Configurations of nematic liquid crystal microdroplet in an electric field
by Rong-Mei Chien

A thesis submitted in partial fulfillment of the requirements for the degree of Doctor of Philosophy in Physics
Montana State University

Abstract:
We have explored the director and order parameter configurations in spherical nematic microdroplets in an applied electric field, using for the internal field calculation a method that takes into account the effect of spatial field variations arising from the liquid crystal's anisotropic polarizability. Our method also takes into consideration the spatial variation of the elastic constants and the anchoring strength, through the dependence of these quantities on the order parameter. The approach is based on the Landau-de Gennes model free energy and determines the stable configurations by numerical solution of the Euler-Lagrange equations for the director with Newton's relaxation method or by direct minimization of total free energy with the conjugate gradient or relaxation techniques We have found that inhomogeneity of the electric field inside the nematic droplet is significant in determining the stable configurations. We also investigated the influence of ratios of Oseen-Frank elastic constants and the spatial dependence of the scalar order parameter on the phase boundary between the radial and axial configurations. For strong anchoring the influence of bend-to-splay ratio on the location of the phase boundary dominates when the twist deformation is not significant. Our nonuniform-field approach predicts a greater range of stability for the radial phase than that obtained by the uniform-field approximation. In addition, the "reentrant" feature of the axial phase is lost. The twist elastic constant has a significant effect on the location of the phase boundary between the radial and axial phases for strong anchoring when the splay elastic constant is large compared to twist and bend elastic constants. We predict a twist configuration when the droplet is viewed along the field. In addition, a mirror symmetry appears on the equatorial plane as the field increases. For weak anchoring the influence of the saddle-splay elastic deformation on the location of phase boundary dominates and inclusion of the saddle-splay deformation stabilizes the radial phase even at very strong external field. The spatial dependence of the order parameter does not affect the location of the phase boundary more than that the various elastic deformations do. However, it does allow the creation of defect regions, where elastic energy is reduced by the suppression of order parameter S. We have discussed the effects of external field strength, anchoring strength, droplet radius, and temperature on the defect region.

CONFIGURATIONS OF NEMATIC LIQUID CRYSTAL MICRODROPLET IN AN ELECTRIC FIELD

by

Rong-Mei Chien

A thesis submitted in partial fulfillment
of the requirements for the degree

of

Doctor of Philosophy

in

Physics

MONTANA STATE UNIVERSITY
Bozeman, Montana

July 1994

APPROVAL

of a thesis submitted by

Rong-Mei Chien

This thesis has been read by each member of the thesis committee and has been found to be satisfactory regarding content, English usage, format, citations, bibliographic style, and consistency, and is ready for submission to the College of Graduate Studies.

7/13/94
Date

Chairperson, Graduate Committee

Approved for the Major Department

7-13-94
Date

Head, Major Department

Approved for the College of Graduate Studies

8/4/94
Date

Graduate Dean

STATEMENT OF PERMISSION TO USE

In presenting this thesis in partial fulfillment of the requirements for a doctoral degree at Montana State University, I agree that the Library shall make it available to borrowers under rules of the Library. I further agree that copying of this thesis is allowable only for scholarly purposes, consistent with "fair use" as prescribed in the U.S. Copyright Law. Requests for extensive copying or reproduction of this thesis should be referred to University Microfilms International, 300 North Zeeb Road, Ann Arbor, Michigan 48106, to whom I have granted "the exclusive right to reproduce and distribute my dissertation for sale in and from microform or electronic format, along with the right to reproduce and distribute my abstract in any format in whole or in part."

Signature 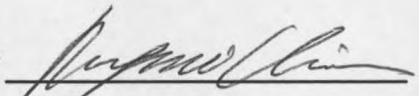

Date 8-8-94

to my husband Chi-Shun (Tim) and my son Stachus Igu

"The fear of the Lord is the beginning of knowledge"

Proverbs 1:7 (NKJV)

VITA

The Author was born Rong-Mei Chien on December 19, 1961 in Whowen, Yunlin, Taiwan, Republic of China to Kuen-Chih Tsai Chien and Chih-Ko Chien (deceased, November 8,1991). She has one older brother (Rong-Kuang Chien) and one older sister (Rong-Hua Chien). She attended public elementary and junior high schools in Whowen. She passed the national entrance examination to attend Taipei Municipal Chung-San Girls' Senior High School. She is married to Chi-Shun (Tim) Tu and has a son: Stachus Igu Tu.

After competition in a national entrance examination she attended National Taiwan Normal University in Taipei, Taiwan from 1980 to 1984 majoring in physics. She graduated as the fouth place of academic achievement in a class of 80 and taught Physics in Taipei Municipal Chung-Cheng Junior High School to fulfill the requirement of her bachelor's degree in physics from 1984 to 1985. She was employed as a teaching assistant in National Taiwan Normal University from 1985 to 1988. She won an excellent edition award of Modern Physics Lab Book in 1988. She also successfully administrated the first National Conference of University General Physics at Taiwan in 1985.

She attended graduate school in physics as a graduate teaching assistant at University of Oregon in Eugene, Oregon from the fall of 1988 to the spring of 1990.

She obtained a M.S. in physics in June 1989 and continued doctoral study until the summer of 1990. She has attended Montana State University in Bozeman, Montana as a graduate teaching and research assistant from the fall of 1990 until the summer of 1994, graduating in July, 1994 with a Ph.D. in physics under Professor George F. Tuthill.

ACKNOWLEDGMENTS

My sincere thanks go first to my advisor, Professor George F. Tuthill, for his support, encouragement, and patient guidance, throughout the course of this work. To my mother-in-law, Mrs. Hsiu-Hsia Tsai Tu, for flying from Taiwan to Bozeman to help me with taking care of my son and dealing with house chores so that I can concentrate in this work and finish the thesis.

Thanks to Professor V. Hugo Schmidt for the discussions that have been of continual benefit to this thesis.

My husband Chi-Shun (Tim) deserves my deepest appreciation for his constant support and encouragement in obtaining this Ph.D. My son Stachus Igu I relied upon to always bring a smile to my heart.

Finally, I would like to acknowledge the financial support supplied me by the Department of Energy under grant number DE-FG06-87ER45292 and the Department of Physics, Montana State University during my four years of graduate study.

TABLE OF CONTENTS

TABLE OF CONTENTS--Continued

LIST OF TABLES

LIST OF FIGURES

ABSTRACT

We have explored the director and order parameter configurations in spherical nematic microdroplets in an applied electric field, using for the internal field calculation a method that takes into account the effect of spatial field variations arising from the liquid crystal's anisotropic polarizability. Our method also takes into consideration the spatial variation of the elastic constants and the anchoring strength, through the dependence of these quantities on the order parameter. The approach is based on the Landau-de Gennes model free energy and determines the stable configurations by numerical solution of the Euler-Lagrange equations for the director with Newton's relaxation method or by direct minimization of total free energy with the conjugate gradient or relaxation techniques

We have found that inhomogeneity of the electric field inside the nematic droplet is significant in determining the stable configurations. We also investigated the influence of ratios of Oseen-Frank elastic constants and the spatial dependence of the scalar order parameter on the phase boundary between the radial and axial configurations. For strong anchoring the influence of bend-to-splay ratio on the location of the phase boundary dominates when the twist deformation is not significant. Our nonuniform-field approach predicts a greater range of stability for the radial phase than that obtained by the uniform-field approximation. In addition, the "reentrant" feature of the axial phase is lost. The twist elastic constant has a significant effect on the location of the phase boundary between the radial and axial phases for strong anchoring when the splay elastic constant is large compared to twist and bend elastic constants. We predict a twist configuration when the droplet is viewed along the field. In addition, a mirror symmetry appears on the equatorial plane as the field increases. For weak anchoring the influence of the saddle-splay elastic deformation on the location of phase boundary dominates and inclusion of the saddle-splay deformation stabilizes the radial phase even at very strong external field. The spatial dependence of the order parameter does not affect the location of the phase boundary more than that the various elastic deformations do. However, it does allow the creation of defect regions, where elastic energy is reduced by the suppression of order parameter S. We have discussed the effects of external field strength, anchoring strength, droplet radius, and temperature on the defect region.

CHAPTER 1

INTRODUCTION

Purpose of the Work

The behavior of liquid crystals in restricted geometries (droplets[1-21], capillaries[22-35], and films) has been of great interest due to the potential applications in electro-optic devices. Under confinement , the large bulk elastic distortion imposed by the curvature of restricted geometries strongly competes with the molecular anchoring at the boundary walls to create unusual director and order parameter configurations, which are position-dependent. The configurations are further altered by applied fields. The case of a nematic liquid crystal confined to small droplets is particularly interesting because nematic droplets are the active components of polymer-dispersed liquid crystals (PDLC)[36-39] which are used in shutters and displays based on field-controlled light scattering.

These PDLC materials are obtained by a polymerization-induced phase separation with spontaneously formed and distributed birefringent nematic droplets, with average radius ranging from less than 0.1 μm to more than 10^2 μm, depending on the polymerization process. Two possible configurations of nematic droplets with weak perpendicular surface anchoring are radial and axial (Figure 3 (a)). The orientation of molecules in the geometrically confined droplets can be controlled by an applied electric field. A nematic or uniaxial liquid crystal has two principal refractive indices: ordinary index n_o and extraordinary index n_e. The index n_o is observed for the ordinary ray, which

is defined to be the light wave with the electric field vibrating perpendicular to the optical axis. The index n_e is observed for a linearly polarized light wave where the electric field is parallel to the optical axis. The direction of the optical axis is given by the director $\hat{n}$ in the case of a nematic, so $n_\perp = n_o$ and $n_{//} = n_e$. When the electric field is applied on a positive-anisotropic ($\Delta\varepsilon = \varepsilon_{//} - \varepsilon_\perp > 0$) nematic droplet with perpendicular surface anchoring, the axis of the axial droplet aligns parallel to the direction of the field and the ordinary index n_o of the droplet is matched with the refractive index n_p of the surrounding polymer material. In this "on" state, the PDLC film will be transparent to normally incident unpolarized or polarized light. In the "off" state, the droplet reverts to a radial structure where the index is mismatched and the droplet scatters light to create an opaque state (Figure 1).

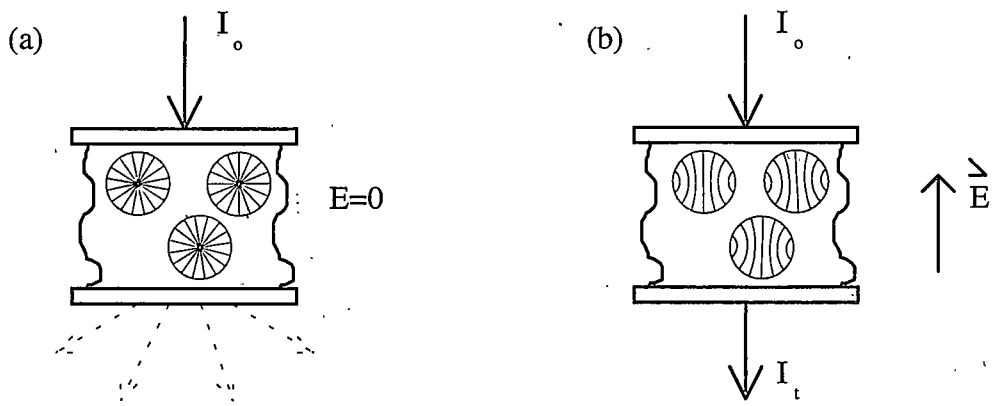

Figure 1. Reorientation of the director within nematic liquid crystal droplets in PDLC due to an applied electric field. The director is unaligned in the absence of electric field (a) such that the droplet ordinary index of refraction $n_o(=n_\perp)$ is not matched to the polymer index of refraction n_p, so that light is scattered and the film looks opaque. The applied electric field aligns the director (b) so that the matching of $n_o(=n_\perp) = n_p$ and $n_e(=n_{//}) \neq n_p$ reduces the scattering of light and produces a transparent state.

In the light shutter device, the director configuration governs the refractive index of the droplets and is important in the response time and voltage of the shutter.

Therefore, it is important to understand as accurately as possible the effect of a given field strength on the director configuration.

Historical Review

Theoretical treatments of nematic droplets in an field have an extensive history. Dubois-Violette and Parodi[1] in 1969 were the first to model in detail the effect of an external (magnetic) field on the director configuration of a spherical droplet, in the limit of strong anchoring. For perpendicular anchoring, they found a first order phase transition from the radial to axial configuration with increasing magnetic field. Candau, Roy and Debeauvais[2] have observed twist configurations of a nematic droplet with normal anchoring in the presence of magnetic field. They also found that the application of a high field gave rise to a disclination line located in a plane perpendicular to the direction of field. Erdman, Zumer, and Doane[4] have studied the axial-radial transition as a function of radius, temperature, and external electric field in the approximation of a spatially uniform order parameter and uniform field inside the droplet. They adopted equal splay and bend constants and neglected twist (K_{22}), saddle-splay (K_{24}), and mixed splay-bend (K_{13}) constants. They have tested their predictions against experimental results obtained on micrometer-sized droplets of the nematic liquid crystal E7 dispersed in a polyurethane matrix. A more thorough theoretical study of this transition by Kralj and Zumer[6] has delineated a region of the phase diagram in which the configuration is axial with an equatorial line defect for anchoring strengths that are large compared to the external field. They have studied the stability diagrams of a supra-μm-sized droplet with weak anchoring in the approximations of uniform scalar order parameter and uniform field inside the droplet. Their approach is based on Landau-de Gennes free energy, including the three basic bulk elastic deformations, and the surface-like saddle-splay elastic deformation, and

finding stable configurations of the droplet by solving Euler-Lagrange equations for the director field with Newton's relaxation method. The phase diagrams basically contain the reentrant feature of the axial phase, and an inversion point where the maximum transition field for the radial-axial transition is reached as well as a zero-field radial-axial coexistence point. Bondar, Lavrentovich, and Pergamenshchik[5] have observed experimentally the transition of the radial to the axial phase in nematic droplets with sizes ranging from few μ m to 30 μm, in an increasing electric field. They found that the molecules far from the drop boundary and equatorial plane are reoriented along the field first as field increases. The configuration thus looks like there is a domain, where the directors are not parallel to the E-field, near the equator. In addition, its thickness decreases as the field strength increases, and disappears when the transition from the radial phase to the axial phase takes place. They also have determined the dependence of the transition E-field strength on the radius of a droplet and the field frequency by observing the transition of the hedgehog (radial phase)-defect ring (axial phase) of various micron-sized droplets. Xu, Kitzerow, and Crooker[8] have investigated the director configurations of nematic droplets with negative dielectric anisotropy and perpendicular anchoring in the presence of an electric field. Using polarization microscopy, they observed for low field that the director field is essentially radial, with some azimuthal twist and a point defect (hedgehog) at the center. At intermediate fields, the point defect moves away from the center along the E-field direction, while at high field a line defect appears along the diameter parallel to the field. Berggren, Zannoni, Chiccoli, Pasini, and Semeria[9] have used Monte Carlo simulations to study the molecular organization, order parameter, and deuterium NMR line shapes of nematic droplets in an applied field.

The splay-bend surface elastic contribution is attracting a great deal of theoretical interest and remains a topic of intense controversy[40-59]. This contribution to the elastic energy density is of the form

$$f_{13} = K_{13}\bar{\nabla}\cdot\left[\hat{n}\left(\bar{\nabla}\cdot\hat{n}\right)\right], \tag{1}$$

and is called a splay-bend surface elastic contribution because it enters the free energy as the coefficient of a divergence term which can be transformed to a surface integral by Green's theorem.

An intensive reexamination of the consequences of a nonvanishing K_{13} has been carried out in recent years by Hinov and Derzhanski[41-44], by Barbero and co-workers[45-56], and by Pergamenshchik and co-workers[57-59]. Barbero and Oldano[45,51] have reported that the term f_{13} leads to strong subsurface distortions. Pergamenshchik[57] interpreted this result as a consequence of the fact that the f_{13} term is unbounded from below, so that the conventional Euler-Lagrange procedure thus involves finding a saddle point, rather than a minimum, of the free energy functional. This is called the Oldano-Barbero paradox. Barbero, Madhusudana, and Oldano[48] have argued that some fourth-order terms should be retained in the elastic free-energy expansion to have the free energy bounded from below. However Pergamenshchik *et al*[57,58] have argued that including the 35 allowed fourth-order terms would give new divergences, and still result in a total free energy which would be unbounded from below. The same would be true of the total contribution at any finite order. Thus it is not possible to solve the problem by introducing new elastic terms up to any finite orders. Pergamenshchik *et al.* instead postulated that the sum R_∞ of all higher-order terms acts as an "appropriate" regularization term which bounds the free energy from below and suppresses unphysically strong subsurface deformations. They claim that the equilibrium director configuration is given, to order $(\delta n)^2$, by the Euler-Lagrange equations associated with the usual Frank-Oseen (Eq. (19)) functional. The Euler-Lagrange equations should be taken formally and do not result from any minimization procedure, since the functional in question has no minimum. Experimental evidence on

the value of K_{13} is rare. Madhusudana *et al*[51] have used the approximation that solutions of Euler-Lagrange equations are valid up to the boundaries and measured the elastic constant K_{13} of a nematic liquid crystal by using PCH-7 (cyanohpetylphenyl cyclohexane) in hybrid nematic layers. The value of K_{13} they have found is about 10^{-6} dynes for temperature slightly below the nematic-isotropic transition temperature, and with anchoring of about 2×10^{-3} ergs / cm^2.

Introduction to this Work

To date, theoretical studies on the director configurations of the nematic liquid crystal in an electric field have assumed that the E field within the droplet is uniform in magnitude and direction[4,6]. However, the liquid crystal's large dielectric anisotropy and the ability of the molecules to reorient themselves in response to elastic and surface, as well as electric forces, will in general make the E field inside the droplet inhomogeneous. Here we investigate the director and order parameter configurations in spherical nematic liquid crystal microdroplets in a uniform and static applied electric field, taking explicit account of the interaction between the electric and the director fields and also taking into consideration the spatial variation of the elastic constants and the anchoring strength, through the dependence of these quantities on the order parameter. The director $\hat{n}$ and electric fields are coupled via the distribution of bound charge at the droplet surface and must be determined self-consistently. We limit our discussion to the case without splay-bend (K_{13}) elastic contribution because its effects have not been completely analyzed. (see the discussion of the splay-bend elastic contribution in Chapter 5) We also assume that the size and the shape of the droplet will not be altered by the applied field, and omit as well any consideration of dynamic phenomena or conductivity.

Liquid Crystals

Mesophases

In addition to the transitions among the three traditional states: solid, liquid, and gas, many organic materials show a cascade of transitions involving new phases; which are intermediate mechanically and symmetrically between the isotropic liquid and the crystalline solid. They have been called liquid crystalline phases or mesophases, since they can be strongly anisotropic in some of their properties and yet exhibit a certain degree of fluidity, in some cases even comparable to that of an ordinary liquid. The constituent molecules, or group of molecules (the building blocks) of liquid crystals are strongly elongated or, less frequently, disk shaped. They range from small organic molecules with lengths ~ 20 Å and widths ~5 Å in PAA (*p*-azoxyanisole) to long helical rods with lengths of order 10^2 ~ 10^3 Å and widths of order 10~10^2 Å in DNA or TMV (tobacco mosaic virus).

Types and Classification of Liquid Crystals

Transitions to and between these mesophases may be induced by changes in temperature, in the case of thermotropic liquid crystals, or by the influence of solvent concentration in lyotropic liquid crystals. Thermotropic liquid crystals, such as E7 (commercial nematic mixture of biphenyls and terphenyls), 5CB (*p*-pentyl-*p'*-cyanobiphenyl), PAA and MBBA [N-(p-methoxybenzylidene)-p'-n-butylaniline], are of interest both from the standpoint of basic research and for applications in electro-optic

displays, temperature and pressure sensors, etc. Lyotropic liquid crystals, such as DNA and TMV, are of great interest biologically and play an important role in living systems.

Following the nomenclature proposed originally by G. Friedel in 1922, mesophases are classified into three general types: nematic, cholesteric (or chiral nematic), and smectic, according to the type and degree of molecular order.

(a) The nematic mesophase has a high degree of long range orientational order of the molecules, but no long range translational order. Thus there is some order in the direction of the molecules; they tend to be parallel to some common axis, labeled by a unit vector $\hat{n}$, called the director (Figure 2 (a)). The preferred direction usually varies from point to point in the medium, but a homogeneously aligned specimen is optically uniaxial (cylindrically symmetric) with the optical axis along $\hat{n}$ and strongly birefringent. The states described by $\hat{n}$ and $-\hat{n}$ appear to be indistinguishable, i.e. the polarity of the constituent molecules does not lead to a macroscopic effect. Consequently the long range orientational order must be described by a symmetric and traceless second rank tensor $Q_{\alpha\beta}$, which will be defined in Chapter 2. In an actual sample the orientation of $\hat{n}$ is imposed by the boundary conditions, thermal distribution, and/or by external fields. This leads to variations in the director pattern, and thus to differences in birefringence.

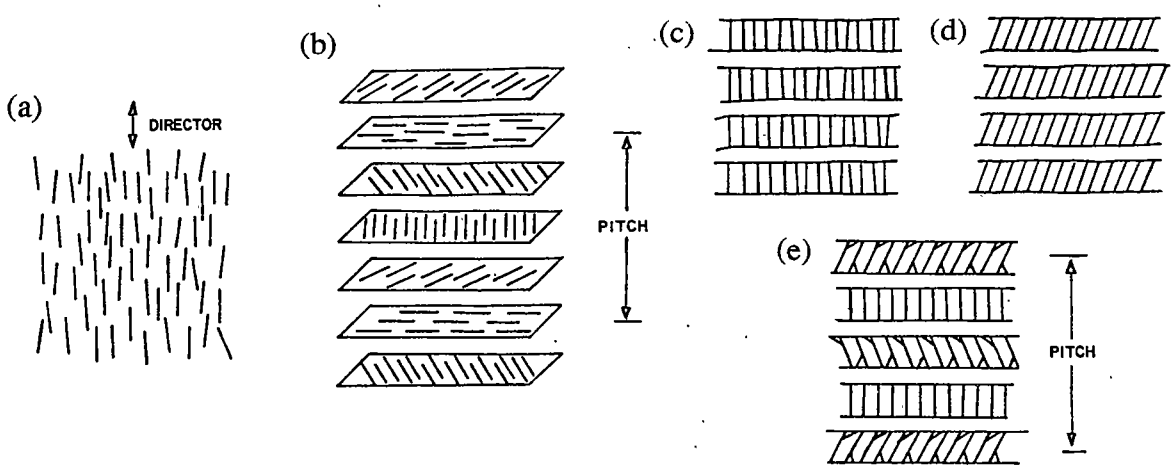

Figure 2. Molecular arrangement in various types of liquid crystals: (a) nematic, (b) cholesteric, (c) smectic A, (d) smectic C, (e) chiral smectic C*.

(b) Locally, a cholesteric mesophase is a nematic type of liquid crystal except that it is composed of optically active molecules. As a consequence, on a large scale, the structure has a screw axis superimposed normal to the director $\hat{n}$ (Figure 2 (b)) and the director $\hat{n}$ helically spirals. Optically inactive molecules or racemic mixtures result in a helix of infinite pitch which corresponds to the true nematic.

(c) Smectic liquid crystals have layered structure but a variety of molecular arrangements are possible within each layer. Many smectic phases such as S_A, S_B, S_C, S_A*, S_C*, S_F, S_I, S_E, S_G, S_H, etc. have been identified, and only smectic A, B, C phases are reasonably well characterized. In smectic A the molecules are upright in each layer with their centers irregularly spaced in a liquid-like fashion (Figure 2 (c)). The thickness of the layer is of the order of the length of the free molecule. The interlayer attractions are weak as compared with the lateral forces between molecules and in consequence the layers are able to slide over one another relatively easily. Thus this phase has fluid properties, though it is still much more viscous than the nematic phase. Smectic B differs from A in that the molecular centers in each layer are hexagonal close packed. Smectic C is a tilted form of smectic A. (Figure 2 (d)) If we add optically-active molecules to a smectic C, the structure distorts; the direction of tilt precesses around the screw axis and a helical configuration C* is obtained. (Figure 2 (e)) Chiral smectic C* compounds are the most popular ferroelectric liquid crystals (FLCs) because their synthesis is uncomplicated and well-documented, and the starting materials are inexpensive and readily available. The advantages of FLCs are that they can be switched at much higher rate than possible with conventional liquid crystal materials and because they are ferroelectric, only a brief electric field application is needed to establish a pattern, which results in lower power requirements.

The Structures of Geometrically Confined Nematic Liquid Crystals

In a practical circumstance of liquid crystals confined to restricted geometries, the internal structures of confined nematics depend on the elastic properties of the liquid crystal, the interfacial interactions between the liquid crystal and the polymer, the temperature, and the external electric or magnetic field. They are characterized by the spatial dependence of the director field $\hat{n}$ and the orientational order parameter S. When the anchoring conditions at the surface are comparably strong, the director configuration of a nematic depends essentially on the type of molecular anchoring at the surface. The variety of director configurations can be classified as follows:

(a) Homeotropic anchoring at the interfacial boundary: The molecules are preferentially anchored perpendicular to the wall; radial and axial configurations are possible in the spherical droplets[2,4-6,8,15,16] (Figure 3 (a)). The radial structure possesses a splay-type deformation from the central point defect. It is stable for strong surface anchoring while an increasing external field will deform the radial structure or even shift the point defect from the center to the surface. If the anchoring is weak or if there is a strong external field the axial configuration is stable. The axial structure essentially contains a splay-bend deformation and the largest deformations appear close to the equator of the droplet. Depending on the strength of the external field and anchoring the structure can be defectless or have a concentric line defect in the equatorial plane. Cylindrical geometries[39] have analogous structures for homeotropic anchoring: planar-radial (PR) (splay deformation) with a line disclination along the cylinder axis and planar-polar (PP) (splay and bend deformations) with two axial line disclinations[27]. The escaped-radial (ER) structure[22,24,25], also possible, is planar and radial near the cavity wall and bends out of the plane to escape along the cylinder axis[23,26,28,29]. Since both directions of bend are

energetically equivalent, often a series of point defects forms along the cylinder axis (escaped-radial-with-point-defects ERPD) (Figure 4 (a)).

(b) Tangential anchoring: bipolar and concentric configurations are possible in spherical droplets[1,2,13,14]. The bipolar configuration with a splay-bend deformation characterized by two point defects (boojums) at the poles of the droplet is the most common structure. The bipolar structure containing twist deformations has also been observed. The concentric configuration with a pure bend deformation and a point defect in the center is rarely seen (Figure 3 (b)). Cylindrical geometries[39] also have analogous structure for tangential anchoring condition such as the parallel-axial PA (no deformation), planar-bipolar PB (splay and bend deformations), planar-concentric PC (pure bend deformation), and escaped-twist structure[33] ET (twist-bend deformation) illustrated in Figure 4 (b).

For materials with small twist elastic constants, a reduction of the splay elastic free energy leads to twisted structures[18-20].

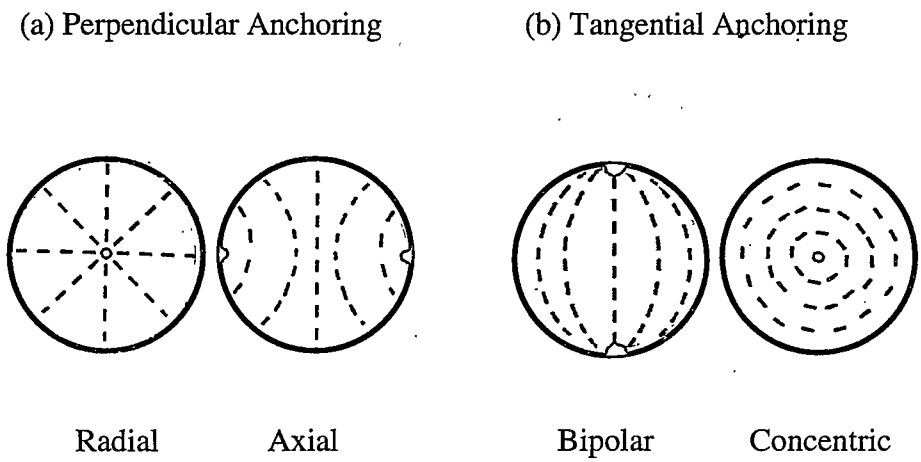

Figure 3. Director configurations of nematic liquid crystal in spherical geometries for (a) perpendicular anchoring: radial and axial, (b) tangential anchoring: bipolar and concentric.

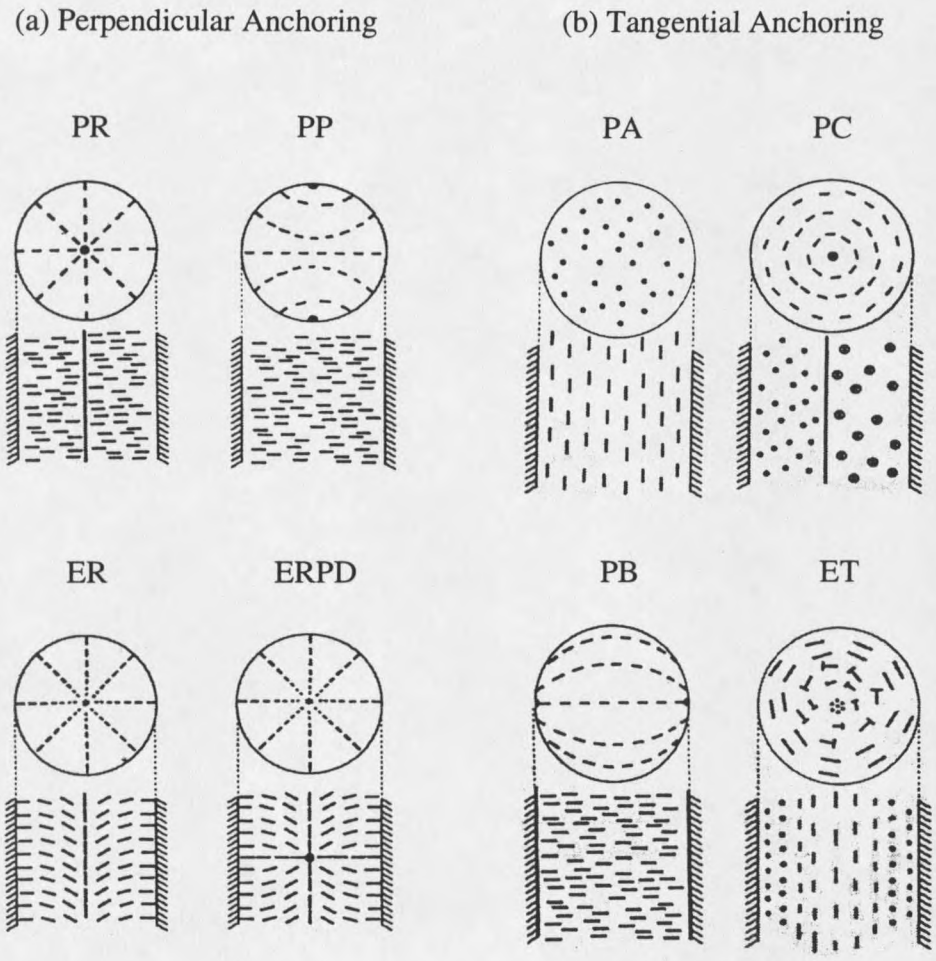

Figure 4. Director configurations of nematic liquid crystal in cylindrical geometries for (a) perpendicular anchoring: parallel radial (PR), planar-polar (PP), escaped-radial (ER), and escaped-radial with point defects, (b) tangential anchoring: parallel-axial (PA), planar-concentric (PC), planar-bipolar (PB), and escaped-twisted (ET).

CHAPTER 2

THEORY

Definition of Order Parameter[60-62]

All liquid crystalline states are characterized by a long range orientational order of the molecules. In fact this is the only aspect in which the nematic and isotropic phases differ. To describe the orientational order of nematics two aspects have to be taken into account: the local average direction of the molecular long axis by a unit vector $\hat{n}$, called the director (Figure 2 (a)), and the ordering in the distribution of the long molecular axes around the director $\hat{n}$. Since $\hat{n}(\bar{r})$ and $-\hat{n}(\bar{r})$ correspond to physically equivalent states, the order parameter $Q(\bar{r})$ must be proportional to an even combination of components of $\hat{n}(\bar{r})$. The two lowest even-order combinations of a unit vector are a scalar and a second rank tensor, and since the liquid crystal order cannot be completely described by a scalar, $Q(\bar{r})$ must be a second rank tensor.

The long-range order in the nematic phase prevents any molecular anisotropy from being averaged to zero. Consequently all macroscopic response functions of the bulk material, such as the dielectric constant or the magnetic susceptibility, are anisotropic as well. In deriving a macroscopic tensor order parameter we shall use the magnetic susceptibility. However, any other macroscopic property as, e.g., the dielectric constant or refractive index, could be used. Application of a magnetic field $\bar{H}$ results in a magnetization $\bar{M}$ given by

$$M_\alpha = \chi_{\alpha\beta} H_\beta, \qquad \alpha,\beta = x,y,z \tag{2}$$

where $\chi_{\alpha\beta}$, M_α, and H_β denote the components of the susceptibility tensor $\vec{\chi}$, the magnetization $\vec{M}$, and the magnetic field $\vec{H}$, respectively. In Eq. (2) summation over repeated indices is implied. In general the tensor $\vec{\chi}$ is symmetric: $\chi_{\alpha\beta} = \chi_{\beta\alpha}$. Thus such a tensor can be reduced to the diagonal form by choosing a suitable coordinate system, i.e.

$$\vec{\chi} = \begin{pmatrix} \chi_1 & 0 & 0 \\ 0 & \chi_2 & 0 \\ 0 & 0 & \chi_3 \end{pmatrix} \tag{3}$$

To extract the anisotropic part of $\vec{\chi}$ we use $\sum_{i=1}^{3} \chi_i = \chi$. Then the elements χ_1, χ_2, and χ_3 can be expressed as

$$\begin{aligned} \chi_1 &= \frac{1}{3}\chi[1-(Q_1 - Q_2)] \\ \chi_2 &= \frac{1}{3}\chi[1-(Q_1 + Q_2)] \\ \chi_3 &= \frac{1}{3}\chi[1+2Q_1]. \end{aligned} \tag{4}$$

That is, the susceptibility tensor is

$$\chi_{\alpha\beta} = \chi\left(\frac{1}{3}\delta_{\alpha\beta} + Q_{\alpha\beta}\right) \tag{5}$$

with the order parameter tensor

$$\ddot{Q} = \begin{pmatrix} -\frac{1}{3}(Q_1 - Q_2) & 0 & 0 \\ 0 & -\frac{1}{3}(Q_1 + Q_2) & 0 \\ 0 & 0 & \frac{2}{3}Q_1 \end{pmatrix} \tag{6}$$

The isotropic liquid is described by $Q_1 = Q_2 = 0$. The anisotropic liquid with the biaxial symmetry requires $Q_1 \neq 0$ and $Q_2 \neq 0$. But the uniaxial nematic is described by only one order parameter, i.e. $Q_1 \neq 0$ and $Q_2 = 0$ for choosing its symmetry axis $\hat{n}$ along the z axis. Then the order parameter tensor becomes

$$\ddot{Q} = Q_1 \begin{pmatrix} -\frac{1}{3} & 0 & 0 \\ 0 & -\frac{1}{3} & 0 \\ 0 & 0 & \frac{2}{3} \end{pmatrix} \tag{7}$$

In addition, the susceptibility tensor $\ddot{\chi}$ is

$$\ddot{\chi} = \begin{pmatrix} \chi_\perp & 0 & 0 \\ 0 & \chi_\perp & 0 \\ 0 & 0 & \chi_{//} \end{pmatrix} \tag{8}$$

Rewriting gives

$$\chi_{\alpha\beta} = (2\chi_\perp + \chi_{//})\left(\frac{1}{3}\delta_{\alpha\beta} + Q_{\alpha\beta}\right) \tag{9}$$

with $Q_1 = \Delta\chi/(2\chi_\perp + \chi_{//})$, where $\Delta\chi = \chi_{//} - \chi_\perp$ denotes the anisotropy in susceptibility. Then the susceptibility tensor $\ddot{\chi}$ can be written as

$$\vec{\vec{\chi}} = \bar{\chi}\vec{\vec{I}} + \Delta\chi \begin{pmatrix} -\frac{1}{3} & 0 & 0 \\ 0 & -\frac{1}{3} & 0 \\ 0 & 0 & \frac{2}{3} \end{pmatrix}, \tag{10}$$

i.e.

$$\vec{\vec{\chi}} = \bar{\chi}\vec{\vec{I}} + \Delta\chi_{max} S \begin{pmatrix} -\frac{1}{3} & 0 & 0 \\ 0 & -\frac{1}{3} & 0 \\ 0 & 0 & \frac{2}{3} \end{pmatrix}, \tag{11}$$

where $\bar{\chi} = (2\chi_{\perp} + \chi_{//})/3$. $\Delta\chi_{max} = \Delta\chi/S$ denotes the anisotropy in the susceptibility in the perfectly aligned phase. Thus the order parameter tensor of a nematic, which is real, symmetric and traceless, can be defined as

$$Q_{\alpha\beta}(\vec{r}) = \frac{3}{2} S(\vec{r}) \left[N_{\alpha\beta} - \frac{1}{3}\delta_{\alpha\beta} \right],$$

$$\text{with } N_{\alpha\beta} = n_{\alpha} n_{\beta} \tag{12}$$

Then the susceptibility tensor is defined as

$$\chi_{\alpha\beta} = \bar{\chi}\delta_{\alpha\beta} + \frac{2}{3}\Delta\chi_{max} Q_{\alpha\beta}, \tag{13}$$

where α, β = x, y, z denote the components along the three orthogonal axes of the Cartesian coordinate system and $S(\vec{r})$ the scalar order parameter, which measures the alignment of the long axes of the molecules. $S(\vec{r})$ may be defined as an quantity that is nonzero in the nematic phase, zero in the isotropic phase, and unity in the perfectly aligned phase:

$$S(\vec{r}) = \frac{1}{2}\left\langle 3\cos^2\theta - 1 \right\rangle, \tag{14}$$

where θ is the angle between the long molecular axis and the local director $\hat{n}(\vec{r})$, the bracket $< >$ standing for the statistical average over molecules in the local region. When all the molecules are fully aligned with $\hat{n}$, all θ=0 then $\left\langle \cos^2\theta \right\rangle = 1$ and S=1. On the other hand, if the molecules are randomly distributed in direction, all values of θ are equally likely, so $\left\langle \cos^2\theta \right\rangle = 1/3$ and S=0.

Macroscopic Continuum Theory of Nematic Liquid Crystals[63]

Now it is clear that the orientation of a nematic (uniaxial) liquid crystal must be described in terms of the tensor $N_{\alpha\beta}(\vec{r})$, whereas the degree of ordering is expressed by the order parameter S. However, the bulk response of confined nematic liquid crystals to external disturbances usually involves a large-scale (~1 μm) phenomena compared to molecular dimensions (~ of the order 10 ~10^2 Å). Thus it is more convenient to regard the liquid crystal as a continuous medium with a set of elastic constants than to treat it on a molecular basis. On the other hand, the degree of order S(T) will be hardly affected by the slow variations of orientation. Hence it is useful to consider a liquid crystalline material with a slowly varying orientation, such that the medium remains locally uniaxial while S(T) does not depend on the position $\vec{r}$. Consequently the liquid crystal deformation may be described by a second rank tensor field $N_{\alpha\beta}(\vec{r})$ disregarding the details of the structure on the molecular scale. This consideration is the basis of the continuum theory of liquid crystals developed by Oseen[64] (1933), Zocher[65] (1933), and Frank[66] (1958).

In a nematic liquid crystal in the absence of surface effects, flow, or external perturbations, the parallel alignment of all local directors represents the equilibrium state with minimum free energy. Generally speaking, however, a confined nematic liquid crystal is in a distorted state with higher free energy, the enforced interfacial anchoring, an applied external field, or thermal fluctuation causing the local directors $\hat{n}(\vec{r})$ to vary spatially. Thus we can think of the spatial derivatives of the tensor field $N_{\alpha\beta}(\vec{r})$ as the distortion parameters. The deformation in a nematic liquid crystal in turn brings about 'restoring forces' that oppose curvature. Frank referred to these generalized forces as torque stresses and assumed a linear relation between these stresses and the curvature strains (essentially Hooke's law). Then the free energy density of a deformed liquid crystal can be expanded around the equilibrium state , where $\partial_\alpha N_{\beta\gamma}(\vec{r}) = 0 = \partial_\alpha \partial_\beta N_{\gamma\delta}(\vec{r})$, retaining only the first and second order terms, $\partial_\alpha N_{\beta\gamma}(\vec{r})$ and $\partial_\alpha \partial_\beta N_{\gamma\delta}(\vec{r})$, where $\partial_\alpha = \partial / \partial_\alpha$ and the Greek indices denote x, y, z. This approximation is equivalent to the assumption of a linear relation between stress and strain:

$$F(\vec{r}) = F_o + F_d(\vec{r})$$

$$F_d(\vec{r}) = L_{\alpha\beta}(\vec{r})\partial_\alpha n_\beta + L_{\alpha\beta\gamma\delta}(\vec{r})\left[\partial_\alpha n_\beta(\vec{r})\right]\left[\partial_\gamma n_\delta(\vec{r})\right] + L_{\alpha\beta\gamma}(\vec{r})\partial_\alpha \partial_\beta n_\gamma(\vec{r}), \qquad (15)$$

where F_o is the free energy density of the equilibrium states. $F_d(\vec{r})$ is the Frank free energy density for the distorted state and is obtained by using $N_{\alpha\beta}(\vec{r}) = n_\alpha(\vec{r}) n_\beta(\vec{r})$. The tensors $L_{\alpha\beta}(\vec{r})$, $L_{\alpha\beta\gamma}(\vec{r})$, and $L_{\alpha\beta\gamma\delta}(\vec{r})$, which are dependent on the order parameter S, must be composed of all possible combinations of $n_\alpha(\vec{r}), \delta_{\alpha\beta}$, and $\varepsilon_{\alpha\beta\gamma}$, and can be determined by the following constraints:

(a) The free energy density $F_d(\vec{r})$ must be a scalar quantity.

(b) $F_d(\vec{r})$ must be even in the n_α, because of head-tail symmetry.

Keeping the essential different and non-zero contributions, the general Frank free energy density is obtained as

$$F_d(\bar{r}) = k\varepsilon_{\alpha\beta\gamma} n_\gamma \partial_\alpha n_\beta + k_1(\partial_\alpha n_\alpha)(\partial_\beta n_\beta) + k_2(\partial_\alpha n_\beta)(\partial_\alpha n_\beta) + k_3 n_\alpha n_\beta (\partial_\alpha n_\gamma)(\partial_\beta n_\gamma), \quad (16)$$

where k, k_1, k_2, and k_3 are functions of order parameter S. Discarding surface contributions from terms of the form $\nabla \cdot \bar{u}(\bar{r})$, where $\bar{u}(\bar{r})$ is any vector field, the Frank free energy density can be written in the more compact form with vector notation

$$F_d(\bar{r}) = k(\hat{n}(\bar{r}) \cdot \nabla \times \hat{n}(\bar{r})) + \frac{1}{2}K_{11}(\nabla \cdot \hat{n}(\bar{r}))^2 + \frac{1}{2}K_{22}(\hat{n}(\bar{r}) \cdot \nabla \times \hat{n}(\bar{r}))^2 + \frac{1}{2}K_{33}(\hat{n}(\bar{r}) \times \nabla \times \hat{n}(\bar{r}))^2 \quad (17)$$

where k=0 in the nematic case but nonzero in the chiral nematics. K_{11}, K_{22}, and K_{33} are, respectively, the Oseen-Frank splay, twist, and bend elastic constants. The three basic deformations associated with K_{11}, K_{22}, and K_{33} are shown in Figure 5.

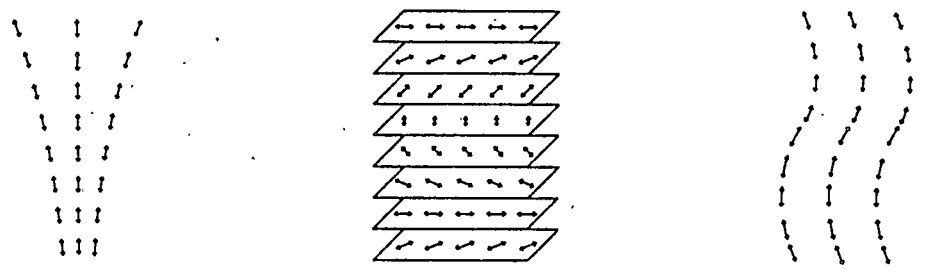

(a) Splay (b) Twist (c) Bend

Figure 5. The three basic elastic deformations of a nematic: (a) splay, (b) twist, (c) bend.

Usually $K_{22} \leq K_{11} \leq K_{33}$ and for the rod-like nematics one has found approximately: $0.5 < K_{33} / K_{11} < 3.0$ and $0.5 < K_{22} / K_{11} < 0.8$.[20,32,34,67-70] The Oseen-Frank constants are of the order of 10^{-7} ~ 10^{-6} dyne and are also temperature dependent:

$K \propto S^2(T) + cS^3(T) + \ldots$ with $c \ll 1$, which follows from the Landau-de Gennes description[69,74]. When a single elastic constant approximation ($K_{11} = K_{22} = K_{33} = K$) is used for the nematic case, the Frank free energy density can be written as

$$F_d = \frac{K}{2}\left\{\left[\nabla \cdot \hat{n}(\vec{r})\right]^2 + \left[\nabla \times \hat{n}(\vec{r})\right]^2\right\} \tag{18}$$

Nehring and Saupe[71,72] have reported that second order terms in the free energy expansion should not be neglected and have proposed the following more general expression for nematic liquid crystals:

$$F_{N\text{-}S}(\vec{r}) = \frac{1}{2}K_{11}\left[\nabla \cdot \hat{n}(\vec{r})\right]^2 + \frac{1}{2}K_{22}\left[\hat{n}(\vec{r}) \cdot \nabla \times \hat{n}(\vec{r})\right]^2 + \frac{1}{2}K_{33}\left[\hat{n}(\vec{r}) \times \nabla \times \hat{n}(\vec{r})\right]^2$$
$$-\frac{1}{2}K_{24}\vec{\nabla} \cdot \left\{\hat{n}(\vec{r})\left[\vec{\nabla} \cdot \hat{n}(\vec{r})\right] + \left[\hat{n}(\vec{r}) \times \nabla \times \hat{n}(\vec{r})\right]\right\} + K_{13}\vec{\nabla} \cdot \left\{\hat{n}(\vec{r})\left[\vec{\nabla} \cdot \hat{n}(\vec{r})\right]\right\}, \tag{19}$$

where K_{24} is the saddle-splay and K_{13} the splay-bend elastic constant. The equivalency of different forms in saddle-splay term is $\left[\hat{n}(\vec{r}) \times \nabla \times \hat{n}(\vec{r})\right] = -\left[\hat{n}(r) \cdot \vec{\nabla}\right]\hat{n}(\vec{r})$. Here it should be mentioned that we follow the notation of Saupe from his 1981 paper[73] where the sum (K_{24}+K_{22}) originally used (by Frank[66], and Nehring and Saupe[71,72]) is replaced by $K_{24}/2$.

Landau-de Gennes Model[60,61,74,75]

The Landau Expansion

Landau theory is a generalization of mean field theory that gives a phenomenological description of phase transitions. This approach begins with the

assumption that the thermodynamic free energy near the critical point (second order order-disorder transition point) can be expanded as a power series in the order parameter, which is arbitrarily small there. In the neighborhood of the transition point, the free energy density is postulated to be given by

$$F(T,Q) = F_o(T) + \lambda(T)Q + \frac{1}{2}A(T)Q^2 + \frac{1}{3}B(T)Q^3 + \frac{1}{4}C(T)Q^4 + ... \qquad (20)$$

The stability condition for determining the equivalent value of Q is $(dF/dQ) = 0$. In the absence of an ordering field (i.e. $\lambda = 0$), this reduces Eq. (20) to

$$F(T,Q) = F_o(T) + \frac{1}{2}A(T)Q^2 - \frac{1}{3}B(T)Q^3 + \frac{1}{4}C(T)Q^4 + ..., \qquad (21)$$

where the negative sign in front of B has been chosen for reasons of convenience, and at high T we thus require Q=0.

Since the order parameter is zero at equilibrium in the high temperature phase, F(T,Q) has its minimum at Q=0 for $T > T_c$, i.e. $d^2F/dQ^2 = A > 0$. Likewise F(T,Q) has a relative maximum at Q=0 for $T < T_c$, i.e. $A < 0$. Thus, $d^2F/dQ^2 = A = 0$ at the transition temperature T_c, implying that $A = a(T - T_c)$ with a>0.

The equilibrium value of the order parameter Q_o can be obtained from the stability condition

$$\left(\frac{dF}{dQ}\right)_{Q=Q_o} = 0 = a(T - T_c)Q_o - BQ_o^2 + CQ_o^3 + ... \qquad (22)$$

Near the transition point $T=T_c$

$$\text{(a) } Q_o = 0 \text{ for the high temperature phase} \qquad (23)$$

$$\text{(b) } Q_o = \frac{B \pm \sqrt{B^2 - 4aC(T - T_c)}}{2C} \tag{24}$$

For a second-order phase transition Q is continuous at the transition, requiring B=0, i.e. in the low temperature phase $Q = \pm\sqrt{-A/C}$. This means that C must be positive since $A = a(T - T_c) < 0$ for $T < T_c$. Therefore, the Landau free energy density takes the form

$$F_L(T,Q) \cong F_o(T) + \frac{1}{2}a(T - T_c)Q^2 + \frac{1}{4}C(T)Q^4 + \ldots; a, C > 0 \tag{25}$$

Generalization of the Landau Expression to Liquid Crystals

In the Landau approach, the free energy density is approximated by a low-order polynomial in the order parameter near the second-order transition where the order parameter will be small. All isotropic-nematic phase transitions are first order and $Q(\vec{r})$ exhibits a discontinuous jump at $T=T_C$ from $Q(\vec{r})=0$ in the isotropic phase to $Q(\vec{r}) \neq 0$ in the low-temperature phase. P.G. de Gennes was the first to successfully apply this theory to the first-order isotropic nematic phase transitions of liquid crystals. The resulting Landau-de Gennes theory provides a satisfactory description of the phase transition from a phenomenological point of view. This generalization can be achieved by including the coefficient B, which can result in a first-order transition. If the symmetry of the low temperature phase does not allow for the appearance of odd powers in Q, i.e. B=0, a first-order transition can be also obtained by taking C to be negative. In addition, a positive sixth power term in Q is required to ensure stability of the ordered phase.

The free energy being a scalar, the expansion of F in powers of $\vec{\vec{Q}}$ can only contain terms that are invariant combinations of the elements $Q_{\alpha\beta}$ of the order parameter tensor. Since the expansion only can contain scalar combinations of $\vec{\vec{Q}}(\vec{r})$ and its spatial derivatives, the term linear in $\vec{\vec{Q}}(\vec{r})$ vanishes because $\vec{\vec{Q}}(\vec{r})$ is symmetric and traceless, that is, there is no linear invariant of such quantity. The term linear in the spatial derivative of $\vec{\vec{Q}}(\vec{r})$ also must vanish since there is no way of forming a scalar quantity from the derivative. However, the term cubic in $\vec{\vec{Q}}(\vec{r})$ does not have to vanish because it is possible to construct a scalar from three 'tensors', and also $\vec{\vec{Q}}(\vec{r})$ and $-\vec{\vec{Q}}(\vec{r})$ physically correspond to different states. Thus the free energy density is no longer symmetric about $\vec{\vec{Q}}(\vec{r})=0$. Recalling that the trace of a matrix or of a product of matrices is a scalar, the free energy density of the uniaxial nematic liquid crystal can be written as

$$F_{L-dG} = F_o(T) + \frac{1}{2}a(T-T_c^*)^{\tau} Q_{\alpha\beta}(\vec{r})Q_{\beta\alpha}(\vec{r}) - \frac{1}{3}BQ_{\alpha\beta}(\vec{r})Q_{\beta\gamma}(\vec{r})Q_{\gamma\alpha}(\vec{r}) + \frac{1}{4}C_1\left[Q_{\alpha\beta}(\vec{r})Q_{\beta\alpha}(\vec{r})\right]^2 + \frac{1}{4}C_2 Q_{\alpha\beta}(\vec{r})Q_{\beta\gamma}(\vec{r})Q_{\gamma\delta}(\vec{r})Q_{\delta\alpha}(\vec{r}) + \frac{1}{2}L_1\partial_\alpha Q_{\beta\gamma}(\vec{r})\partial_\alpha Q_{\beta\gamma}(\vec{r}) + \frac{1}{2}L_2\partial_\alpha Q_{\alpha\gamma}(\vec{r})\partial_\beta Q_{\beta\gamma}(\vec{r}) \tag{26}$$

where T_c^* is the temperature (slightly below T_c) below which supercooling is impossible, a>0, B, C_1, C_2 ,and τ is an unknown exponent. (τ=1 in a mean field theory such as the Maier-Saupe theory; here τ=1). L_1 and L_2 may be called the elastic constants in the isotropic phase. The last two terms contribute to $F_{L\text{-}dG}$ in situations where the order parameter $\vec{\vec{Q}}(\vec{r})$ varies slowly from point to point.

Substituting Eq. (12) for $Q_{\alpha\beta}(\vec{r})$ into Eq. (26) and omitting surface contributions to the free energy density, the Landau-de Gennes free energy density is

$$F_{L-dG} = F_o(T) + F_{or}(\vec{r},T) + F_{F-e}(\vec{r},T) + F_{cp}(\vec{r},T), \tag{27}$$

where[75]

$$F_{or}(\vec{r},T)=\frac{3}{4}a(T-T_c^*)S^2(\vec{r})-\frac{1}{4}BS^3(\vec{r})+\frac{9}{16}CS^4(\vec{r})+\frac{3}{4}\left(L_1+\frac{1}{6}L_2\right)\left[\vec{\nabla}S(\vec{r})\right]^2 \tag{28}$$

$$F_{F-e}(\vec{r},T)=\frac{9}{4}S^2(\vec{r})\left\{\left(L_1+\frac{1}{2}L_2\right)\left[\vec{\nabla}\cdot\hat{n}(\vec{r})\right]^2+L_1\left[\hat{n}(\vec{r})\cdot\vec{\nabla}\times\hat{n}(\vec{r})\right]^2+\left(L_1+\frac{1}{2}L_2\right)\left[\hat{n}(\vec{r})\times\vec{\nabla}\times\hat{n}(\vec{r})\right]^2\right\} \tag{29}$$

$$F_{cp}(\vec{r},T)=\frac{3}{8}L_2\left[\hat{n}(\vec{r})\cdot\vec{\nabla}S(\vec{r})\right]^2+\frac{3}{4}L_2S(\vec{r})\left\{2\left[\vec{\nabla}\cdot\hat{n}(\vec{r})\right]\left[\hat{n}(\vec{r})\cdot\vec{\nabla}S(\vec{r})\right]+\left[\hat{n}(\vec{r})\times\vec{\nabla}\times\hat{n}(\vec{r})\right]\cdot\vec{\nabla}S(\vec{r})\right\} \tag{30}$$

$F_o(T)$ is the free energy of the isotropic phase, $F_{or}(\vec{r},T)$ concerns the orientational order $S(\vec{r})$ and its spatial variation, $F_{F-e}(\vec{r},T)$ contains the familiar contributions of splay, twist, and bend distortions of the director field $\hat{n}(\vec{r})$ (but only two different elastic constants instead of three well-known independent Frank elastic constants), and $F_{cp}(\vec{r},T)$ represents the interactions between the spatial derivatives of the order parameter $S(\vec{r})$, and $\hat{n}(\vec{r})$ and its derivatives.

The equilibrium value S_o can be obtained by minimizing the homogeneous part F_h of the free energy density:

$$F_h=F_o(T)+\frac{3}{4}a(T-T_c^*)S^2-\frac{1}{4}BS^3+\frac{9}{16}CS^4 \tag{31}$$

with respect to S. This means that S_o is determined by the equation

$$\frac{3}{2}a(T-T_o^*)S_o-\frac{3}{4}BS_o^{\,2}+\frac{9}{4}CS_o^{\,3}=0 \tag{32}$$

The solutions are

$$S_o = 0 \quad \text{, the isotropic phase} \tag{33}$$

$$S_o^{\pm} = \frac{B \pm \sqrt{B^2 - 24a(T - T_o^*)C}}{6C}. \tag{34}$$

The correct solution describing the temperature dependence of the order parameter in the nematic phase is the S_o^+ solution. This follows from the calculation of the transition temperature T_c by using the condition $F_h = F_o$, i.e.

$$\frac{3}{4}a(T - T_c^*)S_c^2 - \frac{1}{4}BS_c^3 + \frac{9}{16}CS_c^4 = 0 \tag{35}$$

and the second relation between S_c and T_c given by Eq. (32):

$$\frac{3}{2}a(T_c - T_o^*)S_c - \frac{3}{4}BS_c{}^2 + \frac{9}{4}CS_c{}^3 = 0 \tag{36}$$

The two possible solutions are:

$$S_c = 0 \qquad ,T_c = T_c^* \tag{37}$$

$$S_c = \frac{2B}{9C} \qquad ,T_c = T_c^* + \frac{B^2}{27aC} \tag{38}$$

Clearly the S_o^- solution gives the result $S_c = 0$ at $T = T_c^*$, whereas the S_o^+ solution gives $S_c = 2B/9C$ at the higher transition temperature $T_c = T_c^* + B^2/27aC$. The solutions Eq. (34) determine a third temperature T_c^+, called maximum superheating temperature, given by

$$T_c^+ = T_c^* + \frac{B^2}{24aC} \tag{39}$$

Concluding then, the Landau-de Gennes theory distinguishes four different temperature regions[74]:

(a) $T > T_c^+$: the isotropic phase (S=0) is stable whereas the nematic phase is unstable.

(b) $T_c < T < T_c^+$: the isotropic phase is stable and the nematic phase metastable obtained by overheating.

(c) $T_c^* < T < T_c$ the nematic phase is stable and the isotropic phase metastable obtained by undercooling.

(d) $T < T_c^*$: no way to obtain the isotropic phase, only the nematic phase is reached. (i.e. T_c^* is the minimum supercooling temperature)

The above statements are illustrated in Figure 6, a qualitative plot of the difference in free energy (see Eq. (31)) $\Delta F = \frac{(F_h - F_o)}{aT_c^*} = \frac{3}{4}\left(\frac{T}{T_c^*} - 1\right)S^2 - \frac{1}{4}S^3 + \frac{9}{16}S^4$, with $B = C = aT_c^*$, versus S for five different temperatures. The curves 1 to 5 refer respectively to the temperatures, $T > T_c^+, T = T_c^+, T = T_c, T = T_c^*$, and $T < T_c^*$. The isotropic phase (1), the metastable nematic phase (2), the metastable isotropic phase (3), and the nematic phase (4) lie in the regions bounded respectively by curve 2, curves 2 and 3, curves 3 and 4, and curve 4.

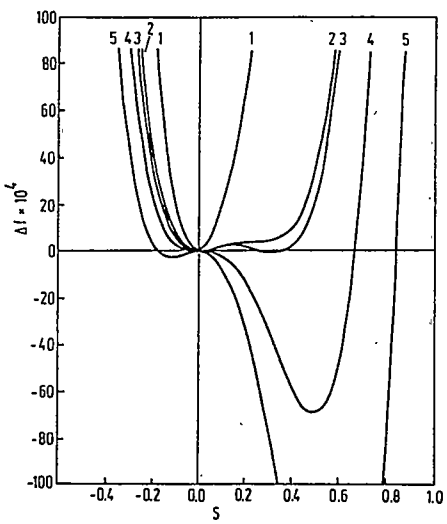

Figure 6. Qualitative illustration of the difference in Landau free energy density (Eq. (31)) $\Delta F = (F_h - F_o)$ versus S for five different temperatures: $T > T_c^+$, $T = T_c^+$, $T = T_c$, $T = T_c^*$, and $T < T_c^*$.

Effects of Static External Fields

Uniform Field Approach

Nematic liquid crystal molecules exhibit strong anisotropy in their electrical and magnetic response. Typically, the dielectric constant ε or the electric anisotropy $\Delta\varepsilon$ is of order $10^{-1} \sim 10^{0}$ and magnetic susceptibility χ or the magnetic anisotropy $\Delta\chi$ is of order $10^{-7} \sim 10^{-6}$ in cgs units. A uniform field approximation is therefore valid for the case of an applied magnetic field, but for the electric field case we must expect a strong inhomogeneity of the field induced by the large dielectric anisotropy. Nonetheless, this uniform electric field approximation can be used for comparison with the magnetic-field case, as has been done by Kralj and Zumer[6].

In the uniform field approximation, we assume that the field inside the nematic liquid crystal droplet is constant in magnitude and direction, and that the order parameter S is spatially uniform as well.

The dielectric tensor $\vec{\varepsilon}(\vec{r})$ for the nematic can be derived from the definitions of order parameter in Eq. (12) and Eq. (13)

$$\begin{aligned}\vec{\varepsilon} &= \bar{\varepsilon}\vec{I} + \frac{2}{3}\Delta\varepsilon_{max}\vec{Q} \\ &= \bar{\varepsilon}\vec{I} + \Delta\varepsilon_{max} S\left[\hat{n}(\vec{r})\hat{n}(\vec{r}) - \frac{1}{3}\vec{I}\right],\end{aligned} \tag{40}$$

i.e.

$$\begin{aligned}\vec{\varepsilon}(\vec{r}) &= \bar{\varepsilon}\vec{I} + \Delta\varepsilon\left[\hat{n}(\vec{r})\hat{n}(\vec{r}) - \frac{1}{3}\vec{I}\right] \\ &= \varepsilon_{\perp}\vec{I} + \Delta\varepsilon\hat{n}(\vec{r})\hat{n}(\vec{r})\end{aligned} \tag{41}$$

where $\bar{\varepsilon} = 1/3(\varepsilon_{//} + 2\varepsilon_{\perp})$, $\varepsilon_{//}$, and $\varepsilon_{\perp}$ are the static dielectric constants in the directions parallel and perpendicular to the director $\hat{n}(\vec{r})$, respectively, and $\Delta\varepsilon = \Delta\varepsilon_{max} S$. $(\Delta\varepsilon)_{max}$ is the maximum possible value of the dielectric anisotropy, i.e., the anisotropy of dielectric constants in the perfectly aligned phase. Thus $\Delta\varepsilon = (\Delta\varepsilon)_{max} S = (\varepsilon_{//} - \varepsilon_{\perp})$ measures the local dielectric anisotropy. The electric displacement $\vec{D}$ induced by $\vec{E}$ is given by

$$\vec{D} = \vec{\varepsilon} \cdot \vec{E} = \varepsilon_{\perp} \vec{E} + \Delta\varepsilon \left[\vec{E} \cdot \hat{n}(\vec{r}) \right] \hat{n}(\vec{r}) \tag{42}$$

so $\vec{D} = \varepsilon_{//} \vec{E}$ if $\vec{E}$ is parallel to $\hat{n}(\vec{r})$, and $\vec{D} = \varepsilon_{\perp} \vec{E}$ if $\vec{E}$ is perpendicular to $\hat{n}(\vec{r})$.

Because the liquid crystal molecules are generally electrically polarizable, diamagnetic, and anisotropic in their electric and magnetic properties, an applied field helps align the molecules and usually contributes to the free energy density an amount which is opposite in sign to that of the elastic distortion free energy density. Then the free energy density due to an electric field (in this homogeneous approach) can be written as

$$\begin{aligned} F_E &= -\frac{1}{4\pi} \int_0^E \vec{D}' \cdot \vec{E}' = -\frac{1}{8\pi} \vec{E} \cdot \vec{\varepsilon} \cdot \vec{E} \\ &= -\frac{1}{8\pi} \varepsilon_{\perp} E^2 - \frac{1}{8\pi} \Delta\varepsilon \left[\vec{E} \cdot \hat{n}(\vec{r}) \right]^2 \end{aligned} \tag{43}$$

Similarly, the effect of a static applied magnetic field $\vec{H}$ depends on the magnetic susceptibility tensor $\vec{\chi}$, written as

$$\begin{aligned} \vec{\chi}(\vec{r}) &= \bar{\chi} \vec{I} + \Delta\chi \left[\hat{n}(\vec{r}) \hat{n}(\vec{r}) - \frac{1}{3} \vec{I} \right] \\ &= \chi_{\perp} \vec{I} + \Delta\chi \hat{n}(\vec{r}) \hat{n}(\vec{r}) \end{aligned} \tag{44}$$

where $\overline{\chi} = 1/3(\chi_{//} + 2\chi_{\perp})$ and $\Delta\chi = (\Delta\chi)_{max} S = (\chi_{//} - \chi_{\perp})$ measures the local diamagnetic anisotropy, with $\chi_{//}$ and $\chi_{\perp}$ denoting the static diamagnetic susceptibilities parallel and perpendicular to $\hat{n}(\vec{r})$, respectively. Thus we obtain the free energy density induced by the magnetic field $\vec{H}$ as

$$\begin{aligned} F_M &= -\frac{1}{2}\vec{H}\cdot\tilde{\chi}\cdot\vec{H} \\ &= -\frac{1}{2}\chi_{\perp}H^2 - \frac{1}{2}\Delta\chi\left[\vec{H}\cdot\hat{n}(\vec{r})\right]^2 \end{aligned} \tag{45}$$

The terms $-\frac{1}{2}\chi_{\perp}H^2$ in F_M and $-\frac{1}{8\pi}\varepsilon_{\perp}E^2$ in F_E are temperature- and field-dependent constants (i.e. independent of $\hat{n}(\vec{r})$) and can be omitted in the discussion. Parallel alignment with the field is favored if $\Delta\varepsilon(=\varepsilon_{//} - \varepsilon_{\perp}) > 0$ or $\Delta\chi(=\chi_{//} - \chi_{\perp}) > 0$, and perpendicular alignment if $\Delta\varepsilon < 0$ or $\Delta\chi < 0$.

Dimensional analysis shows that an elastic constant and the applied field may be combined to define a natural length, which characterizes the competition between elastic and electric or magnetic energy densities. The coherence length ξ measures how far the alignment of the director (for instance induced by a surface where the molecules are strongly anchored) persists in the presence of an applied field, and may be defined as follows:

(i) magnetic case[76]: $$\xi = \frac{1}{H}\sqrt{\frac{K}{S(\Delta\chi)_{max}}} \tag{46}$$

(ii) electric case[77]: $$\xi = \frac{1}{E}\sqrt{\frac{4\pi K}{S(\Delta\varepsilon)_{max}}}, \tag{47}$$

where K is a typical Frank elastic constant.

Nonuniform Field Approach: Electric Field Inside the Droplet

The large dielectric anisotropy $\Delta\varepsilon$ and dielectric constant ε of the liquid crystal, and hence the ability of the molecules to align themselves more closely with the electric field, will generally make the electric field inside the liquid crystal droplet inhomogeneous. A calculation of this inhomogeneous electric field is necessary to give a more precise description of the director configurations in the confined nematic liquid crystal droplet.

Dielectrics differ from conductors in that they have no free charges that can move through the material under the influence of an electric field. In dielectrics, all the electrons are bound; electric charge displacement is the only motion possible in the presence of an electric field. Then the dielectric material is said to be polarized and the molecules possess induced dipole moments. These dipoles produce their own field that can be comparable with the external applied electric field in magnitude, and should be added to the external electric field to result in a true internal field. Since the internal field affects the director orientation, and the director orientation enters into the dielectric tensor and hence affects the internal field, our calculation must determine both the electric field and the director field self-consistently.

For a given director configuration at the surface of the confined nematic droplet we calculate the E field within the droplet by solving Laplace's equation with appropriate boundary conditions.

The spherical droplet of radius R is assumed to be placed in an infinite slab of material with uniform polarization p_o perpendicular to the slab's parallel faces, which are electrically insulated, as indicated in Figure 7. Thus the E field far from the droplet is $E_o = -4\pi p_o$.

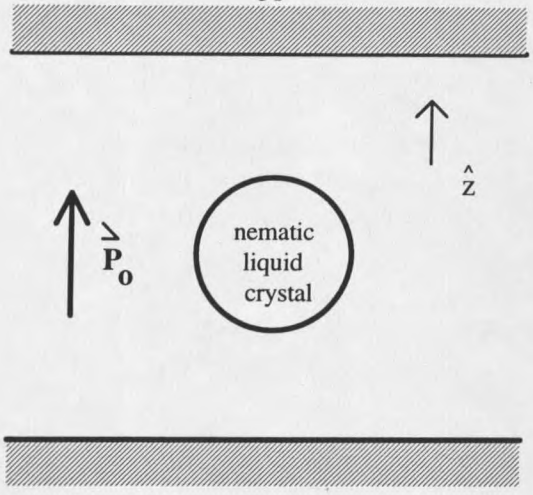

Figure 7. The nematic liquid crystal microdroplet in the infinite polarized slab.

Since there are no free charges either inside or outside the droplet, the problem is one of Laplace's equation with the proper boundary conditions at surface r=R. From the axial symmetry of the geometry, we can take the solution of the potential inside and outside droplet to be in the form of a multipole expansion:

$$\text{INSIDE:} \qquad \Phi_{in} = \sum_{n=0}^{\infty} C_n r^n P_n(\cos\theta) \tag{48}$$

$$\text{OUTSIDE:} \qquad \Phi_{out} = -E_o r\cos\theta + \sum_{n=0}^{\infty} G_n r^{-n-1} P_n(\cos\theta) \tag{49}$$

where the boundary condition at infinity ($\Phi_{out} \rightarrow -E_o r\cos\theta$) has been used and P_n's are Legendre polynomials. The other coefficients are determined from the boundary conditions at the droplet surface (r=R):

$$\text{TANGENTIAL E:} \qquad \vec{E}_{//,in} = \vec{E}_{//,out} \tag{50}$$

$$\text{NORMAL D:} \qquad \vec{D}_{\perp,in} = \vec{D}_{\perp,out} \tag{51}$$

The dielectric tensor $\vec{\varepsilon}$, which enters into the definition of $\vec{D}$, is

$$\vec{\varepsilon}(\vec{r}) = \varepsilon_{\perp}\vec{I} + \Delta\varepsilon\left[\hat{n}(\vec{r})\hat{n}(\vec{r})\right], \tag{52}$$

where $\Delta\varepsilon = (\Delta\varepsilon)_{max} S(\vec{r})$ and $\varepsilon_{\perp} = \Delta\varepsilon + \varepsilon_{//}$ are dependent on the order parameter $S(\vec{r})$ but independent of the director $\hat{n}(\vec{r})$.

Thus

$$\begin{aligned}\vec{D}_{\perp,in} = \hat{r}\cdot\vec{\varepsilon}\cdot\vec{E}_{in} &= \hat{r}\cdot\left\{\varepsilon_{\perp}\vec{I} + \Delta\varepsilon\left[\hat{n}(\vec{r})\hat{n}(\vec{r})\right]\right\}\cdot\vec{E}_{in} \\ &= \hat{r}\cdot\left\{\varepsilon_{\perp}\vec{E}_{in} + \Delta\varepsilon\left[\hat{n}(\vec{r})\cdot\vec{E}_{in}\right]\hat{n}(\vec{r})\right\}.\end{aligned} \tag{53}$$

The first boundary condition gives:

$$G_n = C_n R^{2n+1} + E_o R^{n+2}\delta_{n,1} \tag{54}$$

while the second leads to the relation:

$$\sum_{n=o}^{\infty} C_n J_{mn} = \frac{G_m}{R^{m+2}}\frac{2(m+1)}{2m+1} \tag{55}$$

The multipole coefficients C_n of the potential inside droplet are functionals of the director angle $A(R,\theta)$ on the surface. They can be obtained from Eqs. (54) and (55):

$$C_n = \frac{4}{3}E_o\left(J^{-1}\right)_{n1} \tag{56}$$

where $\left(J^{-1}\right)_{n1}$ is the inverse of the matrix J_{mn} which is given by

$$J_{mn} = -R^{n-1}\int_0^1 P_m(x)\left\{\left[g(S)+(\Delta\varepsilon)_{max}S\cos^2 A\right]nP_n(x)+(\Delta\varepsilon)_{max}S\cos A\sin A\sqrt{1-x^2}\,\frac{dP_n(x)}{dx}\right\}dx$$
$$-R^{n-1}\frac{2n+2}{2n+1}\delta_{mn} \qquad (57)$$

and A is the director angle A(R,θ) on the surface. Then the E field inside droplet is obtained by $\vec{E}_{in}(\vec{r}) = -\vec{\nabla}\Phi_{in}(\vec{r})$, which can be written in terms of radial and tangential (θ) components as follows:

$$E_r(\vec{r}) = -\frac{\partial\Phi_{in}(\vec{r})}{\partial r} = -\sum_{n=1}^{\infty} nC_n r^{n-1}P_n(\cos\theta) \qquad (58)$$

$$E_t(\vec{r}) = \frac{1}{r}\frac{\partial\Phi_{in}(\vec{r})}{\partial\theta} = -\sum_{n=1}^{\infty} C_n r^{n-1}\frac{\partial P_n(\cos\theta)}{\partial\theta}, \qquad (59)$$

where the coefficients C_n have been calculated in Eq. (56).

The cosA(R,θ)≡f(x) with x≡cosθ in the Eq. (57) is understood to be a smooth function which can be expanded in a series of Legendre polynomials[78]:

$$f(x) = \sum_{n=0}^{\infty} b_n P_n(x) \qquad (60)$$

The smooth function f(x) is determined by the values of cosA(R,θ) at discrete values of the angle θ -- the polar angle giving the position on the surface of the spherical droplet. The best fit procedure is that f(x) is constrained by f(1)=cos(A=0)=1 on the axis. In addition, f(x) is even in x for the radial configuration and odd in x for the axial configuration since f(x) is constrained by f(0)=cos(A=0)=1 for radial configuration and f(0)=cos(A=π/2)=0 for axial configuration on the equator. Thus the n in Eq. (60) should be even for the radial configuration and odd for the axial configuration.

To obtain the coefficients b_n for f(x), we use a least squares fit to minimize the quantity

$$\sum_{i=0}^{N}\left[\sum_{n} b_n P_n(x_i) - f(x_i)\right]^2 \tag{61}$$

and $b_0 = 1 - b_2 - b_4 - b_6 - \ldots\ldots$ and $b_1 = 1 - b_3 - b_5 - b_7 - \ldots\ldots$ have been chosen for radial and axial case, respectively. Then the coefficients b_n are given by

$$b_n = \left(p^{-1}\right)_{nj} q_n \tag{62}$$

where $\left(p^{-1}\right)_{nj}$ is the inverse of the matrix $p_{nj} = \sum_i P_n(x_i)\left[P_j(x_i) - \eta\right]$ and $q_n = \sum_i f(x_i)\left[P_j(x_i) - \eta\right]$ with $\eta = P_o$ and P_1 for the radial and axial case, respectively.

Phenomenological Total Free Energy Density in Our Work

To determine the stable structure of the chosen system at constant volume, temperature, and external electric field, we have used the minimization of the phenomenological total free energy of the liquid crystal droplet, i.e. of $F_t(\vec{r}) = \int f_b dv + \int f_s ds$. Here f_s is the surface interaction term and the bulk term f_b consists of three terms: ordering f_{or}, elastic $f_{elastic}$, and electrostatic-field f_E,

$$f_b(\vec{r}) = f_{or}(\vec{r}) + f_{elastic}(\vec{r}) + f_E(\vec{r}) \tag{63}$$

The three bulk terms are essentially adopted from the Landau-de Gennes model for the isotropic-nematic transition, where the biaxiality induced by surface or by distortion is neglected. For f_{or} we use the well-known expansion in terms of the powers of the order parameter:

$$f_{or}(\vec{r}) = f_o(T) + \frac{a}{2}\left(T - T_c^*\right)S^2(\vec{r}) - \frac{b}{3}S^3(\vec{r}) + \frac{c}{4}S^4(\vec{r}) + \frac{3}{4}d\left[\vec{\nabla}S(\vec{r})\right]^2 \quad (64)$$

where $f_o(T)$ is the free energy density of the isotropic phase, and a, b, c, and $d=L_1$ are positive temperature-independent constants, and T_c^* is the temperature of supercooling limit. The bulk elastic free energy density includes the well-known Frank elastic distortion terms, Nehring-Saupe expressions (Eq. (19)) omitting splay-bend contribution, and the coupling terms of the director $\hat{n}(\vec{r})$ and order parameter $S(\vec{r})$ from the F_{cp} of the Landau-de Gennes free energy density (Eq. (30)):

$$\begin{aligned} f_{elastic}(\vec{r}) = {} & \frac{1}{2}\left\{K_{11}\left[\vec{\nabla}\cdot\hat{n}(\vec{r})\right]^2 + K_{22}\left[\hat{n}(\vec{r})\cdot\vec{\nabla}\times\hat{n}(\vec{r})\right]^2 + K_{33}\left[\hat{n}(\vec{r})\times\vec{\nabla}\times\hat{n}(\vec{r})\right]^2\right\} \\ & -\frac{1}{2}K_{24}\vec{\nabla}\cdot\left\{\hat{n}(\vec{r})\left[\vec{\nabla}\cdot\hat{n}(\vec{r})\right] + \left[\hat{n}(\vec{r})\times\nabla\times\hat{n}(\vec{r})\right]\right\} \\ & +\frac{3}{8}e\left[\hat{n}(\vec{r})\cdot\vec{\nabla}S(\vec{r})\right]^2 + \frac{3}{4}eS(\vec{r})\left\{2\left[\vec{\nabla}\cdot\hat{n}(\vec{r})\right]\left[\hat{n}(\vec{r})\cdot\vec{\nabla}S(\vec{r})\right] + \left[\hat{n}(\vec{r})\times\vec{\nabla}\times\hat{n}(\vec{r})\right]\cdot\vec{\nabla}S(\vec{r})\right\} \end{aligned} \quad (65)$$

where $K_{11} \cong k_{11}S^2$, $K_{22} \cong k_{22}S^2$, $K_{33} \cong k_{33}S^2$, and $K_{24} \cong k_{24}S^2$ when we take account into the spatially dependent order parameter. $e = L_2 \cong (4/9)\cdot 1/2\left(k_{11} + k_{33}\right)$ is modified by suppressing the twist related constant L_1 in Eq. (29). It should be stressed that (as is customary) we have allowed for the three different Frank elastic constants K_{11}, K_{22}, and K_{33} for the splay, twist, and bend distortions instead of the same values for splay and bend constants of the free energy density $F_{F\text{-}e}$ shown in Eq. (29). In addition, we have included the saddle-splay $\left(K_{24}\right)$ contribution according to the Saupe's paper[73] in 1981. The nematic director, which enters into the $f_{elastic}$, can be generally expressed in a spherical coordinate system as

$$\hat{n}(\vec{r}) = \cos A\hat{r} - \sin A\cos B\hat{\theta} + \sin A\sin B\hat{\varphi} \quad (66)$$

with $\hat{r}, \hat{\theta}$, and $\hat{\varphi}$ unit vectors of the spherical coordinate system whose polar axis lies along the direction of the external electric field, the angle $A=A(r,\theta)$ between $\hat{r}$ and $\hat{n}$, and the twist-related angle $B=B(r,\theta)$, the amount that the director rotates out to the $\hat{\theta}$-$\hat{\varphi}$ plane. (Figure 8)

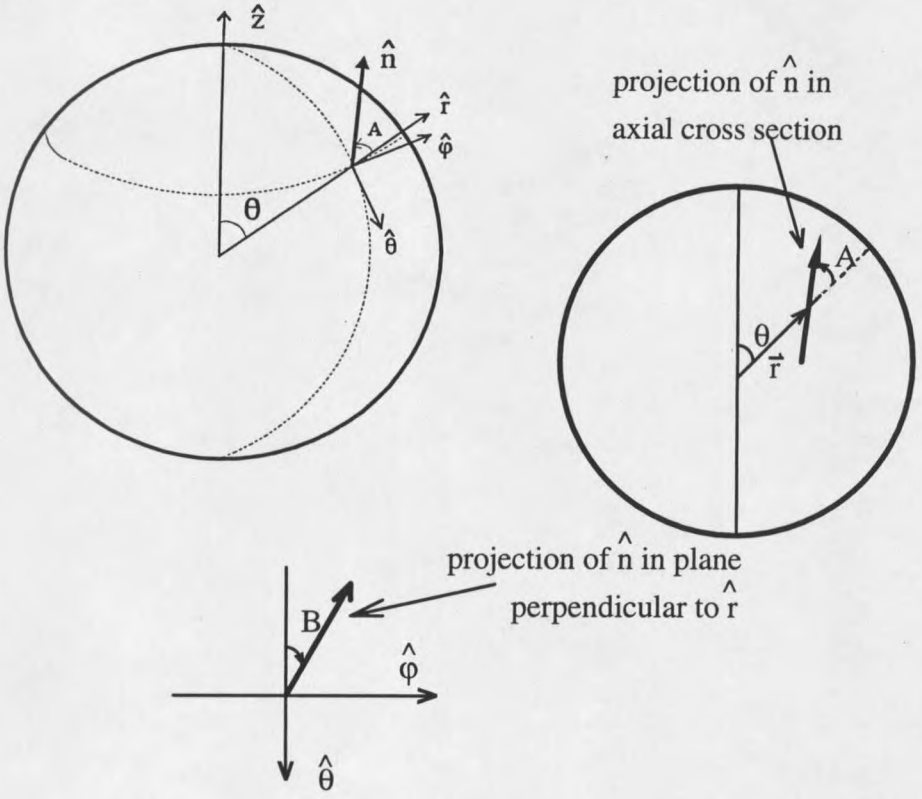

Figure 8. Orientation of the director field $\hat{n}(\vec{r})$ may be specified by the angle $A(r,\theta)$ between $\hat{n}$ and $\hat{r}$ and the twist-related angle $B(r,\theta)$.

In the case with the no-twist assumption the expression of the director becomes

$$\hat{n}(\vec{r}) = \cos A\hat{r} - \sin A\hat{\theta} \tag{67}$$

The electrostatic-field contribution f_E is

$$f_E(\vec{r}) = -\frac{1}{8\pi}\vec{E}(\vec{r})\cdot\vec{\varepsilon}\cdot\vec{E}(\vec{r}) = -\frac{1}{8\pi}E^2\left[\varepsilon_\perp + \Delta\varepsilon(\hat{n}\cdot\hat{e}_E)^2\right] \quad (68)$$

where the dielectric tensor $\vec{\varepsilon}$ is defined in Eq. (41). The direction of electric field can be written as

$$\hat{e}_E = \cos\theta_E\hat{r} - \sin\theta_E\hat{\theta} \quad (69)$$

where the angle θ_E and the magnitude of electric field $E(\vec{r})$ can be obtained from the radial and tangential components of the electric field, which was calculated in Eq. (58) and Eq. (59).

To describe weak anchoring, we take the term for the surface interaction between the liquid crystal and the surrounding medium to be linearly dependent on the order parameter and expressible in the Rapini-Papoular form of the anchoring energy[79-84]:

$$f_s = -\frac{1}{2}W_o S(\vec{r})\left[\hat{n}(\vec{r})\cdot\hat{r}\right]^2\delta(r-R), \quad (70)$$

where W_o is the anchoring strength (>0 for homeotropic surface anchoring, <0 for tangential surface anchoring) and R the droplet radius.

The equilibrium value S_o can be obtained by minimizing the homogeneous part f_h of the free energy density:

$$f_h = f_o(T) + \frac{a}{2}(T-T^*)S^2(\vec{r}) - \frac{b}{3}S^3(\vec{r}) + \frac{c}{4}S^4(\vec{r}) \quad (71)$$

with respect to S. This means that S_o is determined by the equation

$$a(T-T_o^*)S_o - bS_o^2 + cS_o^3 = 0 \quad (72)$$

The solutions are

$$S_o = 0 \quad \text{the isotropic phase,} \tag{73}$$

$$S_o^{\pm} = \frac{b \pm \sqrt{b^2 - 4ac\left(T - T^*\right)}}{2c}. \tag{74}$$

The S_o^+ solution is the correct solution describing the temperature dependence of the order parameter in the nematic phase.

CHAPTER 3

NUMERICAL METHODS

Introduction

In the phenomenological approach, the stable phases and configurations of microconfined liquid crystals are determined by finding the structures which have the minimum free energy. The minimization of the total free energy of a liquid crystal is used to determine possible stable and metastable structures. This procedure can be done numerically, here with relaxation or conjugate gradient techniques to obtain the director $\hat{n}(\bar{r})$ and order parameter $S(\bar{r})$ configurations. The relaxation methods can be performed either directly, or by solving the corresponding Euler-Lagrange differential equations.

Finite Difference Method for Discretizing[85]

The ultimate goal of discrete methods is the reduction of continuous systems to 'equivalent' discrete systems which are suitable for high-speed computer solution. In addition, since the solution is not in closed form we use a discrete method to deal with the continuum problem of the total free energy for numerical analysis. The finite difference method has been adopted to approximate the free energy expression at a discrete set of

coordinate points defined on a two-dimensional computational grid (Δr, $\Delta\theta$), ranging from 10×10 to 100×100 in our work. The computational grid separations Δr_i and $\Delta\theta_j$ are constant. (Figure 9)

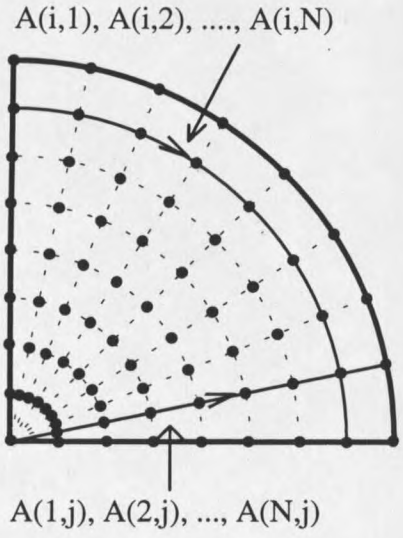

Figure 9. The computational grid in one quadrant of an axial cross section of a sphere.

Due to simplification we shall derive finite differences in one dimension. In similar fashion this method is easily extended to a two-dimensional grid (Δr, $\Delta\theta$). The calculus of finite differences employs the fundamental ideas of ordinary calculus up to the taking of the limit $\Delta x\to0$. In the approximation the Δx's are treated as small quantities and called truncation errors, whose presence will be signified by employing the asymptotic O notation. To obtain an approximate expression for the derivative of a function, for instance A'(x), we start with the Taylor series expansion written as

$$A(x+\Delta x)=A(x)+A'(x)\Delta x+A''(x)\frac{\Delta x^2}{2!}+A'''(x)\frac{\Delta x^3}{3!}+\ldots\ldots, \qquad (75)$$

i.e.

$$A'(x) = \frac{A(x+\Delta x) - A(x)}{\Delta x} + O(\Delta x) \tag{76}$$

The forward difference of Eq. (76) provides the simple first order approximation..

FORWARD:

$$A'(x_i) = \frac{A(x_{i+1}) - A(x_i)}{\Delta x} + O(\Delta x), \tag{77}$$

$$\text{i.e. } A'_i = \frac{\Delta A_i}{\Delta x} = \frac{(A_{i+1} - A_i)}{\Delta x} + O(\Delta x), \tag{78}$$

where $\Delta A_i = (A_{i+1} - A_i)$ is the first forward difference between the point (x_i, A_i) and the next point (x_{i+1}, A_{i+1}). The second derivative A"(x) can also be written as

$$A''_i = \frac{\Delta^2 A_i}{(\Delta x)^2} + O\left[(\Delta x)^2\right], \tag{79}$$

where the second forward difference is

$$\begin{aligned} \Delta^2 A_i &= \Delta(\Delta A_i) \\ &= \Delta(A_{i+1} - A_i) \\ &= \Delta A_{i+1} - \Delta A_i \\ &= (A_{i+2} - A_{i+1}) - (A_{i+1} - A_i) \\ &= (A_{i+2} - 2A_{i+1} + A_i) \end{aligned} \tag{80}$$

The alternatives for A'(x) and A"(x) with the backward and central differences can be obtained by replacing Δx by $-\Delta x$ in Eq. (76) and by averaging the equations for forward and backward differences, respectively.

BACKWARD:

$$A'(x_i) = \frac{A(x_i) - A(x_{i-1})}{\Delta x} + O(\Delta x), \tag{81}$$

$$\text{i.e. } A'_i = \frac{\nabla A_i}{\Delta x} = \frac{(A_i - A_{i-1})}{\Delta x} + O(\Delta x). \tag{82}$$

$$A''_i = \frac{\nabla^2 A_i}{(\Delta x)^2} = \frac{(A_i - 2A_{i-1} + A_{i-2})}{(\Delta x)^2} + O\left[(\Delta x)^2\right], \tag{83}$$

where $\nabla A_i = (A_i - A_{i-1})$ is the first backward difference and $\nabla^2 A_i = (A_i - 2A_{i-1} + A_{i-2})$ the second backward difference.

CENTRAL:

$$A'_i = \frac{\delta A_i}{\Delta x} + O\left[(\Delta x)^2\right], \tag{84}$$

where the first central difference is defined as:

$$\begin{aligned} \delta A_i &\equiv \frac{1}{2}(\Delta A_i + \nabla A_i) \\ &= \frac{1}{2}\left[(A_{i+1} - A_i) - (A_i - A_{i-1})\right] \\ &= \frac{1}{2}(A_{i+1} - A_{i-1}). \end{aligned} \tag{85}$$

$$A''_i = \frac{\delta^2 A_i}{(\Delta x)^2} + O\left[(\Delta x)^2\right], \tag{86}$$

where the second central difference is

$$\begin{aligned} \delta^2 A_i &= \frac{1}{2}\left[\Delta^2 A_{i-1} + \nabla^2 A_{i+1}\right] \\ &= \frac{1}{2}\left[(A_{i+1} - 2A_i + A_{i-1}) + (A_{i+1} - 2A_i + A_{i-1})\right] \\ &= (A_{i+1} - 2A_i + A_{i-1}). \end{aligned} \tag{87}$$

Approximate expressions for the derivatives of a function A(x) at a point x_i are summarized as follows:

	BACKWARD	CENTRAL	FORWARD
$\left(\frac{\partial A}{\partial x}\right)_i$	$\frac{(A_i - A_{i-1})}{\Delta x}$	$\frac{(A_{i+1} - A_{i-1})}{2\Delta x}$	$\frac{(A_{i+1} - A_i)}{\Delta x}$
$\left(\frac{\partial^2 A}{\partial x^2}\right)_i$	$\frac{(A_i - 2A_{i-1} + A_{i-2})}{(\Delta x)^2}$	$\frac{(A_{i+1} - 2A_i + A_{i-1})}{(\Delta x)^2}$	$\frac{(A_{i+2} - 2A_{i+1} + A_i)}{(\Delta x)^2}$

Table 1. The derivatives of a function A(x) with respect to x.

Similarly, the approximate expressions of finite differences for the derivatives of the director $\hat{n}(r_i, \theta_j)$ with respect to r_i and θ_j can be summarized in Table 2. The derivatives of order parameter $S(r_i, \theta_j)$ with respect to r_i and θ_j can be obtained in the same fashion.

	BACKWARD	CENTRAL	FORWARD
$\left(\frac{\partial n}{\partial r}\right)_{i,j} \approx$	$\frac{(n_{i,j} - n_{i-1,j})}{\Delta r}$	$\frac{(n_{i+1,j} - n_{i-1,j})}{2\Delta r}$	$\frac{(n_{i+1,j} - n_{i,j})}{\Delta r}$
$\left(\frac{\partial n}{\partial \theta}\right)_{i,j} \approx$	$\frac{(n_{i,j} - n_{i,j-1})}{\Delta \theta}$	$\frac{(n_{i,j+1} - n_{i,j-1})}{2\Delta \theta}$	$\frac{(n_{i,j+1} - n_{i,j})}{\Delta \theta}$
$\left(\frac{\partial^2 n}{\partial r^2}\right)_{i,j} \approx$	$\frac{(n_{i,j} - 2n_{i-1,j} + n_{i-2,j})}{(\Delta r)^2}$	$\frac{(n_{i+1,j} - 2n_{i,j} + n_{i-1,j})}{(\Delta r)^2}$	$\frac{(n_{i+2,j} - 2n_{i+1,j} + n_{i,j})}{(\Delta r)^2}$
$\left(\frac{\partial^2 n}{\partial \theta^2}\right)_{i,j} \approx$	$\frac{(n_{i,j} - 2n_{i,j-1} + n_{i,j-2})}{(\Delta \theta)^2}$	$\frac{(n_{i,j+1} - 2n_{i,j} + n_{j,j-1})}{(\Delta \theta)^2}$	$\frac{(n_{i,j+2} - 2n_{i,j+1} + n_{i,j})}{(\Delta \theta)^2}$

Table 2. The derivatives of the director field with respect to r_i and θ_j.

In the region of interest, one quadrant of an axial cross section of sphere, we adopt the central differences for the derivatives of $\hat{n}(\bar{r})$ and $S(\bar{r})$ with respect to r and θ, i.e. $\partial n/\partial r$, $\partial^2 n/\partial r^2$, $\partial n/\partial \theta$, $\partial^2 n/\partial \theta^2$, $\partial S/\partial r$, $\partial^2 S/\partial r^2$, $\partial S/\partial \theta$, and $\partial^2 S/\partial \theta^2$, except the region

closest to the boundary. The backward differences have been adopted for the equator and the surface. In addition, the forward differences are used at the axis. The reason is that we have assigned A(1,j) to the node of the center and A(N,j) to the node of the surface along the radial direction by increasing a constant radial segment Δr (i.e. $r_i = (i-1)\Delta r$, with $i = 1,2,\ldots,N$) at a certain polar angle $\theta_j = \pi/2 \cdot [(j-1)/(N-1)]$. In addition, A(i,1), A(i,2), A(i,3), ..., A(i,N) represent the nodes from the axis to the equator along the polar direction by increasing a constant polar segment $\Delta\theta$, i.e. $\theta_j = (j-1)\Delta\theta$, with $j = 1,2,\ldots,N$) at a certain radial distance from the center, i.e. $r_i = R \cdot [(i-1)/(N-1)]$, where N is the grid's size and R is the radius of the nematic droplet. (see Figure 9)

Relaxation Method for Root Solving

Whichever method of minimization we use, either direct minimization or indirect minimization done by solving the corresponding Euler-Lagrange differential equations, a relaxation method may be used for solving numerically the roots of the equations $f(x) = 0$. For direct minimization the derivatives of the total free energy with respect to the local variables, such as the director angles: $A(r_k, \theta_l)$ $(\equiv A_{kl})$ and $B(r_k, \theta_l)$ $(\equiv B_{kl})$, are set equal to zero, i.e.,

$$\frac{\partial F_{total}(A_{ij}, B_{ij})}{\partial A_{kl}} = 0 \tag{88}$$

$$\frac{\partial F_{total}(A_{ij}, B_{ij})}{\partial B_{kl}} = 0 \tag{89}$$

The Euler-Lagrange differential equations are two nonlinear coupled partial differential equations for the director field in the bulk (Eq. (98)) and on the surface (Eq. (99)). To

solve for the roots of these equations, we use a Newton's relaxation method. Newton's method can be derived by starting with the Taylor series for the function f(x) expanded around the given point x_o:

$$f(x) = f(x_o) + \frac{df}{dx}\Big|_{x=x_o}(x - x_o) + \frac{1}{2!}\frac{d^2f}{dx^2}\Big|_{x=x_o} + \ldots\ldots \tag{90}$$

To find a root of the function, we seek an x such that f(x)=0 and assume that $|x - x_o|$ is small, i.e. the desired root x is near the value x_o. Then

$$f(x) = 0 \cong f(x_o) + \frac{df}{dx}\Big|_{x=x_o}(x - x_o) \tag{91}$$

or

$$x = x_o - \frac{f(x_o)}{\left[\frac{df}{dx}\Big|_{x=x_o}\right]}. \tag{92}$$

Replacing the function f(x) by the first two terms in its Taylor series is equivalent to approximating the function by a straight line, through the point $(x_o, f(x_o))$, which has the same slope as the tangent to the curve at that point. Then setting this approximation to f(x) =0, we find the point where the line intersects the axis. (Figure 10) This procedure will not in general give the actual root of f(x)=0, but the value generated by Eq. (92) is closer to the actual root than was the starting point x_o.

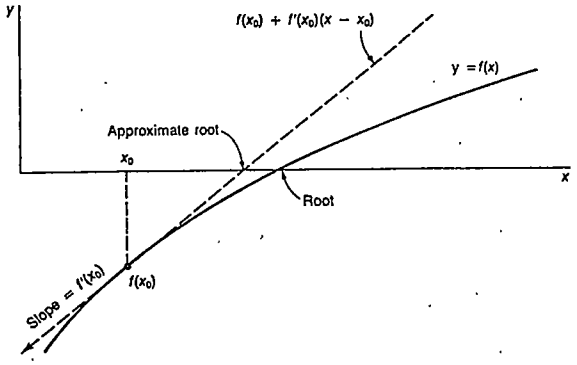

Figure 10. Replacing a function by two terms of a Taylor series.

Newton's method consists of repeating this process; that is, starting from an initial guess for the root of f(x) to calculate an improved guess from Eq. (92). Next use the improved value for the root in the next cycle to calculate the new improvement on the root, and so on, until the difference between new value and old value are less than some chosen number, that is, until the iteration is convergent. The Newton's algorithm can be expressed as the formula:

$$x^{(n+1)} = x^{(n)} - \frac{f\left(x^{(n)}\right)}{f'\left(x^{(n)}\right)}, \tag{93}$$

where (n+1) and (n) denote the (n+1)th and nth step in the iteration, respectively. It also can be shown that the convergence rate of Newton's method is second order[85].

A more efficient relaxation method, called successively over-relaxed (SOR) Gauss-Seidel iteration[86], is defined by

$$x^{(n+1),SOR} = x^{(n)} - (\omega_{over})\frac{f\left(x^{(n)}\right)}{f'\left(x^{(n)}\right)}, \tag{94}$$

where $0 < \omega_{over} < 2$ and the optimal value of ω_{over} is 1 for the initial several iterations and about 1.5 to 1.8 for later iterations.

The iteration can be explained as follows. Let us repeatedly sweep through the x_k, proceeding from x_1 to x_N and then starting over again with x_1,

$x_1, x_2, \ldots\ldots\ldots\ldots, x_N; x_1, x_2, \ldots\ldots\ldots\ldots, x_N; \ldots\ldots\ldots$

First sweep ; second sweep ; .....

at each step replacing the variable x_i being considered by the value which minimizes the function f when all other variables x_k ($k \neq i$) are held fixed. That is, we sweep through the mesh repeatedly and adjust the variables at each node with a single iteration, using the most current values for the node variables at the adjacent points in the calculation of the derivative, until convergence.

In the implementation of Newton's method, we also adopt an annealing process for surface anchoring strength to avoid the divergence caused by large changes of the initial condition which are such that $f'(x^{old})$ is small. That is, we introduce the anchoring parameter incrementally, until the desired value is reached.

Conjugate Gradient Method[87] for Direct Minimization

Our task is to find directly a minimum of the total free energy. Starting with any set of initial parameter space (that is, node variables such as director angles $A(r_i, \theta_j)$, $B(r_i, \theta_j)$, and order parameter $S(r_i, \theta_j)$), a reasonable procedure is to move "downhill" in parameter space, where the gradient of the total free energy with respect to the parameters is used to identify the direction of steepest decrease of F_{total}. This may be done iteratively to search for a minimum. The conjugate gradient method is a technique that accomplishes the procedure of minimization in a direction that is constructed to be conjugate to the old gradient, as well as to all previous direction traversed. (Figure 11)

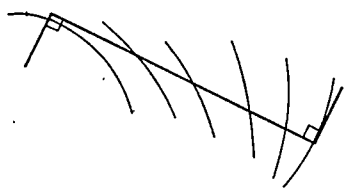

Figure 11. Magnified view of one step in the conjugate gradient technique: a step starts off in the local gradient direction, perpendicular to the contour lines, and traverses a straight line until a local minimum is reached, where the line is parallel to the local contour lines.

We adopt the Polak-Ribiere method[87] to find the successively conjugate directions along which to line-minimize in our work.

The conjugate directions are briefly said to be the "non-interfering" directions. To define mathematically the conjugate directions, we start with the Taylor series expansion for any function $f(\vec{x})$ around the point $\vec{P}$:

$$\begin{aligned} f(\vec{x}) &= f(\vec{P}) + \sum_i \left[\frac{\partial f}{\partial x_i}\right]_{\vec{P}} x_i + \frac{1}{2}\sum_{i,j}\left[\frac{\partial^2 f}{\partial x_i \partial x_j}\right]_{\vec{P}} x_i x_j + \ldots\ldots \\ &\approx f(\vec{P}) - \vec{b}\cdot\vec{x} + \frac{1}{2}\vec{x}\cdot\vec{A}\cdot\vec{x} + O(\delta x^2) \end{aligned} \tag{95}$$

where $$b \equiv -[\nabla f]_{\vec{P}} \text{ and } \vec{A} \equiv \left[\frac{\partial^2 f}{\partial x_i \partial x_j}\right]_{\vec{P}} \tag{96}$$

Then in the approximation of Eq. (95), the gradient of f near $\vec{p}$ is $\nabla f = \vec{A}\cdot\vec{x} - b$. Suppose that we have moved along some direction $\vec{u}$ to a minimum and now propose to move along some new direction $\vec{v}$. The condition that motion along $\vec{v}$ not spoil our minimization along $\vec{u}$ is just that the gradient stay perpendicular to $\vec{u}$, i. e.

$$0 = \vec{u}\cdot\delta(\nabla f) = \vec{u}\cdot\vec{A}\cdot\vec{v} \tag{97}$$

where $\vec{u}$ and $\vec{v}$ are said to be conjugate. When the conjugate relation holds pairwise for all members of a set of vectors, they are called a conjugate direction set.

If the sizes of the set of node variables, such as the director angle $A(r_i, \theta_j)$ and the order parameter $S(r_i, \theta_j)$, are N, then each parameter set will have size of $2N^2$. Storage memory of size $2N^2$ is needed for the nodes, the function and the gradient of the function in each line minimization. But each calculated component of the gradient will typically save not just one function evaluation, equivalent to, say a whole line minimization.

Therefore the conjugate gradient method is faster than the relaxation method for parameter sets of small size but slower for the large parameter sets.

Errors[88]

There are two types of errors in the numerical calculations. The error in the solution due to replacement of the continuous problem by the discrete model, is called the discretization error. When the discrete equations are not solved exactly an additional error is introduced. This error, called round-off error, is present in iterative solutions (machine or manual) since the iteration is only continued until no change takes place up to a certain number of digits. If the iteration is continued without decimal place limitation, any subsequent changes are considered to be round-off errors. The mesh sizes of Δr and $\Delta\theta$ affect the discretization error and round-off error in the opposite sense. The discretization error decreases as the mesh size decreases, while the round-off error generally increases. Therefore one cannot generally assert that decreasing the mesh size always increase the accuracy.

General Description of Minimization Methods Adopted in Our Work

Indirect Minimization

Due to quick convergence of the iteration in a finer computational grid, the indirect minimization done by solving the Euler-Lagrange differential equations with the relaxation method is adopted for mesh sizes up to 100×100. With the assumptions of constant order parameter and no twist contribution, we use the variational method to

obtain the set of the Euler-Lagrange differential equations for the droplet bulk and surface , as follows:

Bulk:

$$\left(\sin^2 A + k_{33}\cos^2 A\right)\left[\frac{\partial^2 A}{\partial \rho^2} + 2\frac{\partial A}{\partial \rho}\right] + \left(\cos^2 A + \sin^2 A\right)\left[\frac{\partial^2 A}{\partial \theta^2} + \frac{\partial A}{\partial \theta}\cot\theta\right]$$
$$-\frac{\sin 2A}{2}\left(\cot^2\theta - 1\right) - \left(1 + k_{33}\right)\cot A \sin^2 A$$
$$+\frac{\left(1 - k_{33}\right)}{2}\left\{\sin 2A\left[\rho^2\left(\frac{\partial A}{\partial \rho}\right)^2 + \rho\frac{\partial A}{\partial \rho}\cot\theta - \left(\frac{\partial A}{\partial \theta}\right)^2 + \frac{\partial A}{\partial \theta} + 2\rho\frac{\partial^2 A}{\partial \rho \partial \theta}\right] + 2\cos 2A\frac{\partial A}{\partial \rho}\frac{\partial A}{\partial \theta}\rho\right\}$$
$$-\frac{R^2\rho^2}{K_{11}}\frac{\Delta\varepsilon E^2}{8\pi}\sin\left[2\left(A - \theta_E\right)\right] = 0 \qquad (98)$$

Surface:

$$\frac{\partial A}{\partial \rho}\left(\sin^2 A + k_{33}\cos^2 A\right) + \frac{\partial A}{\partial \theta}\left(1 - k_{33}\right)\sin A\cos A - \cos A\sin A\left(2 - k_{33}\right) + \cot\theta\sin^2 A$$
$$+\frac{RW_o}{K_{11}}\cos A\sin A + k_{24}\left(\sin 2A - \cot\theta\sin^2 A\right) = 0, \qquad (99)$$

where W_o is the surface anchoring strength. In addition, dimensionless ratios $k_{33} = K_{33}/K_{11}$ and $k_{24} = K_{24}/K_{11}$ are elastic-force-related parameters. $\rho = r/R$ and RW_o/K_{11} are dimensionless position and anchoring strength parameters, respectively. $A=A(\rho,\theta)$ is the director angle defined in Eq. (67). $E=E(\rho,\theta)$ and θ_E are the magnitude and the direction angle of the electric field, respectively. We have performed the variational integral with a variable end point (i.e., $A(\rho,\theta)_{\rho=1}$ is a variable) to obtain the surface differential equation. When the system is "discretized" (replacing such functions as $A(\rho,\theta)$ by values at discrete points, or nodes), there is one Euler-Lagrange equation for each node, and these coupled nonlinear equations must be solved simultaneously. This is done by relaxation, as discussed in the earlier section. Minimization by solving the Euler-

Lagrange equations (Eqs. (98) and (99)) has been adopted in the following cases in our work:

(I) nonuniform-field approach:

(a) with splay and bend contributions for $K_{33}/K_{11}=1$ and $K_{33}/K_{11}=2$.

(b) with splay, bend, and saddle-splay contributions for $K_{24} = K_{11} = K_{33}$.

(II) uniform-field approximation:

(a) with splay and bend contributions for $K_{33}/K_{11}=1$ and $K_{33}/K_{11}=2$.

(b) with splay, bend, and saddle-splay contributions for $K_{24} = K_{11} = K_{33}$.

The difference between the nonuniform- and uniform-field approach is obtained by comparing the two cases above.

Direct Minimization

The goal of direct minimization is to find directly the total free energy minimum instead of solving the Euler-Lagrange differential equations. It can be executed either by setting the derivatives of the total free energy with respect to the local variables to zero and solving the equations by the relaxation method, or by using another minimization technique (e.g. conjugate gradient method) to directly find the minimum total free energy with any set of initial node variables, as discussed in earlier section.

To add sequentially the contributions of the free energy densities into the numerical calculation we mainly use the conjugate gradient technique for direct minimization, which only requires derivatives up to first order. The conjugate gradient technique for direct minimization of the total free energy functional has been adopted for the following cases:

1. director field in the assumption of uniform order parameter:

(1) with splay (K_{11}) and bend (K_{33}) contributions but no twist and saddle-splay contributions: Suppressing the twist contribution simplifies the calculation, because the director angle related to the twist deformation is omitted to reduce the size of the parameter set, which would require more computer memory. After understanding the splay and bend deformations, we sequentially add twist and saddle-splay contributions into the total free energy. Comparing the phase diagrams for $K_{33}/K_{11} = 1$ and $K_{33}/K_{11} = 2$, we can understand the influence of bend-to-splay ratio on the phase transition. This case can also be used to understand the difference between the relaxation and conjugate gradient methods, by comparing this case with the case (I-(a)).

(2) with splay (K_{11}), twist (K_{22}), and bend (K_{33}) contributions but no saddle-splay contribution:

$$K_{22} = K_{11} = K_{33}$$

$$K_{22} = K_{11} = K_{33} / 2$$

$$K_{22} = K_{11} = K_{33} / 3$$

In this calculation, we see the influence of twist deformation on the phase transition and understand that the bend-to-splay ratio plays a more important role in the phase transition than the twist-to-splay ratio.

(3) with splay (K_{11}), twist (K_{22}), bend (K_{33}), and saddle-splay (K_{24}) contributions: We explore the important influence of the saddle-splay deformation for a weak anchoring strength parameter. In addition, we understand that twist contribution has significant influence if the splay elastic constant is large compared to the sum of twist and bend for strong anchoring.

$$K_{24} = K_{11} = K_{33}$$

$$K_{24} / 2 = K_{11} = K_{33}$$

$$K_{24} = K_{11} = K_{33} / 2$$

$K_{24}/2 = K_{11} = K_{33}/2$

$K_{24} = K_{22} = K_{11} = K_{33}$

$K_{24} = K_{11} = K_{22}/0.5 = K_{33}/0.5$

$K_{24} = K_{11} = K_{22}/0.5 = K_{33}$

2. order parameter allowed to vary spatially:

(1) without coupling between $\hat{n}(\vec{r})$ and $S(\vec{r})$ for $K_{33}/K_{11} = 1$: The influence of the order parameter $S(\vec{r})$ on the phase transition can be obtained.

(2) with full coupling between $\hat{n}(\vec{r})$ and $S(\vec{r})$ for $K_{33}/K_{11} = 1$ and $K_{24} = K_{22}/0.5 = K_{11} = K_{33}/0.5$: The influence of the coupling between $\hat{n}(\vec{r})$ and $S(\vec{r})$ on the phase transition in the assumption of no twist contribution can be obtained.

(3) for tangential anchoring with variable director field $\hat{n}(\vec{r})$ (but no twist and no saddle-splay contributions), position-dependent order parameter $S(\vec{r})$, and full coupling between $\hat{n}(\vec{r})$ and $S(\vec{r})$: We omit the twist and saddle-splay to simplify the calculation and see the defect created by the suppression of the order parameter $S(\vec{r})$.

Summary of Numerical Minimization Procedure

According to the symmetry of radial and axial configurations, in a single quadrant of an axial cross section, the director angle $A(r_i, \theta_j)$ is fixed to be zero on the equator for the radial case, $\pi/2$ on the equator for the axial case, and zero on the axis for both configurations.

The procedure of our numerical minimization in the discretized system can be summarized as follows:

(1) discretize the total free energy density or the Euler-Lagrange equations.

(2) calculate the coefficients in the multipole expansion of the potential for a given surface configuration of order parameter $S(\vec{r})$ and director $\hat{n}(\vec{r})$.

(3) find the electric field $E(r,\theta)$ within the droplet from the potential.

(4) vary $\hat{n}(\vec{r})$, $S(\vec{r})$ at each node to minimize F_{total} for given $E(r,\theta)$,

(a) solving Euler-Lagrange differential equations by using relaxation method at each node, or

(b) using direct relaxation at each node, or

(c) using conjugate gradient technique for direct minimization.

(5) if convergence is not reached, return to (2); otherwise, output free energy and equilibrium configuration.

(6) compare the total free energies of radial and axial configurations to determine the stable phase.

(7) map out the phase boundary.

CHAPTER 4

RESULTS AND DISCUSSIONS

Introduction

For calculations we used characteristic parameters of the common nematic liquid crystal 5CB in Eq. (64) as follows: $a = 1.3 \times 10^6 \text{ erg}/(\text{cm}^3\text{K})$, $b = 1.836 \times 10^7 \text{ erg}/\text{cm}^3$, $c = 4.05 \times 10^7 \text{ erg}/\text{cm}^3$, $d = L_1 = 6.0 \times 10^{-7} \text{ erg}/\text{cm}$, $\Delta T = (T - T^*) \approx 1$. (Reference 16) We also adopted typical droplet parameters: the Frank elastic constant for splay deformation $K_{11} = 5 \times 10^{-7}$ dyne, the radius $R = 1\mu\text{m}$, the dielectric anisotropy $\Delta\varepsilon = 13.8$ (below 1k Hz), the perpendicular component of dielectric constant $\varepsilon_\perp = 5.2$, since exact values of these parameters are not available.

The following dimensionless parameters are adopted throughout the results and discussions:

(1) the ratio of bend to splay K_{33}/K_{11}, twist to splay K_{22}/K_{11}, and saddle-splay to splay K_{24}/K_{11} measuring the relative elastic forces.

(2) the surface anchoring strength parameter $\mu = R/d = RW_o/K_{11}$ measuring the relative anchoring strength, where $d = K_{11}/W_o$ is the extrapolation length.

(3) the field strength parameter $\zeta = d/\xi = (E/W_o)\sqrt{\Delta\varepsilon K_{11}/4\pi} = (ER/\mu)\sqrt{\Delta\varepsilon/4\pi K_{11}}$ measuring the relative electric field strength, where $\xi = (1/E)\sqrt{4\pi K_{11}/\Delta\varepsilon}$ is the correlation length over which the ordering (induced by a surface) persists in the field.

In the nonuniform-field approach the magnitude of E field in the interior of the droplet is estimated as

$$E \cong -\frac{8\pi p_o}{(\bar{\varepsilon}+2)}, \text{ with } \bar{\varepsilon} \cong \varepsilon_\perp + \Delta\varepsilon. \tag{100}$$

Thus,

$$E \cong -\frac{8\pi p_o}{(\varepsilon_\perp + \Delta\varepsilon + 2)} = \frac{2E_o}{(\varepsilon_\perp + \Delta\varepsilon + 2)}, \tag{101}$$

where $E_o = -4\pi p_o$ is involved in the calculation of Eq. (56). The order parameter comes into play through $\Delta\varepsilon = (\Delta\varepsilon)_{max} S$ when the spatially dependent order parameter $S(\bar{r})$ is taken into account.

Our basic results are phase diagrams which summarize information concerning the stable or metastable configurations of the director and order parameter fields and are derived from the free energies of the radial and axial structures as functions of anchoring strength parameter μ for certain values of field strength parameter ζ or as functions of ζ for certain values of μ.

In this Chapter we first calculate results for a "perfect phase" model, comparing the free energies of "perfectly" radial and "perfectly" axial configurations in a uniform field in order to understand the phase diagram qualitatively. We then discuss the nonuniformity of the electric field inside the droplet and how the elastic constants affect the inhomogeneity of the electric field. Then we discuss phase diagrams where the electric field induces the transition between radial and axial phases and explore how the elastic constants (K_{11}, K_{22}, K_{33}, and K_{24}) and the spatially dependent order parameter $S(\bar{r})$ affect the phase transition. Finally we study how a point defect suppresses the order parameter

in the case of tangential surface anchoring. We discuss the homeotropic surface anchoring for all sections in this Chapter except the final section.

"Perfect Phase" Model[89] and Uniform-Field Case

Before exploring the phase transition between radial and axial phases induced by the dimensionless field ζ and anchoring strength μ parameters, we would like to understand the reentrant phase diagram for a droplet in the uniform-field and uniform-order-parameter approximation.

We start with the assumption of "perfect" radial and axial patterns and ignore any distortion of the radial pattern by the field, or of the axial pattern by the anchoring. There is only pure splay elastic deformation in the perfectly radial phase and no elastic deformations in the perfectly axial phase (or perfectly uniform configuration), as shown in Figure 12:

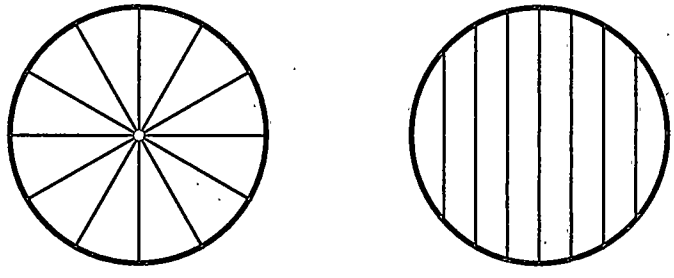

perfectly radial perfectly uniform

Figure 12. Director configurations for the perfectly radial phase and the perfectly uniform phase.

Thus the free energy of the perfectly radial phase in the uniform-field approach consists of contributions from bulk elastic energy, surface anchoring, and the electric field:

$$F_{radial} = f_{elastic} + f_s + f_E$$
$$= 8\pi K_{11} R - \frac{1}{2} W_o 4\pi R^2 - \frac{1}{8\pi} \bar{\varepsilon} E^2 \cdot \frac{4\pi}{3} R^3, \quad (102)$$

where $\bar{\varepsilon} = (\varepsilon_{//} + 2\varepsilon_{\perp})/3$. Similarly, the free energy of the perfectly uniform phase can be written as:

$$F_{axial} = f_{elastic} + f_s + f_E$$
$$= 0 - \frac{1}{2} W_o \cdot \frac{4\pi R^2}{3} - \frac{1}{8\pi} \varepsilon_{//} E^2 \cdot \frac{4\pi}{3} R^3 \quad (103)$$

To obtain the phase boundary we compare the energies of the perfectly radial and perfectly uniform configurations:

$$\Delta F = F_{axial} - F_{radial} = -8\pi K_{11} R + \frac{4\pi}{3} W_o R^2 - \frac{8\pi}{9} \Delta\varepsilon E R^3 \quad (104)$$

Then the locus of the solution in the μ-ζ plane of the equation

$$\frac{1}{6}\zeta^2 \mu^2 - \frac{1}{2}\mu + 3 = 0 \quad (105)$$

gives the phase diagram shown in Figure 13. It is interesting to note that the qualitative features of the phase diagram shown in Figure 14 emerge from this simplest of models. Eq. (105) gives as the phase boundary

$$\mu = \frac{3}{2\zeta^2}\left(1 \pm \sqrt{1 - 8\zeta^2}\right), \quad (106)$$

which indicates the maximum value of $\zeta = 1/\sqrt{8} = 0.3535$.

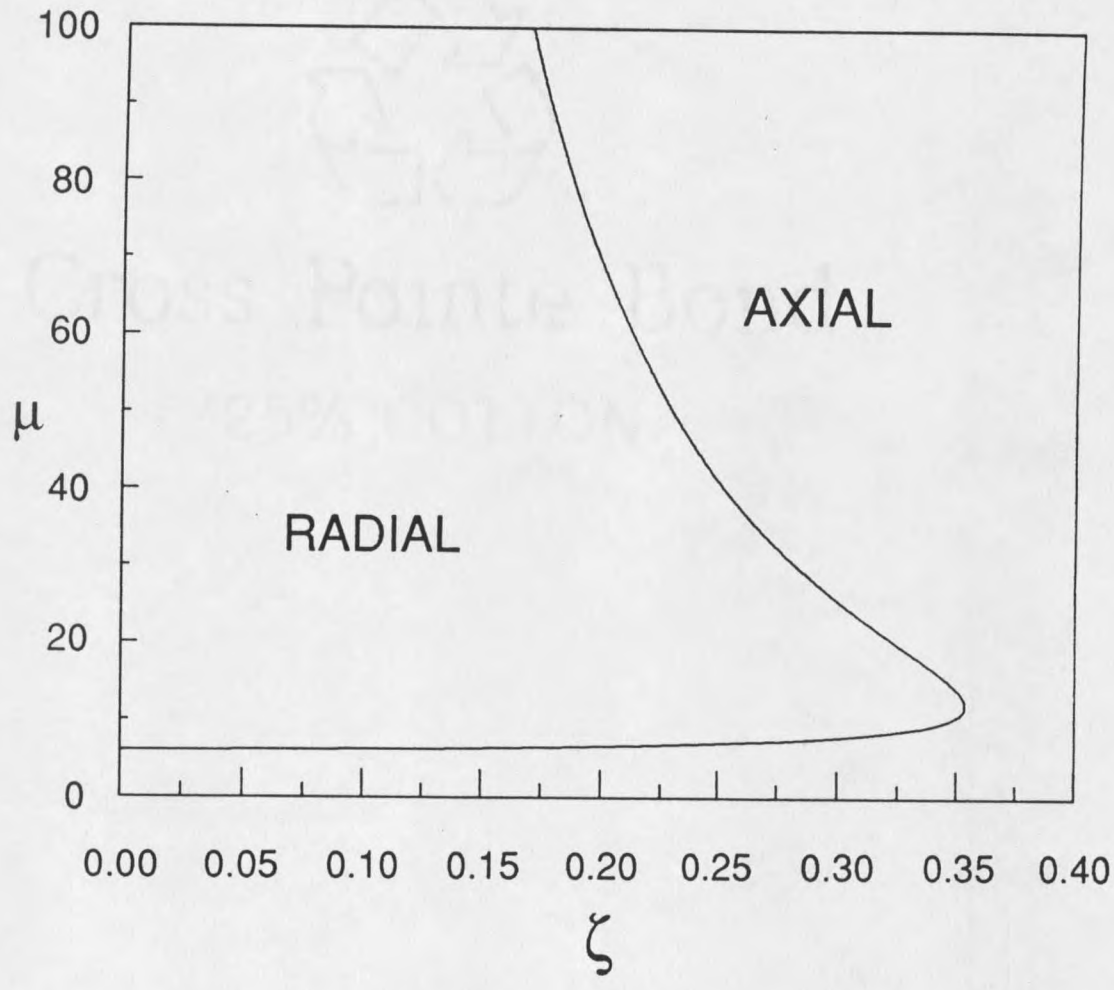

Figure 13. Phase diagram in uniform-field and uniform-order-parameter approximation, obtained from the model Eq. (105). The phase diagram is plotted as a function of the dimensionless anchoring strength parameter $\mu = RW_o/K_{11}$ and field parameter $\zeta = (E/W_o)\sqrt{\Delta\varepsilon K_{11}/4\pi}$.

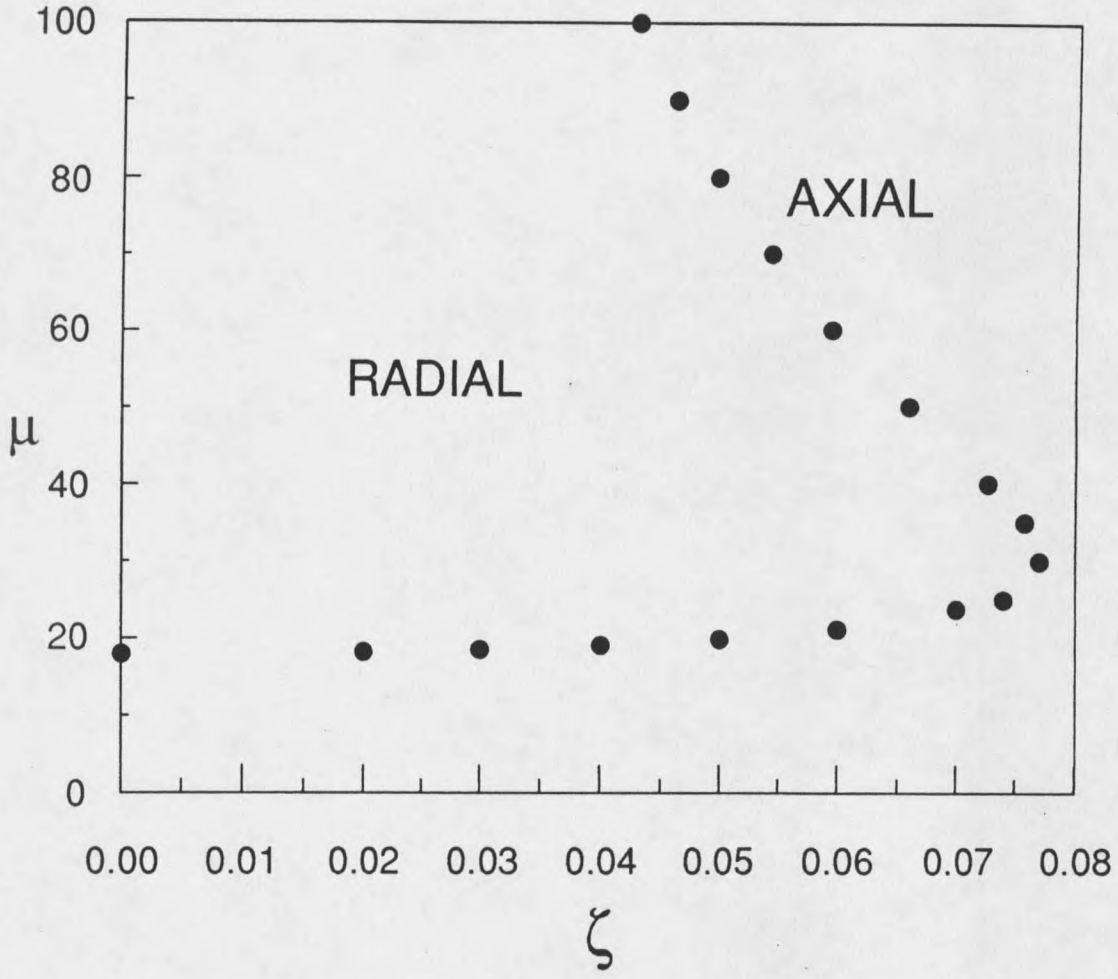

Figure 14. Phase diagram in the approximations of uniform field, uniform order parameter, no twist, and no saddle-splay, obtained numerically for $K_{33}/K_{11} = 1$, where $\mu = RW_o/K_{11}$ and $\zeta = (E/W_o)\sqrt{\Delta\varepsilon K_{11}/4\pi}$.

In addition, $\mu_+ \to \infty$ and $\mu_- \to 6$ when $\zeta \to 0$. The value $\mu_- \to 6$ is lower than the value of $\mu_- \sim 18$ seen by us (Figure 14) in our simulation of the uniform-field and uniform-order-parameter approximation. This implies that in zero field the "axial" phase can reduce its anchoring energy by bending the director near the surface, as shown in Figure 15:

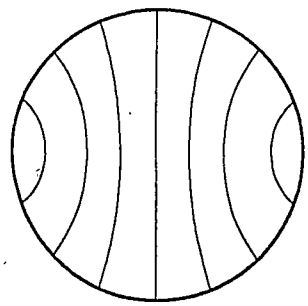

Figure 15. The axial phase is obtained by bending the directors near the surface of the perfectly uniform configuration.

Inhomogeneity of the Electric Field Within the Droplet

We shall discuss the nonuniformity of the E-field in magnitude and direction. In addition, we would like to understand how the elastic constants affect the nonuniformity.

E-Field Strength

Figure 16 shows the dependence of the field strength E on the radial coordinate ρ for varying anchoring strength parameter μ and field parameter ζ, where E is a function of electric polarization and dielectric anisotropy shown in Eq. (100). It is obtained for the stable phase at certain anchoring strength μ and field ζ in the phase diagram of Figure 24. That is, Figure 16 (a) is for the axial phase, Figure 16 (b) for axial phase, Figure 16 (c) for radial phase, and Figure 16 (d) for the axial phase. The conjugate gradient method for

direct minimization with a grid of 20×20 and the assumptions of constant order parameter, no twist, and no saddle-splay for $K_{33} = K_{11}$ have been adopted. We can see that the nonuniformity of the field strength increases from the center to the surface. In addition, the magnitude of the electric field increases at the axis and decreases near the equator. By comparing Figures 16 (b) and (c) we find that the higher field (ζ) parameter gives rise to larger magnitudes and stronger nonuniformity of the electric field inside the droplet. The stronger anchoring (μ) parameter also induces stronger E field and nonuniformity of E field, by comparing Figures 16 (a) and (b). We can understand the origin from the field parameter $\zeta = (ER/\mu)\sqrt{\Delta\varepsilon/4\pi K_{11}}$, where E is proportional to ζ and μ, and the components of the E field are position dependent. (Eqs. (58) and (59))

When the bend-to-splay ratio increases to 2, Figure 17 shows that the E-field nonuniformity becomes weaker for strong μ and ζ (Figures 17 (a) and (b)); that is, the position-dependent E-field strengths at five polar angles becomes closer. But there is no change for smaller value of $(\mu\times\zeta)$, indicated by the overlapping of solid ($K_{33} = K_{11}$) and open (K_{33}/K_{11}=2) symbols. (Figure 17 (c)) However, the influence of saddle-splay deformation on the nonuniformity of E field strength is in the opposite sense, as shown in Figure 18. That is, the nonuniformity of E field strength becomes stronger for larger values of $(\mu\times\zeta)$ (Figure 18 (a) and (b)). There is still no change for smaller value of $(\mu\times\zeta)$ (Figure 18 (c)).

E-Field Angle

In the same fashion we shall discuss the E-field angle nonuniformity and how the elastic constants affect the E-field angle. By using numerical methods mentioned above, we obtain the position dependence of the E-field angle between the axis and the field for various anchoring strength parameters μ and field parameters ζ. The E-field angles are

obtained by $\theta_E = \tan^{-1}(E_t/E_r)$, where E_t and E_r, respectively, are the tangential (theta) component and radial component of E field. (Eqs (58) and (59)) Figure 19, obtained for $K_{33} = K_{11}$, no twist, no saddle-splay, and constant order parameter, shows that the field departs from the axis direction, which is indicated by the polar angle θ, and the E-field angle increases from the center to surface where its variation is also a maximum.. Figures 19 (a), (b), and (c) show that the the E-field angle variation in the bulk (i.e. $\theta = 37.9°$ and $\theta = 56.8°$) is much larger than in the region near the axis (i.e. $\theta = 18.9°$) and the equator (i.e. $\theta = 75.8°$). By comparing Figures 19 (a) and (b) we find that the stronger field strength parameter ζ gives rise to larger angles of E field. The strength of the anchoring parameter μ does not affect the field angle as seen by comparing Figures 19 (b) and (c).

When the ratio K_{33}/K_{11} increases to 2, the E-field angle decreases at stronger ζ (Figure 20 (a)) and stronger μ (Figure 20 (c)) but increases at smaller ζ (Figure 20 (b)). The influence of the saddle-splay deformation on the E-field angle can be obtained by comparing the E-field angles obtained for the case without K_{24} and the case with K_{24}, as shown in Figures 21 (a), (b), and (c). In this point K_{24} also shows an opposite influence to that of K_{33}/K_{11}=2, that is, the E-field angle increases at stronger ζ (Figure 21 (a)) and stronger μ (Figure 21 (c)) but decreases at smaller ζ (Figure 21 (b)).

From the discussions of nonuniformity of the E-field strength and angle, we find that the nonuniformity of the E-field magnitude is greater for larger ζ and μ, but the nonuniformity of the E-field angle is only strong for stronger ζ. Generally speaking, for strong ζ and μ, increasing the bend-to-splay ratio decreases the nonuniformity of E-field strength and angle, while the inclusion of the saddle-splay deformation increases the nonuniformity.

Phase Diagrams

Stable configurations of the nematic droplet in an electric field in general result from the competition between bulk elastic forces and surface anchoring under specific conditions of temperature and external field. In this section we discuss the dependence of the stability of the radial and axial configurations on the anchoring strength, droplet radius, ratio of elastic constants, and the electric field strength in the universal phase diagrams where the phase boundary is plotted as a function of dimensionless parameters μ and ζ, measuring the relative anchoring strength and the relative external field strength, respectively. (Figure 22) The phase boundary is determined by comparing free energies of the radial and axial phases (Figure 23), and successive bracketing in ζ at constant μ, and bracketing in μ at constant ζ until the bracketing range is less than 2×10^{-3}. Every phase diagram discussed here is in the same format, that is, each phase boundary separates the stable phases of the radial on the left and the axial on the right.

Numerical Methods and Various Sizes of the Computational Grid

For $K_{33}/K_{11}=1$, with the assumptions of uniform order parameter, no twist, and no saddle-splay, the $\mu-\zeta$ phase diagrams shown in Figure 24 are obtained by using the conjugate gradient technique for direct minimization to find the phase boundaries for a sequence of sizes up to 40×40. Three phase boundaries in Figure 25 are obtained by using conjugate gradient technique in a 20×20 mesh for $K_{33}/K_{11}=1$, $K_{33}/K_{11}=2$, and $K_{33}=K_{11}=K_{24}$, respectively. Under the same assumptions, we also obtain the three phase boundaries in Figure 26 by solving the Euler-Lagrange equations with Newton's relaxation method and using a 100×100 mesh for $K_{33}/K_{11}=1$, $K_{33}/K_{11}=2$, and $K_{33}=K_{11}=K_{24}$, respectively. Comparing Figures 25 and 26, we find that the phase boundaries obtained by

the two numerical methods have same tendency, that is, the reentrant feature of the axial phase vanishes, and the boundary corresponding to $K_{33}/K_{11} = 2$ is left of the boundary corresponding to $K_{33}/K_{11} = 1$ at intermediate and large anchoring strength, and the curve of $K_{33} = K_{11} = K_{24}$ has a kink at weak anchoring strength.

For the reasons mentioned in the "Errors" section of Chapter 3, the finer computational grid may not always give more accurate results. Thus, in the calculation of nonuniform-field approach we shall use the results obtained by using a grid size of 20x20 for the direct minimization and the conjugate gradient technique in later sections due to convenience and simplicity of the calculation. It is really a compromise between (presumed) accuracy and computational speed.

Nonuniform- and Uniform-Field Approach

To test our code, we compare our uniform-field results with those obtained by Kralj *et al*[6]. Here we use the results found by solving the Euler-Lagrange equations by Newton's relaxation method under the assumptions of no twist and spatially constant S and E.

The phase diagrams in the uniform-field approximation shown in Figure 27 are in close agreement with those of Reference 6. Radial phases are stable at intermediate and larger anchoring strengths but weak external field strength. Axial phases are stable for any anchoring strength in a strong external field, but in weak fields only for weak anchoring. For very weak anchoring ($\mu \approx 18$ for the case of $K_{33}/K_{11} = 1$), the elastic forces stabilize the axial phase even in the absence of an electric field ($\zeta \to 0$). The phase diagrams have an important feature, reentrance of the axial phase, in that the phase induced by an increasing μ goes from axial to radial then back to axial again. That is, the transition field is maximum at an inversion point, where the radial-axial transition is reached. Either

increasing the bend-to-splay elastic constant ratio K_{33}/K_{11} or taking into account the saddle-splay contribution (K_{24}) causes the boundary to shift to the right, enlarging the radial phase region, since the axial phase involves significant bend distortion, while the radial phase has largely splay.

The phase diagram in Figure 25 was obtained by relaxing the uniform-field approximation, that is, by permitting $\bar{E}$ to vary in direction and magnitude in response to the direct field. It is substantially different from the phase diagrams obtained by the uniform-field approach. The region of stability of the radial phase grows, at the expense of the axial phase. The reentrant feature of the axial phase has vanished. We can understand this feature from the simplest calculation, i.e. the "perfect-phase" model. It had the origin in the part of the free energy difference ΔF proportional to volume (e.g., the third term of the r.h.s. of Eq. (104)). The director is in fact able to align more closely with the field than the uniform-field approximation would allow, and the field-dependent parts of F are more nearly equal in the two phases. Figure 23 shows a typical comparison of radial phase vs. axial phase free energies, in a scan at constant ζ. We cannot exclude the possibility that the curves cross a second time at large values of μ, so that the phase boundary eventually bends back toward the μ axis in the phase diagram. More likely, however, is that with strong anchoring and field the radial and axial patterns are very similar, differing only by the form of the director very near the equatorial plane. (Figures 28 (a) and (b)) In this case the field-dependent part of ΔF is proportional to R^2 rather than R^3. Thus the reentrant feature of the axial is lost and the radial phase is still favored for strong field strength parameter ζ.

The nonuniform-field approach shows a much different influence of the elastic constant ratio K_{33}/K_{11} and K_{24}, on the phase diagrams. (Figure 25) This can be understood from the earlier discussions concerning the influence of $K_{33}/K_{11} = 2$ and K_{24} on the nonuniformity of E-field. That is, increasing bend-to-splay ratio decreases the

nonuniformity of the E-field for strong anchoring μ and field ζ. In addition, the inclusion of saddle-splay K_{24} increases the field nonuniformity for strong μ and ζ but causes no change for small μ or ζ. Thus, in Figures 29 (a) and (b), for $K_{33}/K_{11} = 2$ with strong anchoring (i.e. $\mu = 60$) and field (i.e. 0.2 for the stable radial phase and 0.4 for stable axial phase) the radial phase differs from the axial phase not only in the region near the equator but also in the bulk. In this case the field-dependent part of total free energy is more likely proportional to R^3 rather than R^2. Therefore, the phase boundary of $K_{33}/K_{11} = 2$ shifts to the left. For $K_{33} = K_{11} = K_{24}$, increasing nonuniformity of the E-field at strong anchoring and field will cause the phase boundary to shift slightly to the right of the $K_{33}/K_{11} = 1$ curve but there is no change due to field nonuniformity for weak anchoring or field and the phase boundary is the same as in the case of the uniform-field approximation.

Various Contributions of Elastic Deformations

In this section we shall discuss the influence of the elastic deformations on the phase transition by introducing the dimensionless parameters related to elastic forces, i.e. the elastic constant ratios K_{33}/K_{11}, K_{22}/K_{11}, and K_{24}/K_{11}.

Bend Deformation

We have found that the bend contribution has significant influence on the location of the phase boundary. (Figure 30 and 31) Figure 31 is obtained by adding a twist contribution to the calculation of Figure 30. Both figures show that the effect of increasing bend-to-splay ratio is opposite to that which we obtain in the uniform-field approach (Figure 27) for anchoring parameter $\mu > 20$. That is, the higher bend-to-splay

ratio causes the boundary to shift to the left and enlarge the axial phase region for the reason we have discussed in the previous section.

Twist Deformation

To see the influence of a twist deformation on phase transition, Figure 32 (in the assumption of uniform order parameter and no saddle-splay,) compares the case with twist to the case without twist for two ratios: $K_{33}/K_{11} = 1$ and $K_{33}/K_{11} = 2$. The boundary with a twist contribution is not much different from the boundary without a twist contribution, but the boundaries with higher bend-to-splay ratios, i.e. $K_{33}/K_{11} = 2$ and $K_{22} = K_{33}/2 = K_{11}$, are much different from the boundaries with lower ratios, i.e. $K_{33}/K_{11} = 1$ and $K_{22} = K_{33} = K_{11}$. Thus the twist deformation has less influence on the phase diagram than the bend does. However, twist does affect the phase transition when the twist phase is stable, that is, if the splay elastic constant is large enough ($K_{22}/0.5 = K_{11} = K_{33}/0.5 = K_{24}$ in our calculation). Twist configurations will be discussed together with the saddle-splay deformation next.

Saddle-Splay Deformation

Figure 33 shows the strong influence of the saddle-splay constant on the phase transition. The phase diagrams under the assumptions of uniform order parameter and no twist, are obtained for the case without K_{24} and the cases with two ratios of K_{24}/K_{11} (i.e. $K_{24}/K_{11} = 1$ and $K_{24}/K_{11} = 2$). The phase boundaries indicate that saddle-splay stabilizes the radial phase for weak anchoring. Furthermore, it is impossible to find a stable axial phase for very weak anchoring even for a very strong external field when the saddle-to-

splay ratio increases beyond a threshold value, which is estimated as 2. (Figures 34 (a) and (b)) For strong anchoring the inclusion of the saddle-splay contribution does not affect the phase boundary much. (Figures 33) But we need to emphasize again that for anchoring above intermediate strength the phase boundary has lost its reentrant feature, while the reentrance of the axial phase is the main feature of the uniform-field approximation. Our result here is in agreement with the experimental result of Figure 6 in Reference 5. Their transition field E_c and nematic droplet diameter d are related to our dimensionless field strength parameter $\zeta = d/\xi = (E/W_o)\sqrt{\Delta\varepsilon K_{11}/4\pi}$ and anchoring strength parameter $\mu = R/d = RW_o/K_{11}$, respectively.

Figure 35 shows the phase boundaries with different combinations of elastic constant ratios. Comparing the phase boundary for $K_{33} = K_{11} = K_{24}$ to that for $K_{33} = K_{11}$ without K_{24} we can see that including K_{24} stabilizes the radial phase for weak anchoring where the boundary has a kink. The phase boundary then shifts to the left and the kink does not change much as the bend-to-splay ratio increases to 2, i.e. $K_{33}/2 = K_{11} = K_{24}$. If the ratio of K_{24}/K_{11} also increases to 2, i.e. $K_{33}/2 = K_{11} = K_{24}/2$, then only the kink expands as a long tail.

In Figure 36 three phase boundaries are obtained for $K_{22} = K_{11} = K_{33} = K_{24}$, $K_{22}/0.5 = K_{11} = K_{33} = K_{24}$, and $K_{22}/0.5 = K_{11} = K_{33}/0.5 = K_{24}$. The phase boundary for $K_{22}/0.5 = K_{11} = K_{33}/0.5 = K_{24}$, containing the larger splay elastic constant, shows stability of the phase boundary for strong anchoring, that is, the phase boundary does not fluctuate and there is little fluctuation in the total free energy of the radial or axial phase. The instabilities of the other two boundaries were shown in the numerical calculations for strong anchoring. Our results here are similar to those reported by Williams[20]. For strong tangential anchoring and uniform order parameter, he has demonstrated theoretically the existence of a twisted bipolar phase in nematic droplets for a splay elastic constant that is

large compared to the sum of the twist and bend constants, that is, $K_{11} \geq K_{22} + 0.431K_{33}$. The phase containing more splay cannot have stable twist configurations.

Figures 37 (a)-(f) are the projections of director configurations on the local $\theta - \varphi$ planes as the electric field is applied in the direction out of the paper. They are obtained under the assumptions of uniform order parameter for $K_{22} / 0.5 = K_{11} = K_{33} / 0.5 = K_{24}$ at variable strengths of anchoring μ and field ζ. There are larger twist angles on the axis and the equator than in the bulk. Increasing ζ reduces the director twist angles near the equator as seen by comparing Figures 37 (a), (b), and (c). Therefore a mirror symmetry appears on the equatorial plane for the large field, while there is still a twist configuration when the droplet is viewed along the field. Our results here also can be found in Reference 8. But the variation of μ does not affect twist angles, as seen by comparing Figures 37 (d), (e), and (f).

Although we have seen many phase diagrams obtained by various combinations of elastic constants, to conclude which phase boundary is appropriate for a certain kind of nematic liquid crystal we need specific experimental information about the elastic constant ratios K_{22}/K_{11} [49-51], K_{33}/K_{11} [32, 34, 49-51], and K_{24}/K_{11} [27,35].

Position-Dependent Order Parameter

When the order parameter S is allowed to vary spatially we must consider the temperature dependence of the elastic constants via S:

$$K \propto S^2(T) + cS^3(T) + \ldots\ldots \text{ with } c << 1, \tag{107}$$

which follows from the Landau-de Gennes free energy density, expressed in terms of the order parameter tensor $Q_{\alpha\beta}(\vec{r})$ (Eq. (12)) and its derivatives. For simplicity we have

adopted the scalar order parameter dependence of the elastic constants only up to the order S^2: $K_{11} = k_{11}S^2$, $K_{22} = k_{22}S^2$, $K_{33} = k_{33}S^2$, and $K_{24} = k_{24}S^2$ for splay K_{11}, twist K_{22}, bend K_{33}, and saddle-splay K_{24} elastic constants. Up to order S^2, Landau-de Gennes theory predicts $K_{11} = K_{33}$, whereas the inclusion of the higher order terms in S will generally make $K_{11} \neq K_{33}$. For instance, $K_{11} \neq K_{33}$ if a term of the form $Q_{\alpha\beta}(\bar{r})\left[\partial_\alpha Q_{\gamma\delta}(\bar{r})\right]\left[\partial_\beta Q_{\gamma\delta}(\bar{r})\right]$ is introduced into the Landau-de Gennes expression (Eq. (26)) because this term gives rise to

$$2S^3\left\{\left[\bar{\nabla}\cdot\hat{n}(\bar{r})\right]^2+\left[\hat{n}(\bar{r})\cdot\bar{\nabla}\times\hat{n}(\bar{r})\right]^2+2\left[\hat{n}(\bar{r})\times\bar{\nabla}\times\hat{n}(\bar{r})\right]^2\right\} \qquad (108)$$

However, in Figures 38 and 39 we see that the influence of the coupling between director $\hat{n}$ and order parameter S on the phase diagram is not great. Thus we do not take into account the higher-order dependence on S. We do, however, allow K_{11} and K_{33} to be unequal (Figure (39)), since experiments[32, 34, 49] indicate that this is the case. When the order parameter is allowed to vary as well as the director field, the region of stability of the radial phase grows at the expense of the axial phase in strong field and anchoring strength for $K_{33} = K_{11}$ without twist and saddle-splay. (Figure (38)) But for the case including twist and saddle-splay, for the large splay constant, (i.e. $K_{22}/K_{11} = 0.5$ and $K_{33}/K_{11} = 0.5$) (Figure (39)), the phase boundary shifts to the left and is to the left of the boundary obtained in the uniform-order-parameter assumption. Both phase boundaries in Figures 39 look more like the phase boundary obtained for $K_{33} = K_{11} = K_{24}$ without twist in the uniform-field and uniform-order-parameter aproximation, shown in Figure 27. The scale is different because the bend-to-splay ratio used in Figure 39 is smaller and the director can align with the field more closely than the uniform-field approximation would allow. These results also can be understood by noting that the E-field nonuniformity is affected by different elastic deformations.

For $K_{33} = K_{11} = K_{24}$ without twist, Figures 40 (a)-(f) and 41 (a)-(e) show that near the equator there is a region where most of the directors are not parallel to the E-field direction (z-axis). The thickness L of the region decreases as ζ increases in Figures 40 (a)-(f). L also decreases as μ increases in Figures 41 (a)-(e). Thus the thickness of the region can be estimated as the function of μ and ζ:

$$L \approx R/\zeta\mu = (1/E)\sqrt{4\pi K_{11}/\Delta\varepsilon}, \tag{109}$$

which is also mentioned in reference 5. In these Figures, the length of the bar (director) is proportional to the value of order parameter. Thus the order parameter increases in the center of the droplet as ζ and μ increases. We also can see this effect in Figures 42 (a)-(d), which shows the position-dependent order parameter $S(\rho,\theta)$ for increasing ζ at two chosen anchoring strengths, $\mu = 40$ and $\mu = 100$, in the radial phase. The equilibrium value of the order parameter in the undisturbed bulk is $S_o \approx 0.36$, which is obtained from Eq. (74)

$$S_o = \frac{b + \sqrt{b^2 - 4ac\left(T - T^*\right)}}{2c}, \tag{110}$$

with $a = 1.3\times10^6\ \mathrm{erg/(cm^3K)}$, $b = 1.836\times10^7\ \mathrm{erg/cm^3}$, and $c = 4.05\times10^7\ \mathrm{erg/cm^3}$. The order parameter at the center increases as the field strength increases, i.e. $\zeta = 0.01 \rightarrow \zeta = 0.1 \rightarrow \zeta = 0.3 \rightarrow \zeta = 0.5$. In particular, the order parameter at the center jumps up suddenly as the field parameter ζ increases from 0.01 to 0.1. This implies that the transition induced by the electric field may be discontinuous. In addition, the minimum of the order parameter on the equator seems to move toward the surface with increasing ζ. As the field increases, the axial phase eventually becomes stable. Comparing Figure 41 (a) and (b) with Figure 41 (c) and (d), we find that the order parameter on the surface

generally increases as the transition from radial phase to axial phase takes place, and is larger than in the bulk except on the equator, i.e. $\theta = 90°$. Therefore this tendency seems to tell us that the defect of the radial phase in the center may be disappearing as the field strength increases, and a defect ring may appear on the equatorial plane, moving out toward the surface as the field keeps increasing. A similar description can also be found in Reference 5, which describes experimental observations of micron-sized droplets.

The Defect in the Tangential Anchoring

This section is a continuation of our study of the position-dependent order parameter $S(\vec{r})$. We enforced the tangential anchoring on the droplet surface by using the negative value of anchoring strength ($W_o < 0$) in the calculation of the axial phase. Consequently defect regions are created, where the elastic energy is reduced by the suppression of the order parameter $S(\vec{r})$. We show a typical pattern in Figure 43 (a), where the director length is proportional to the order parameter S. Stronger surface anchoring, smaller droplet radius, and higher temperature difference $\Delta T\left(= T - T_c^*\right)$ induce a larger region of the defect, indicated in Figures 43(a) and (b), Figures 43(a) and (c), and Figures 43 (c) and (d), respectively. However, increasing field strength reduces the size of the defect region, shown in Figures 43 (b), (e), and (f).

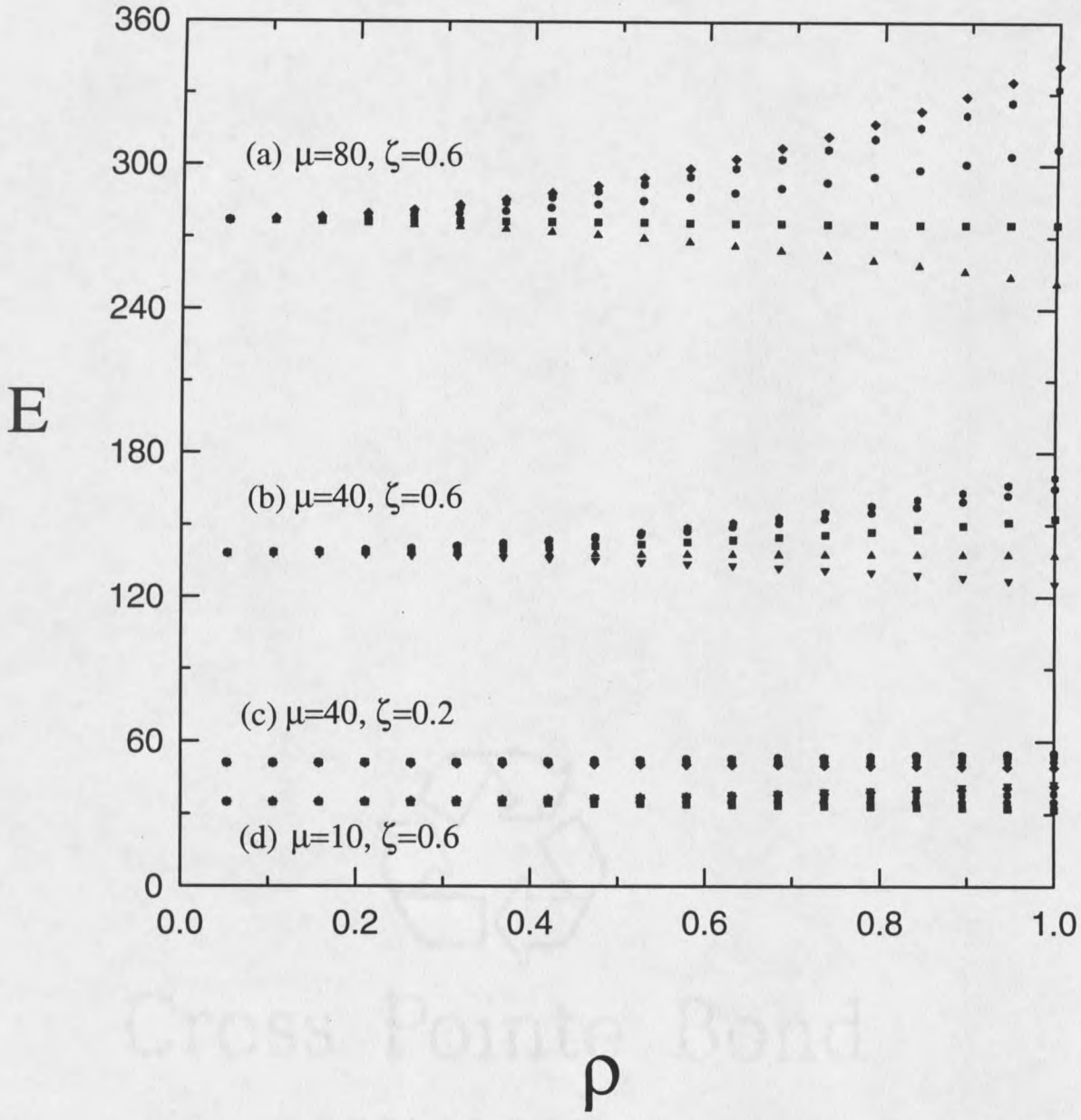

Figure 16. The dependence of the field strength E on the radial coordinate ρ for $K_{33}/K_{11} = 1$ at (a) $\mu = 80$, $\zeta = 0.6$ (b) $\mu = 40$, $\zeta = 0.6$, (c) $\mu = 40$, $\zeta = 0.2$, and (d) $\mu = 10$, $\zeta = 0.6$. They are obtained with the assumptions of fixed S, no-twist, and no saddle-splay. The five data lines in each branch are obtained at five chosen positions: $\theta = 0^\circ$, $\theta = 18.9^\circ$, $\theta = 37.9^\circ$, $\theta = 56.8^\circ$, $\theta = 75.8^\circ$, which descend from the top.

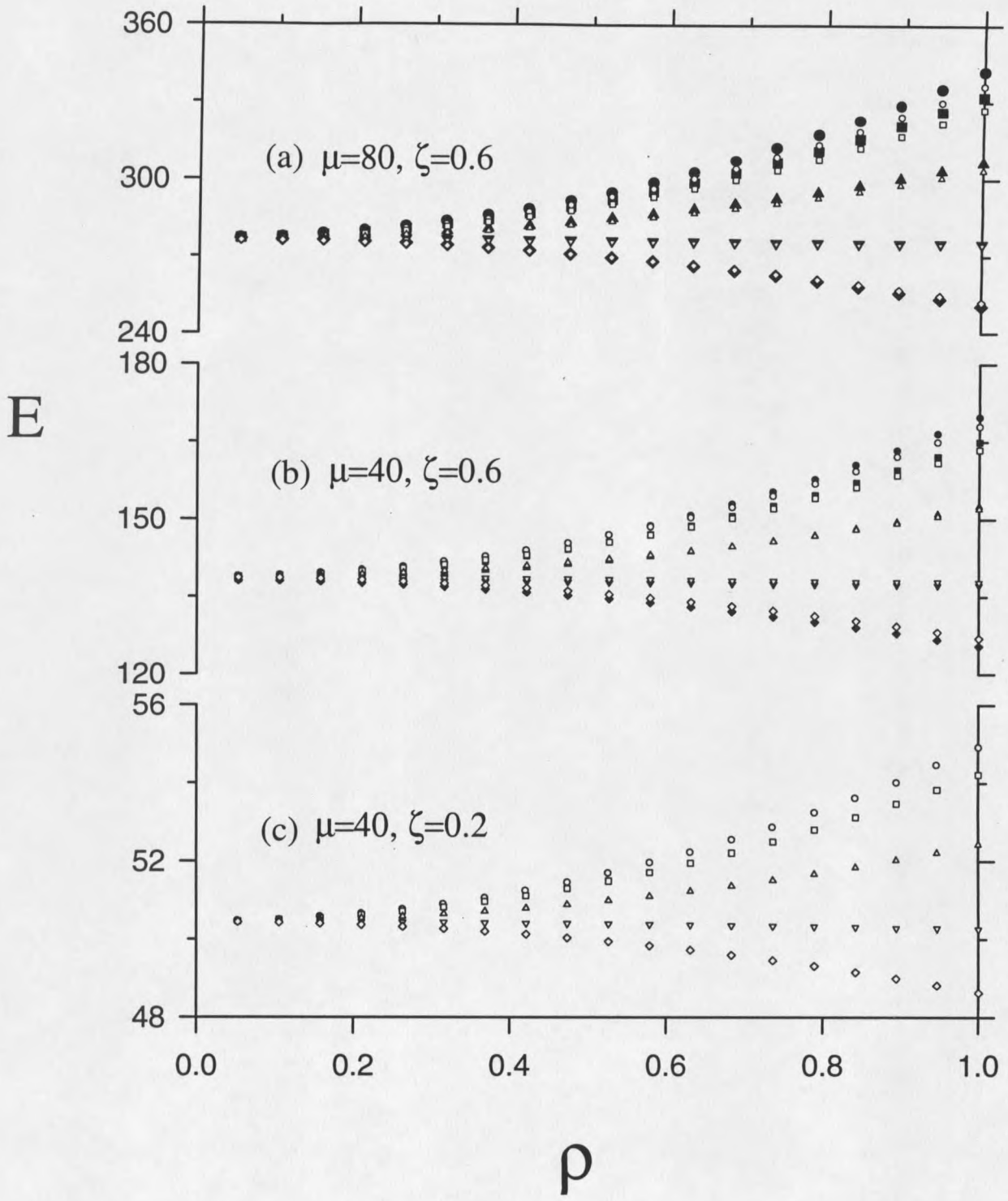

Figure 17. Comparison of the nonuniformity of E-field strength obtained for $K_{33}/K_{11} = 1$ and $K_{33}/K_{11} = 2$ at (a) $\mu = 80$, $\zeta = 0.6$ (b) $\mu = 40$, $\zeta = 0.6$, and (c) $\mu = 40$, $\zeta = 0.2$. The assumptions of fixed S, no K_{22}, and no K_{24} have been used. The solid and open symbols represent $K_{33}/K_{11} = 1$ and $K_{33}/K_{11} = 2$, respectively.

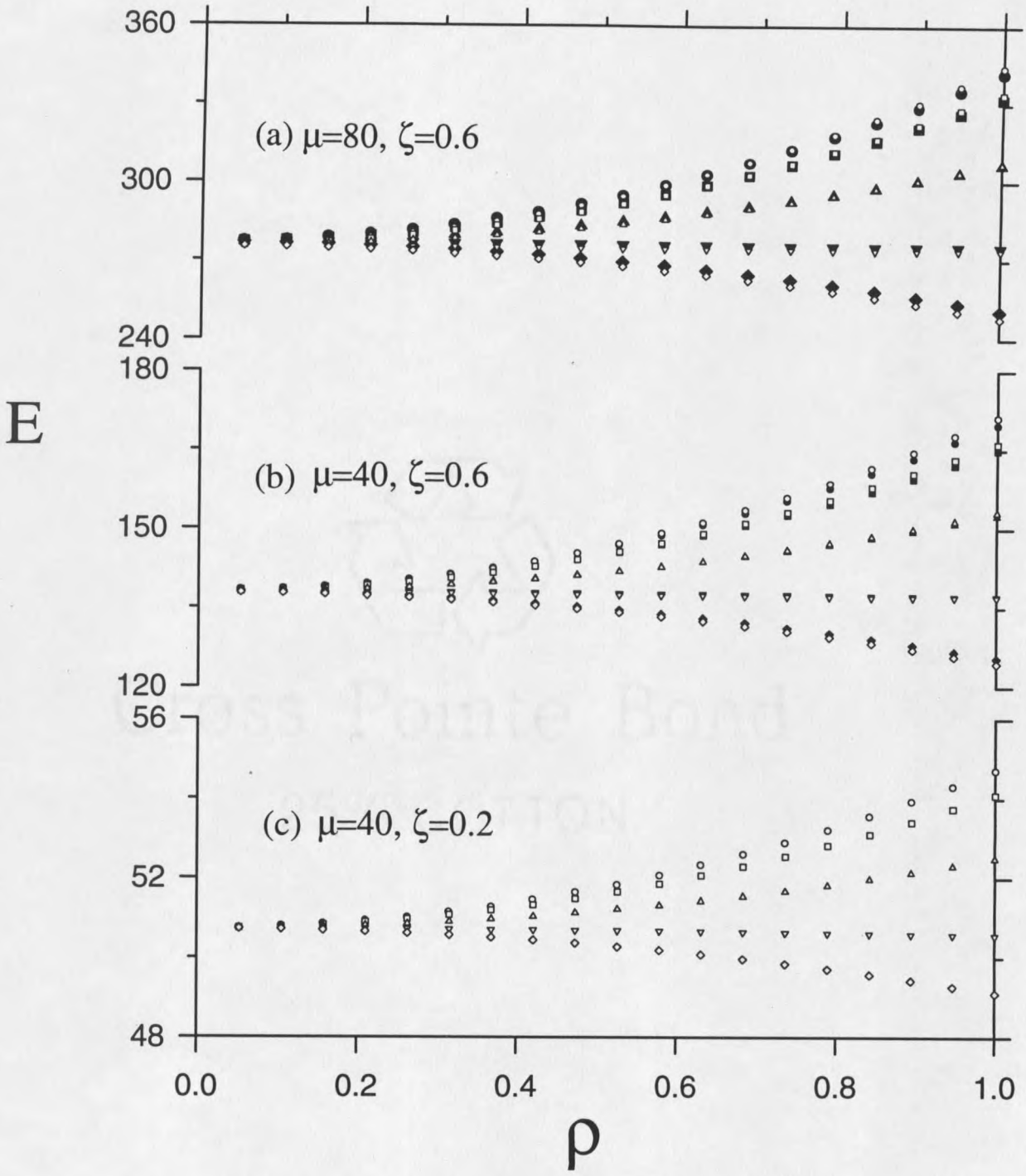

Figure 18. Comparison of the nonuniformity of E-field strength obtained for $K_{33} = K_{11}$ without K_{24} and $K_{33} = K_{11} = K_{24}$ at (a) $\mu = 80$, $\zeta = 0.6$ (b) $\mu = 40$, $\zeta = 0.6$, and (c) $\mu = 40$, $\zeta = 0.2$. The assumptions of fixed S and no K_{22} have been used. The solid and open symbols represent the case without K_{24} and the case with K_{24}, respectively.

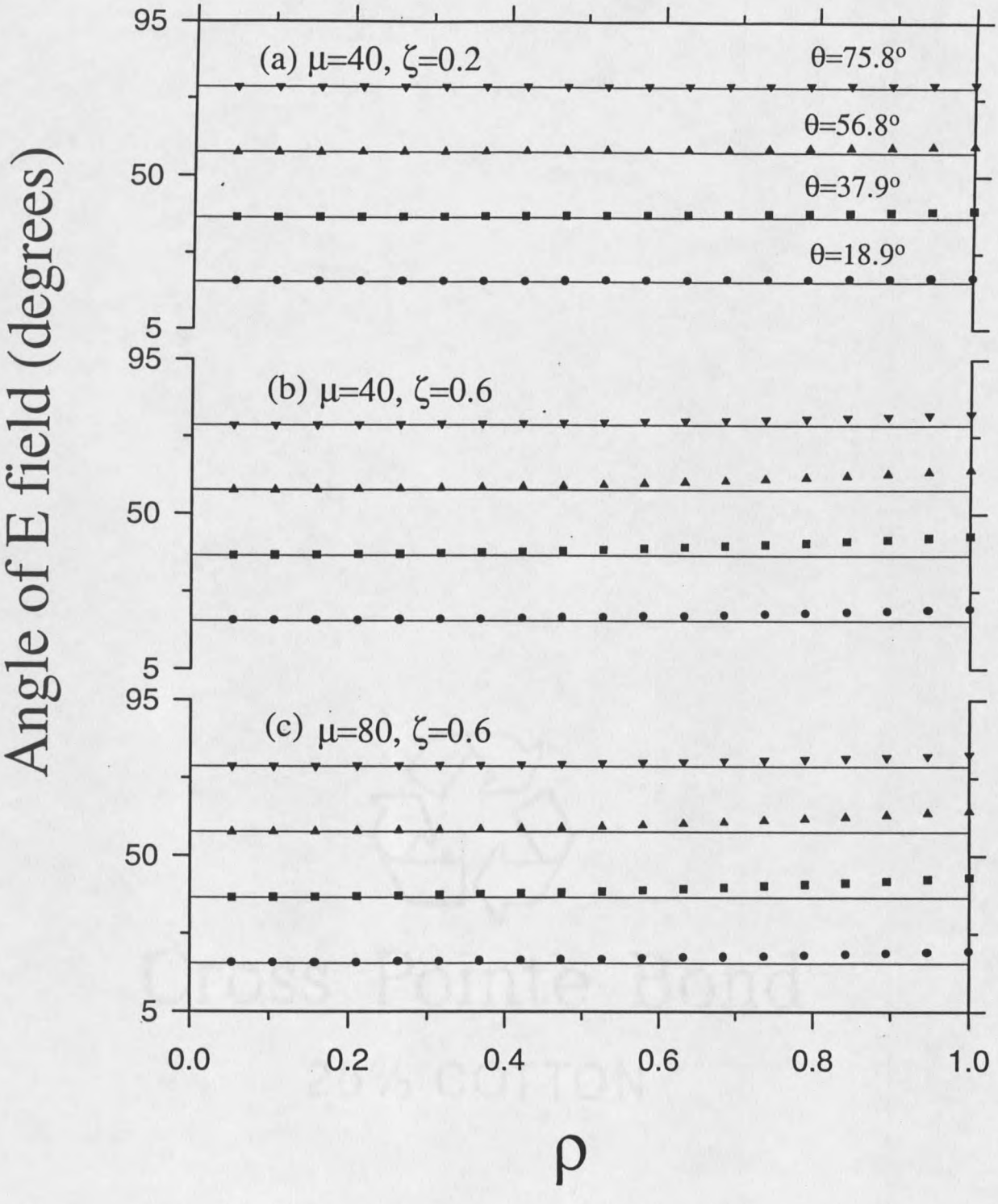

Figure 19. The position dependence of the E-field angle between the axis and the field is obtained for $K_{33} = K_{11}$ in the assumptions of no K_{22}, no K_{24}, and fixed S at (a) $\mu = 40$, $\zeta = 0.2$, (b) $\mu = 40$, $\zeta = 0.6$, and (c) $\mu = 80$, $\zeta = 0.6$. Each figure shows that the E-field angle departs from the axis at the four positions: $\theta = 18.9^{\circ}$, $\theta = 37.9^{\circ}$, $\theta = 56.8^{\circ}$, $\theta = 75.8^{\circ}$.

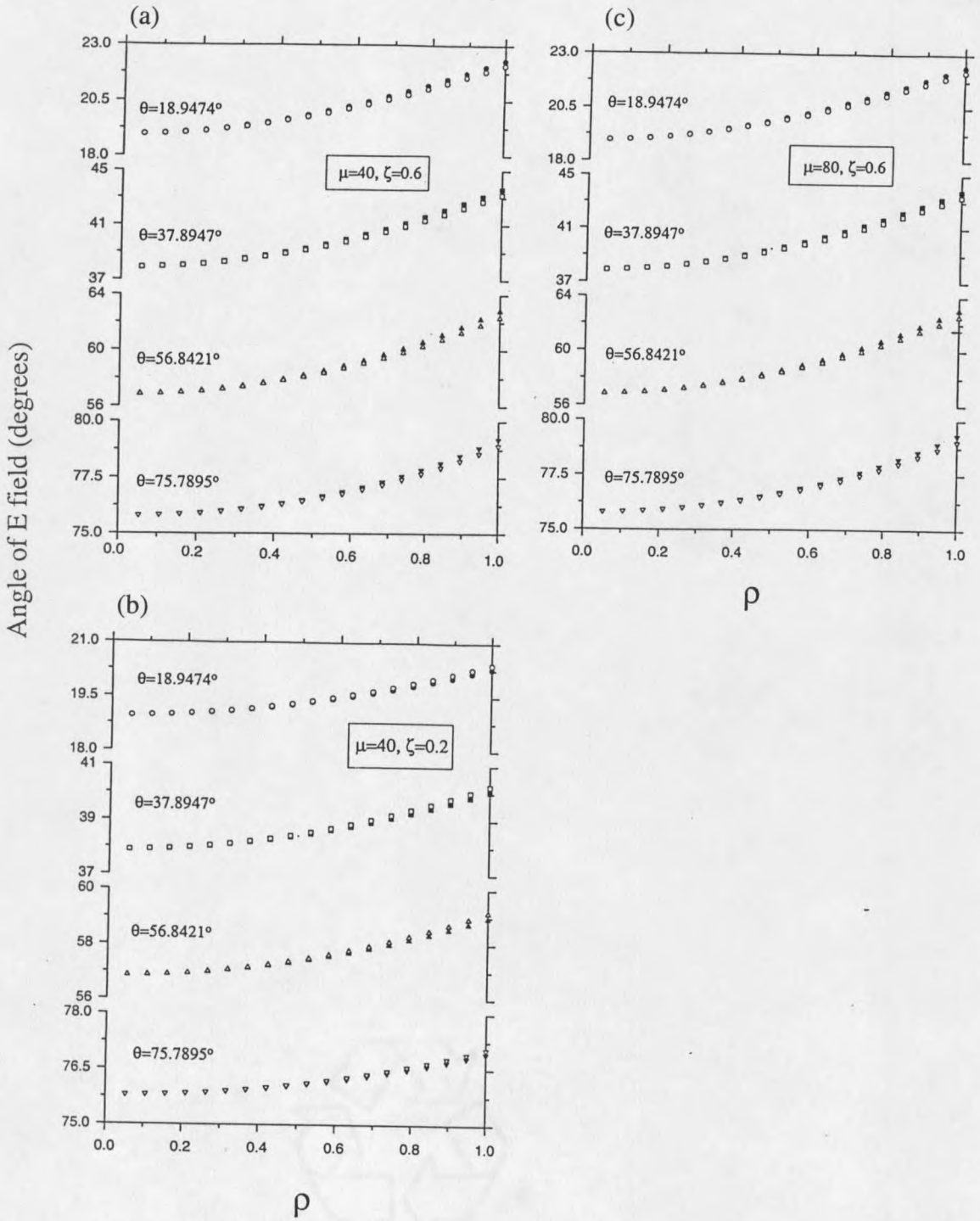

Figure 20. Comparison of E-field angles obtained for $K_{33}/K_{11} = 1$ and $K_{33}/K_{11} = 2$ at (a) $\mu = 40$, $\zeta = 0.6$, (b) $\mu = 40$, $\zeta = 0.2$, and (c) $\mu = 80$, $\zeta = 0.6$. The E-field angles are shown at four chosen positions: $\theta \cong 18.9^{\circ}$, $\theta \cong 37.9^{\circ}$, $\theta \cong 56.8^{\circ}$, $\theta \cong 75.8^{\circ}$. The assumptions of fixed S, no twist, and no saddle-splay have been used. The solid and open symbols represent $K_{33}/K_{11} = 1$ and $K_{33}/K_{11} = 2$, respectively.

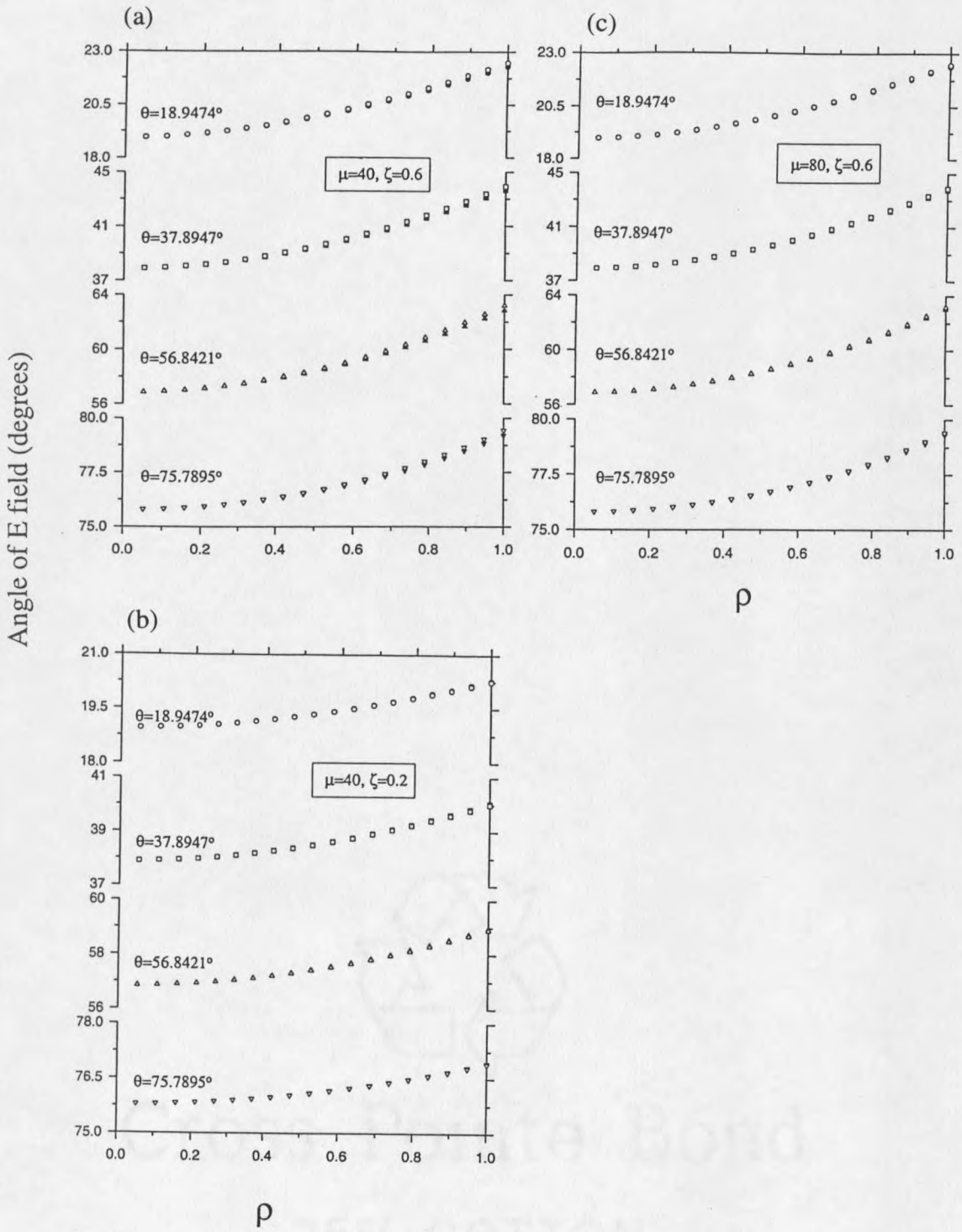

Figure 21. Comparison of E-field angles obtained for $K_{33} = K_{11}$ without K_{24} and $K_{33} = K_{11} = K_{24}$ at (a) $\mu = 40$, $\zeta = 0.6$, (b) $\mu = 40$, $\zeta = 0.2$, and (c) $\mu = 80$, $\zeta = 0.6$. The E-field angles are shown at four chosen positions: $\theta \cong 18.9^{\circ}$, $\theta \cong 37.9^{\circ}$, $\theta \cong 56.8^{\circ}$, $\theta \cong 75.8^{\circ}$. The assumptions of fixed S and no twist have been used. The solid and open symbols represent the case without K_{24} and the case with K_{24}, respectively.

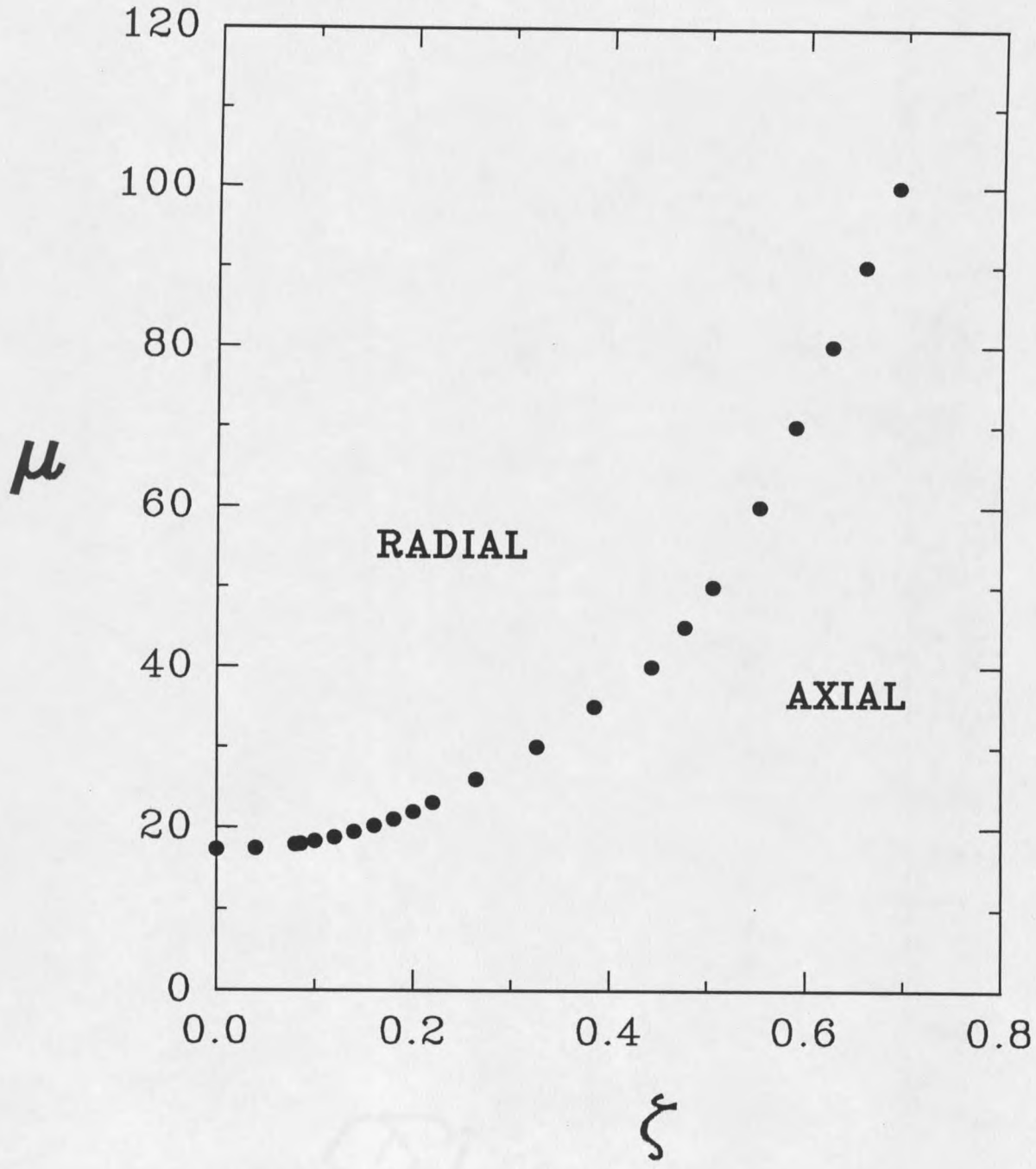

Figure 22. Phase diagram including effects of E-field nonuniformity in the assumptions of uniform order parameter, no twist, and no saddle-splay, obtained by solving the Euler-Lagrange equations with Newton's relaxation method and using a 100×100 mesh for $K_{33}/K_{11} = 1$. The stable phases indicated by the "RADIAL" and "AXIAL" are separated by the phase boundary, i.e. the dots. $\mu = RW_o/K_{11}$ and $\zeta = (E/W_o)\sqrt{\Delta\varepsilon K_{11}/4\pi}$.

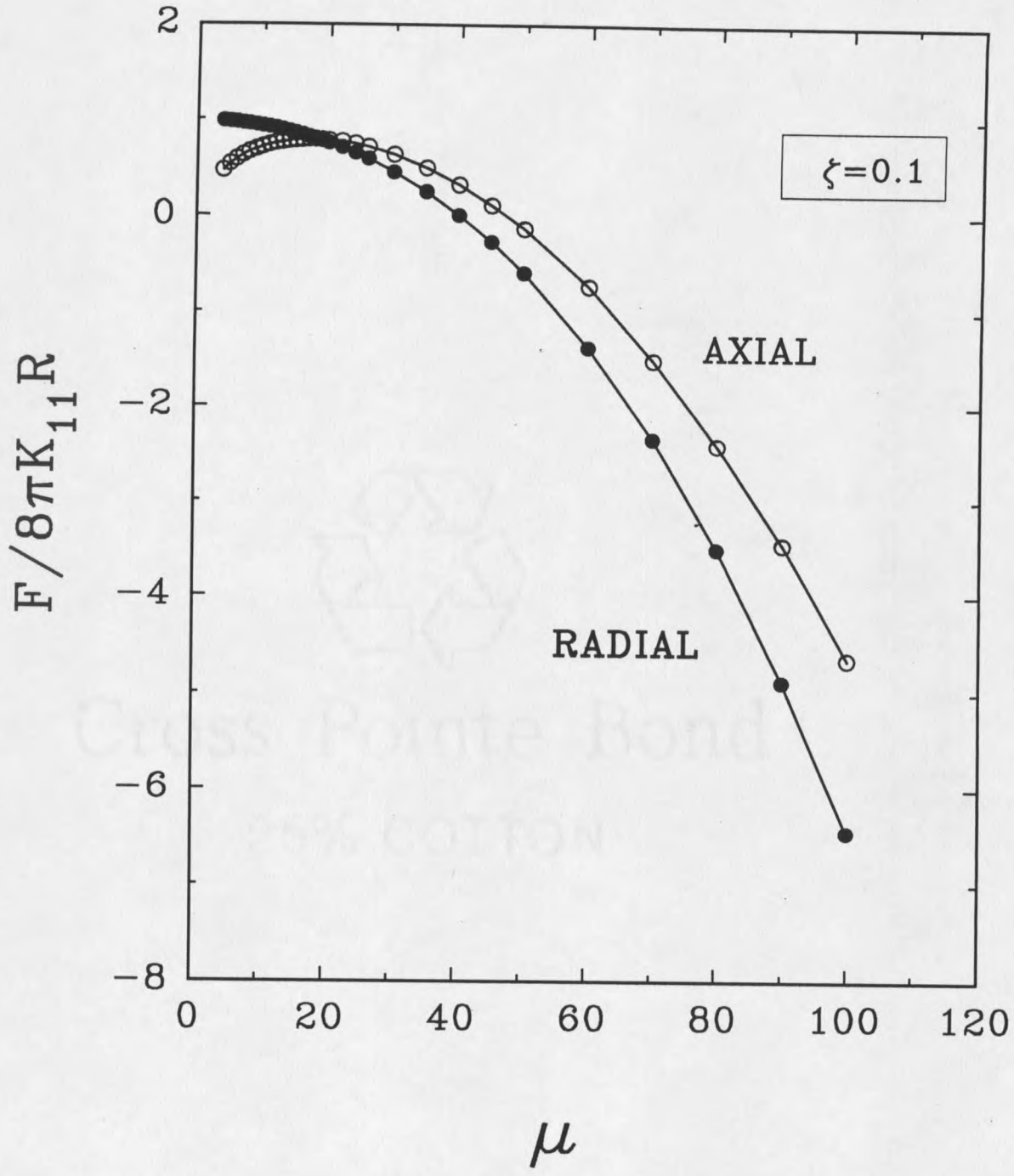

Figure 23. Axial vs. radial total free energies, in a scan of μ at constant ζ.

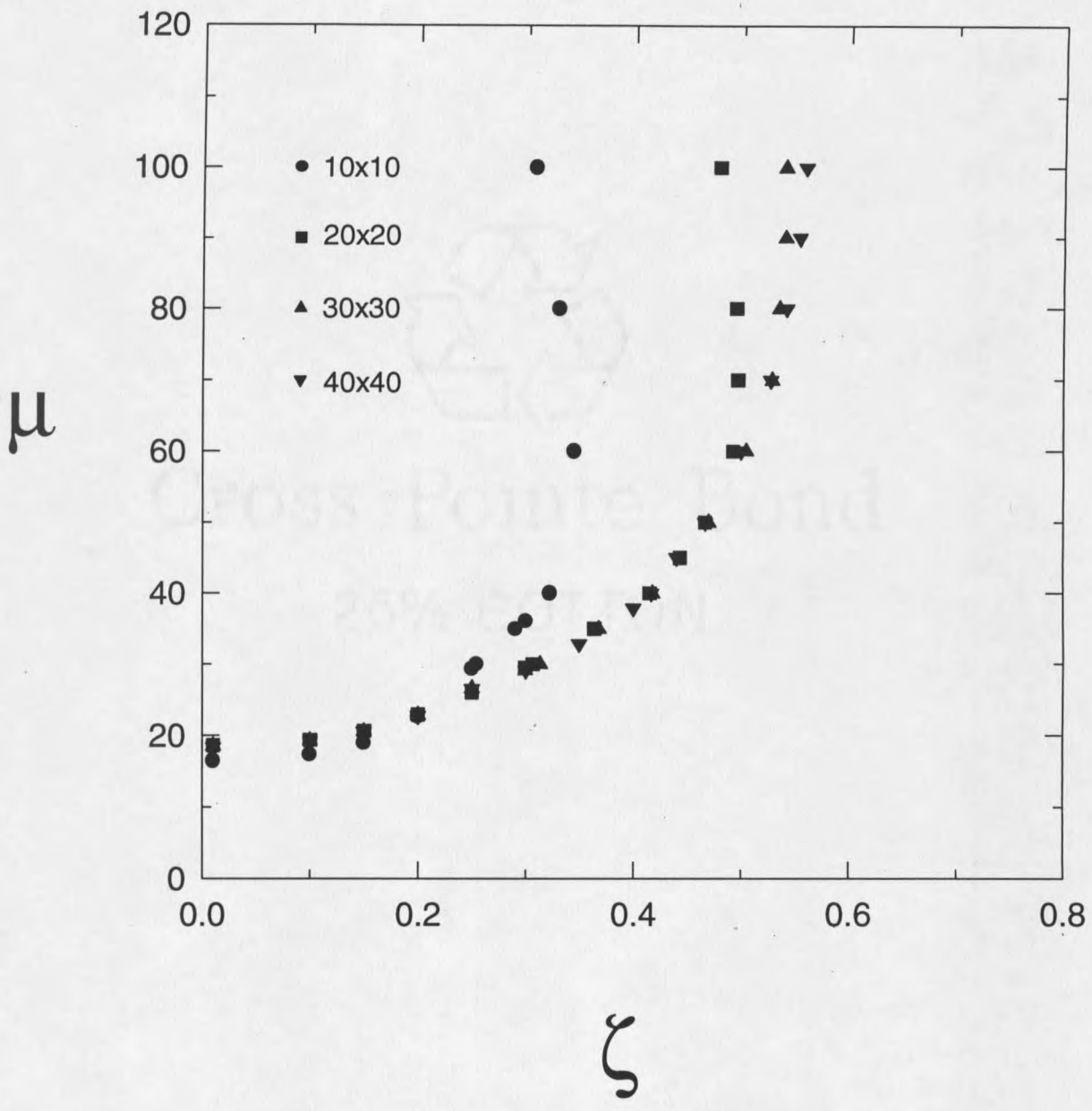

Figure 24. Phase diagrams in the assumptions of uniform order parameter, no twist, and no saddle-splay, obtained by using conjugate gradient technique for direct minimization for $K_{33}/K_{11} = 1$. The phase boundaries obtained by using the grid size of 10×10, 20×20, 30×30, and 40×40 are shown. Each phase boundary separates the stable phases of the radial on the left and the axial on the right

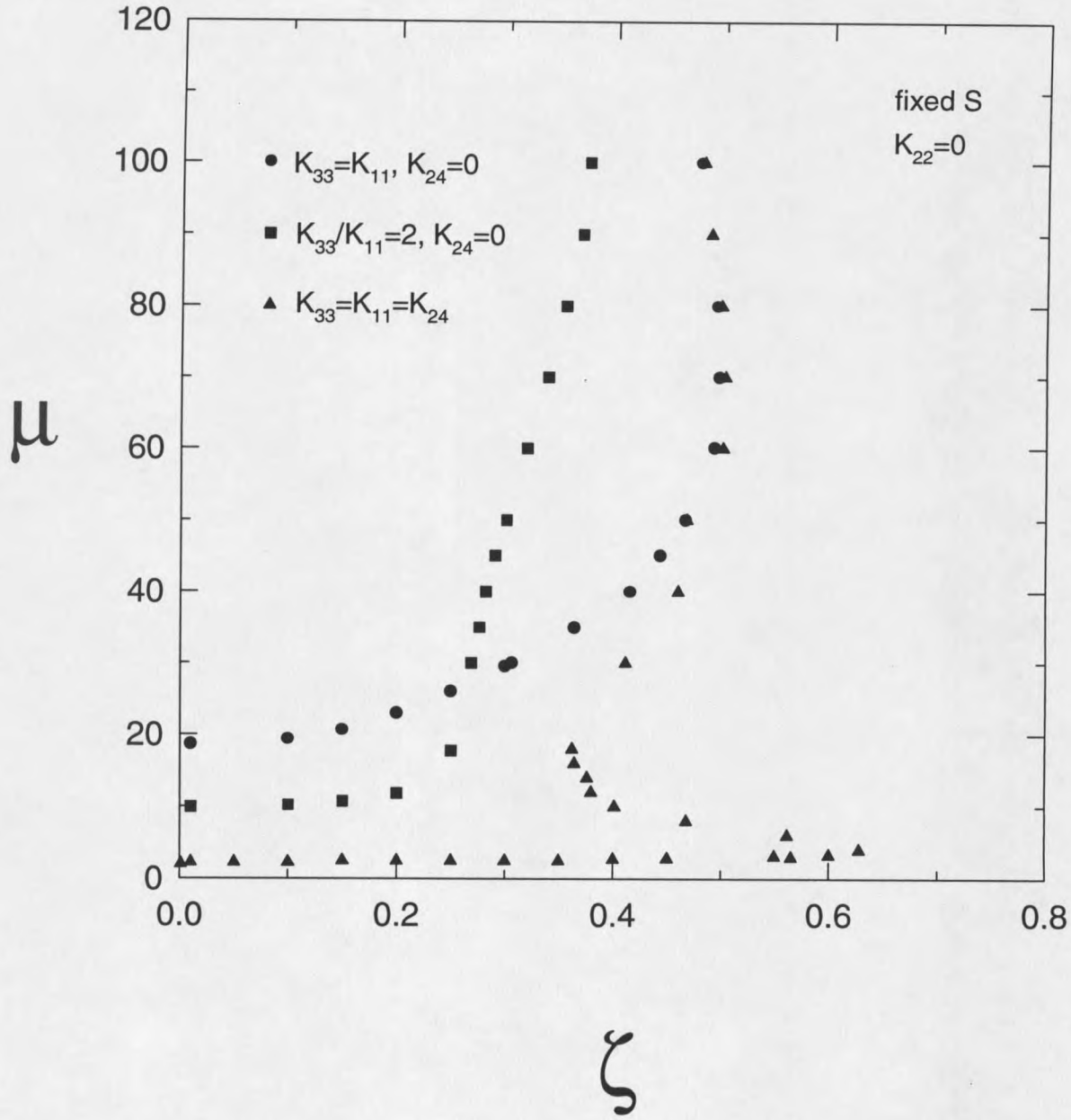

Figure 25. Phase diagrams in the assumptions of uniform order parameter and no twist, obtained by using a 20×20 mesh and conjugate gradient technique for direct minimization. Transition boundaries for $K_{33}/K_{11} = 1$, $K_{33}/K_{11} = 2$, and $K_{33} = K_{11} = K_{24}$ are shown. Each phase boundary separates the stable phases of the radial on the left and the axial on the right.

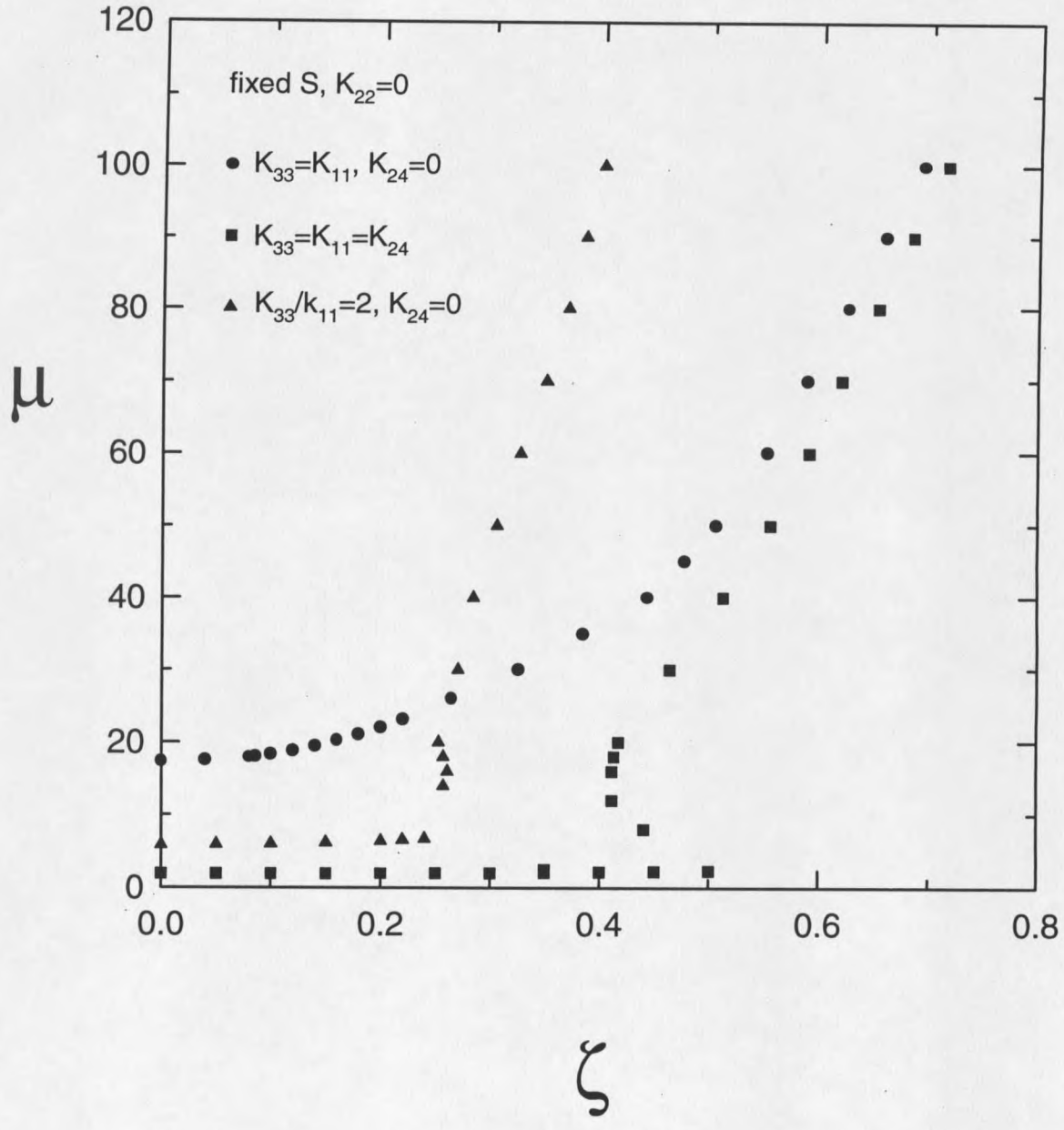

Figure 26. Phase diagrams in the assumptions of uniform order parameter and no twist, obtained numerically by solving the Euler-Lagrange equations and using a 100×100 mesh. Transition boundaries for $K_{33}/K_{11} = 1$, $K_{33}/K_{11} = 2$, and $K_{33} = K_{11} = K_{24}$ are shown. Each phase boundary separates the stable phases of the radial on the left and the axial on the right.

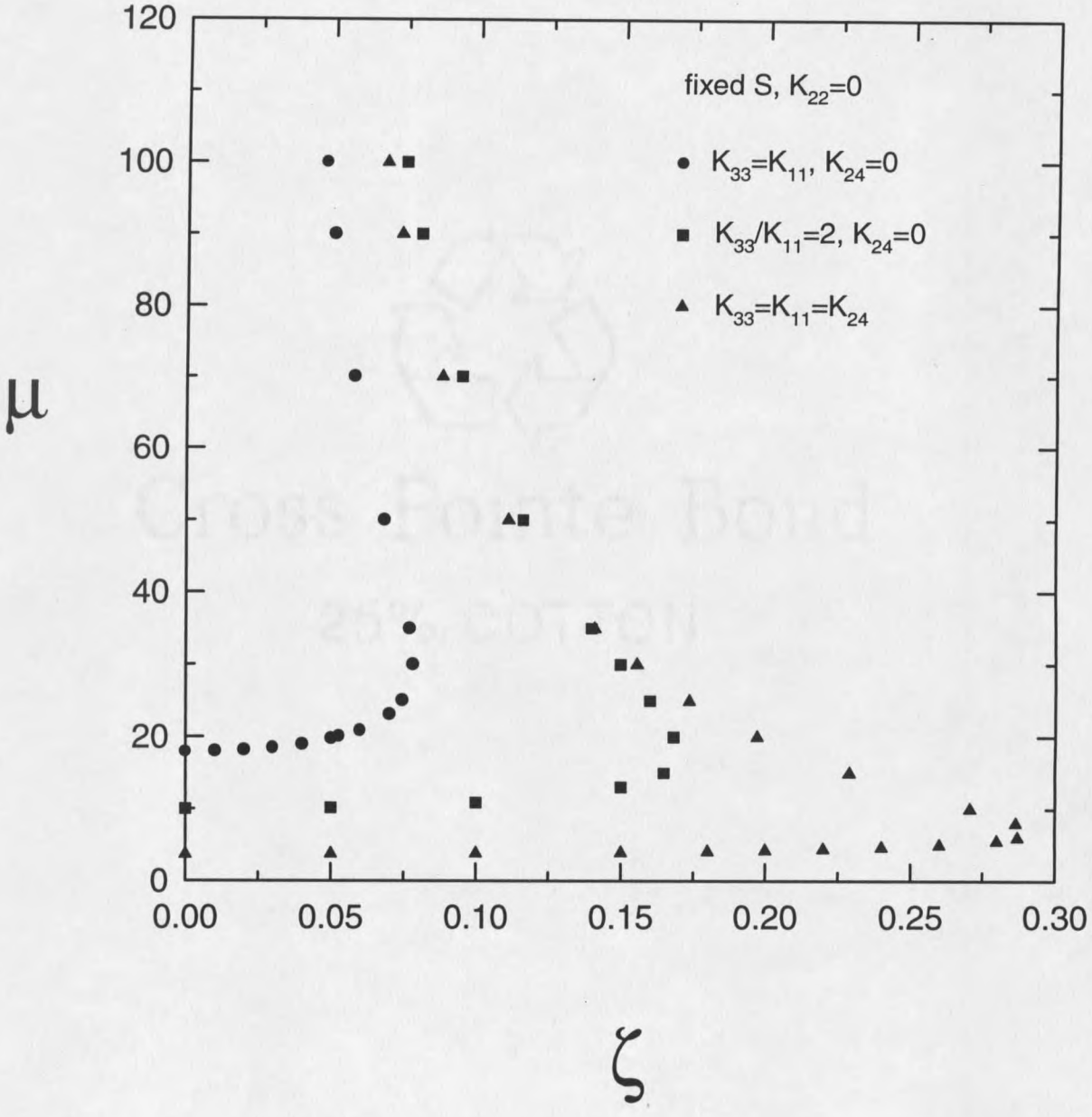

Figure 27. Phase diagrams in uniform-field approximation and the assumptions of uniform order parameter and no twist, obtained numerically by the solving Euler-Lagrange equations and using a 100×100 mesh. Transition boundaries for $K_{33}/K_{11} = 1$, $K_{33}/K_{11} = 2$, and $K_{33} = K_{11} = K_{24}$ are shown. Each phase boundary separates the stable phases of the radial on the left and the axial on the right.

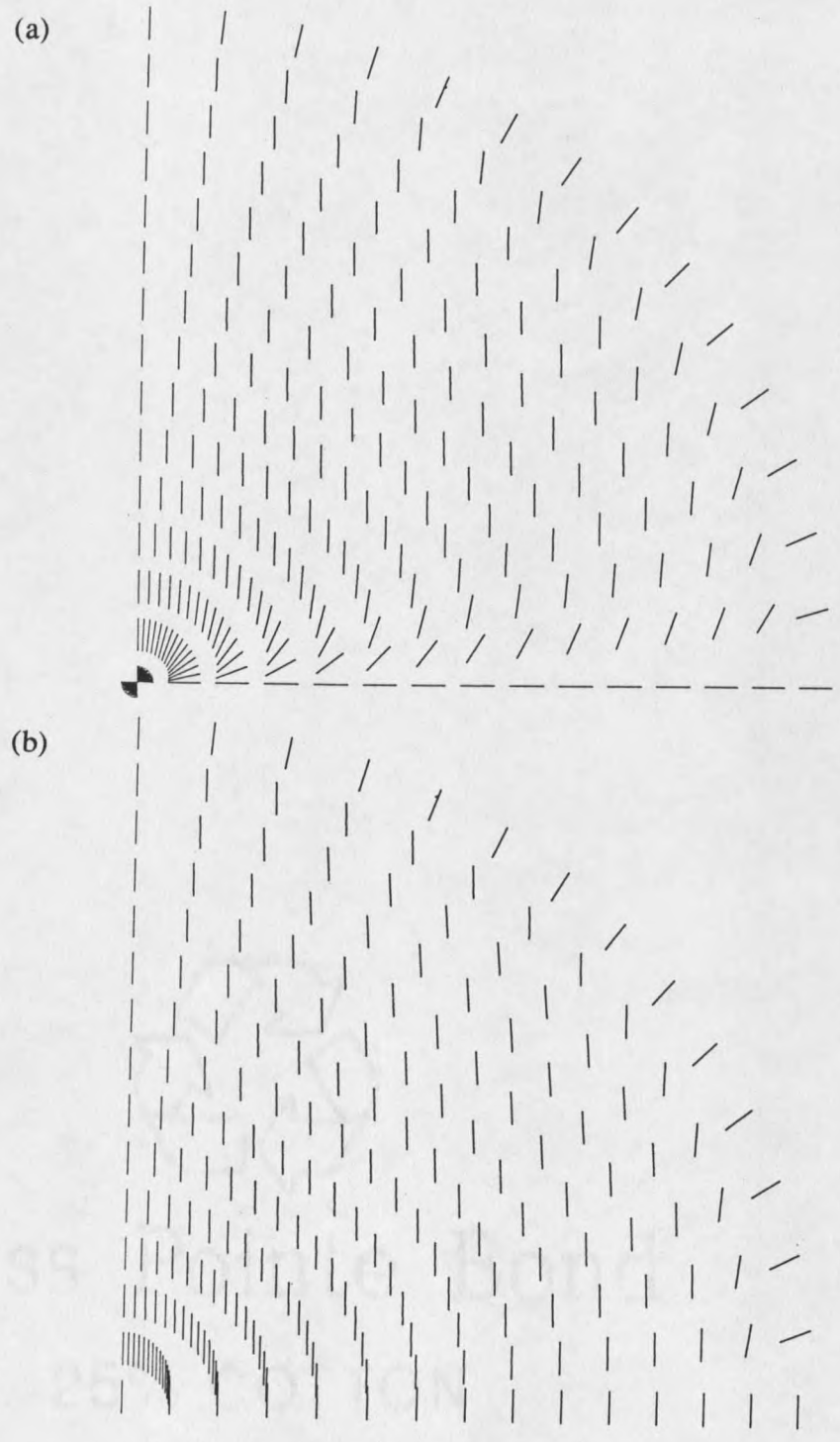

Figure 28. Director configurations of the nematic droplet in the assumptions of uniform order parameter, no twist, and no saddle-splay, obtained for $K_{33}/K_{11} = 1$ by calculating the stable (a) radial phase at $\mu = 60$, $\zeta = 0.4$ and (b) axial phase at $\mu = 60$, $\zeta = 0.7$. The two configurations only differ near the equator. The field is applied along the $\hat{z}$ axis.

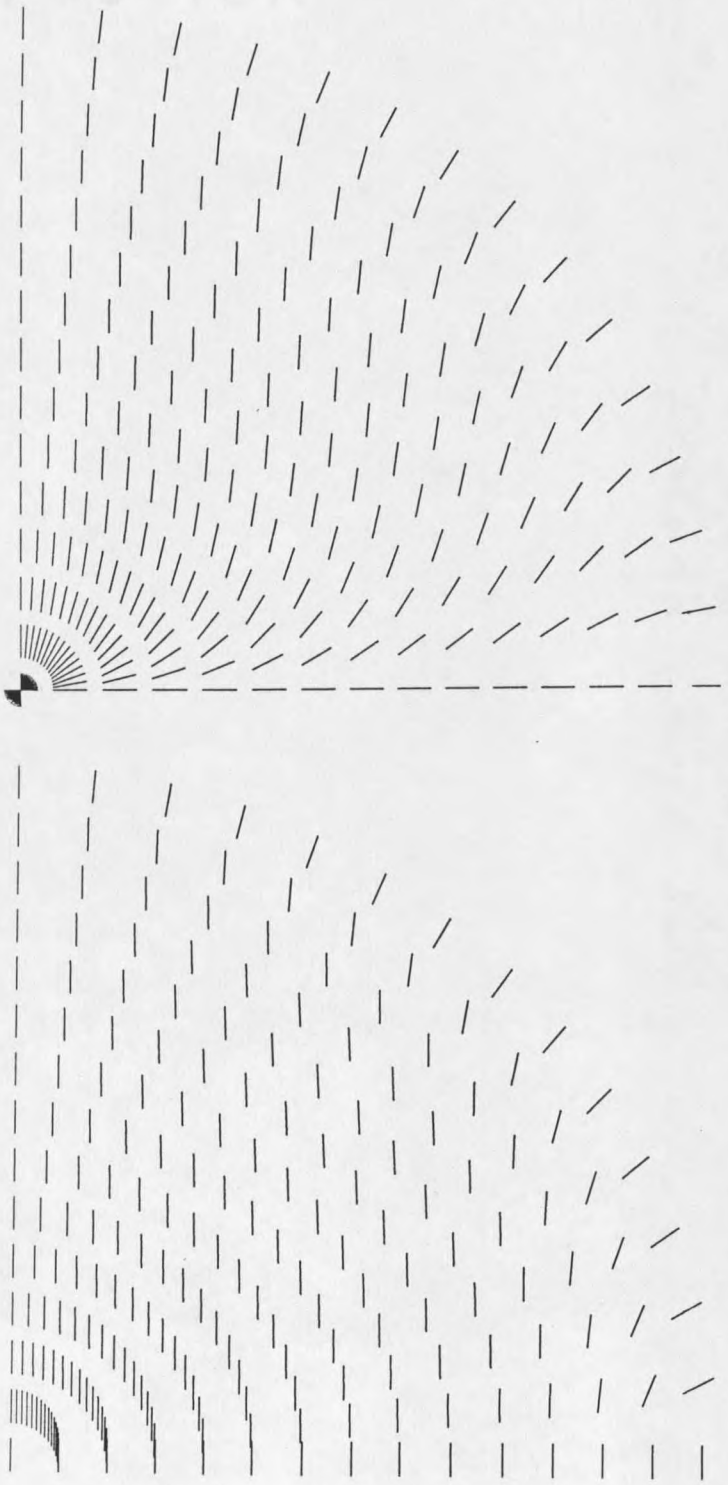

Figure 29. Director configurations obtained with the same assumptions as Figure 28 for $K_{33}/K_{11} = 2$ by calculating the stable (a) radial phase at $\mu = 60$, $\zeta = 0.2$ and (b) axial phase at $\mu = 60$, $\zeta = 0.4$. The two configurations differ not only near the equator but also in the bulk. The field is applied along the $\hat{z}$ axis.

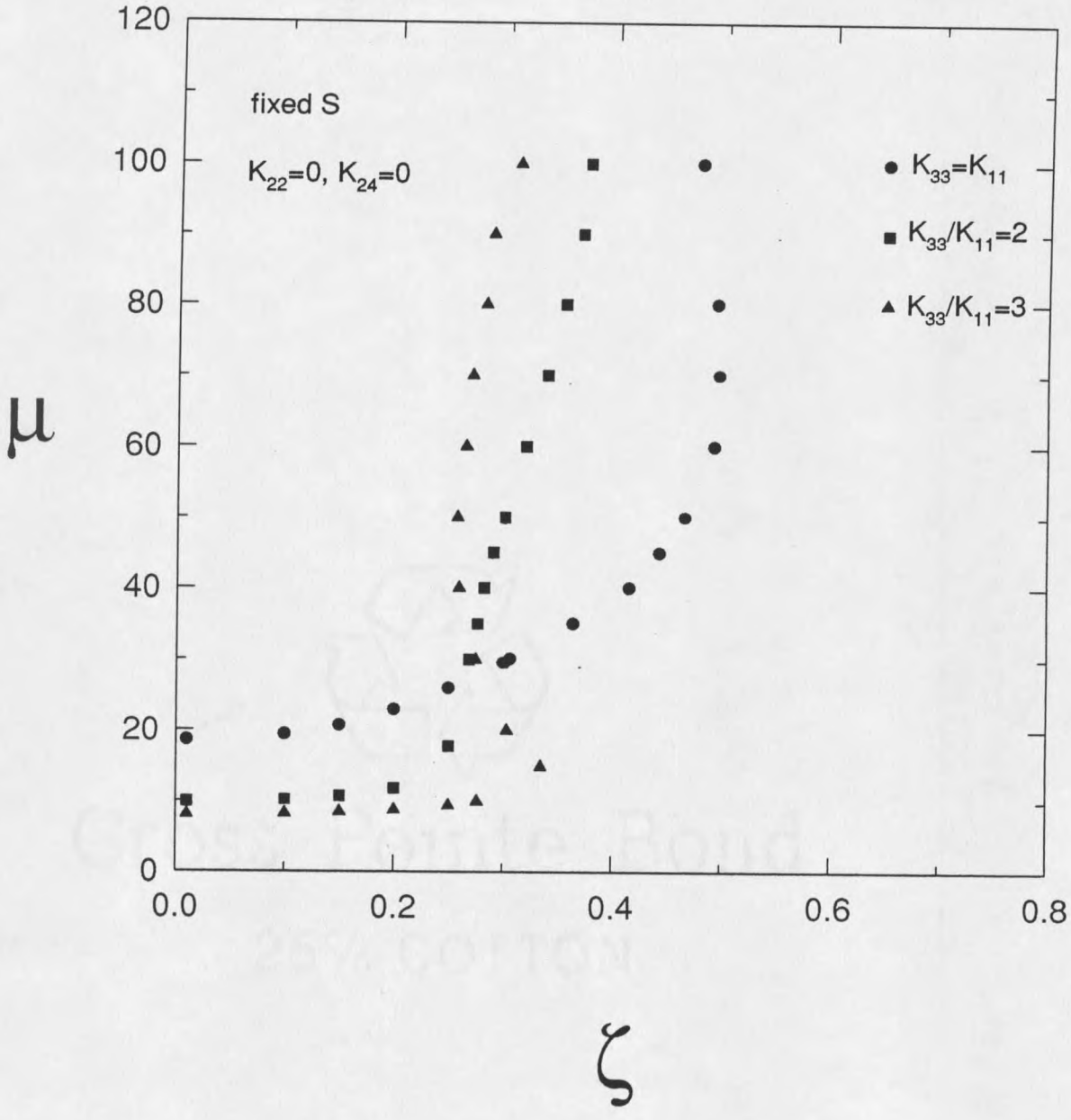

Figure 30. Phase diagrams in the assumptions of uniform order parameter, no twist, and no saddle-splay, obtained by using a 20×20 mesh and conjugate gradient technique for direct minimization. Transition boundaries for $K_{33}/K_{11} = 1$, $K_{33}/K_{11} = 2$, and $K_{33}/K_{11} = 3$ are shown. Each phase boundary separates the stable phases of the radial on the left and the axial on the right. Increasing bend-to-splay ratio causes the phase boundary to shift to the left.

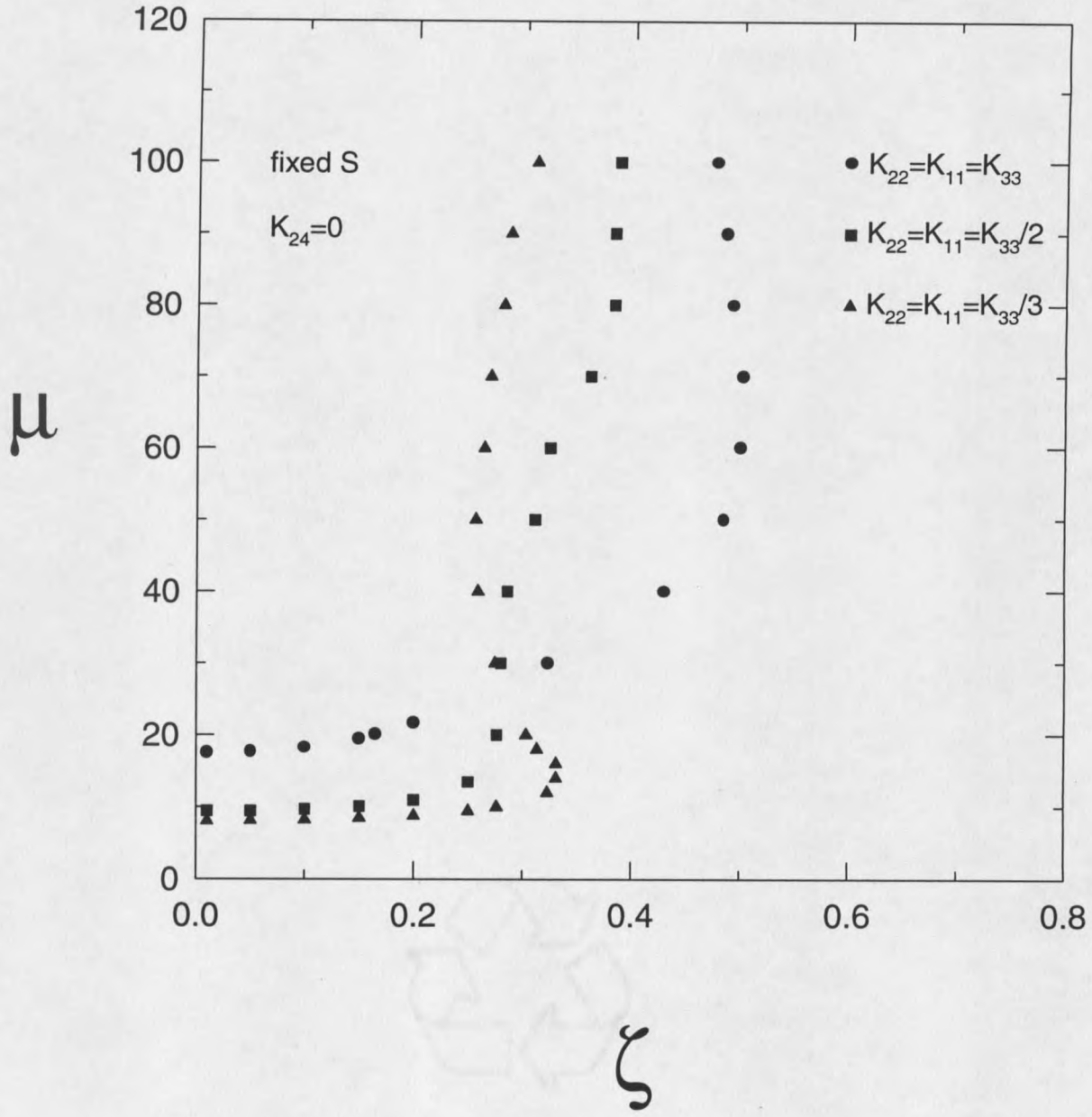

Figure 31. Phase diagrams are obtained by using the same assumptions and methods as Figure 30 for adding twist, i.e. $K_{22} = K_{11} = K_{33}$, $K_{22} = K_{11} = K_{33} / 2$, and $K_{22} = K_{11} = K_{33} / 3$ as shown. They do not differ much from those obtained in Figure 30.

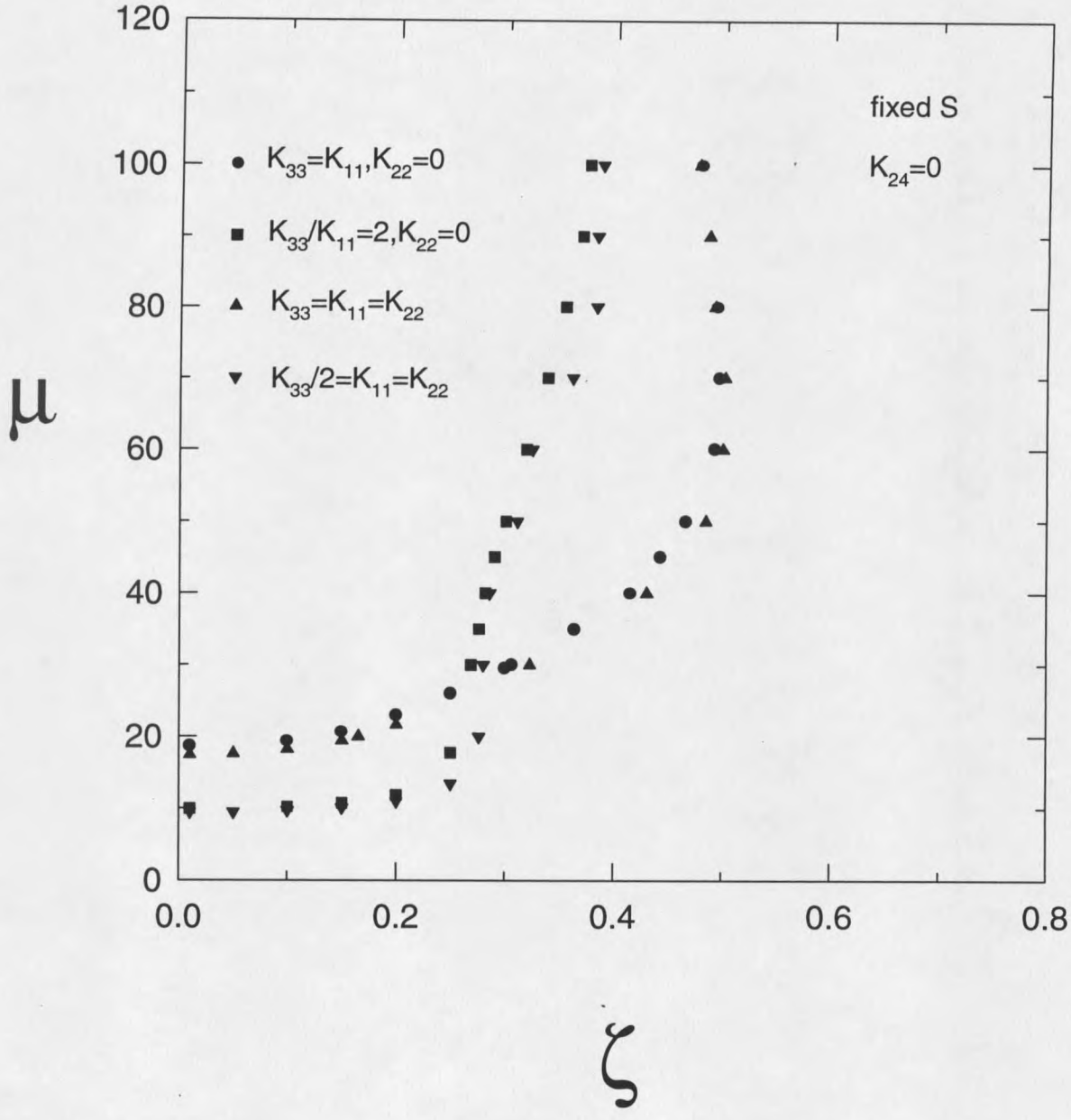

Figure 32. Comparison of the phase diagrams obtained in Figure 30 to those obtained in Figure 31. The phase boundaries with twist do not differ much from the boundaries without twist, comparing the $K_{22} = K_{11} = K_{33}$ with the $K_{11} = K_{33}$, $K_{22} = 0$, and comparing the $K_{22} = K_{11} = K_{33} / 2$ to the $K_{33}/K_{11} = 2$, $K_{22} = 0$.

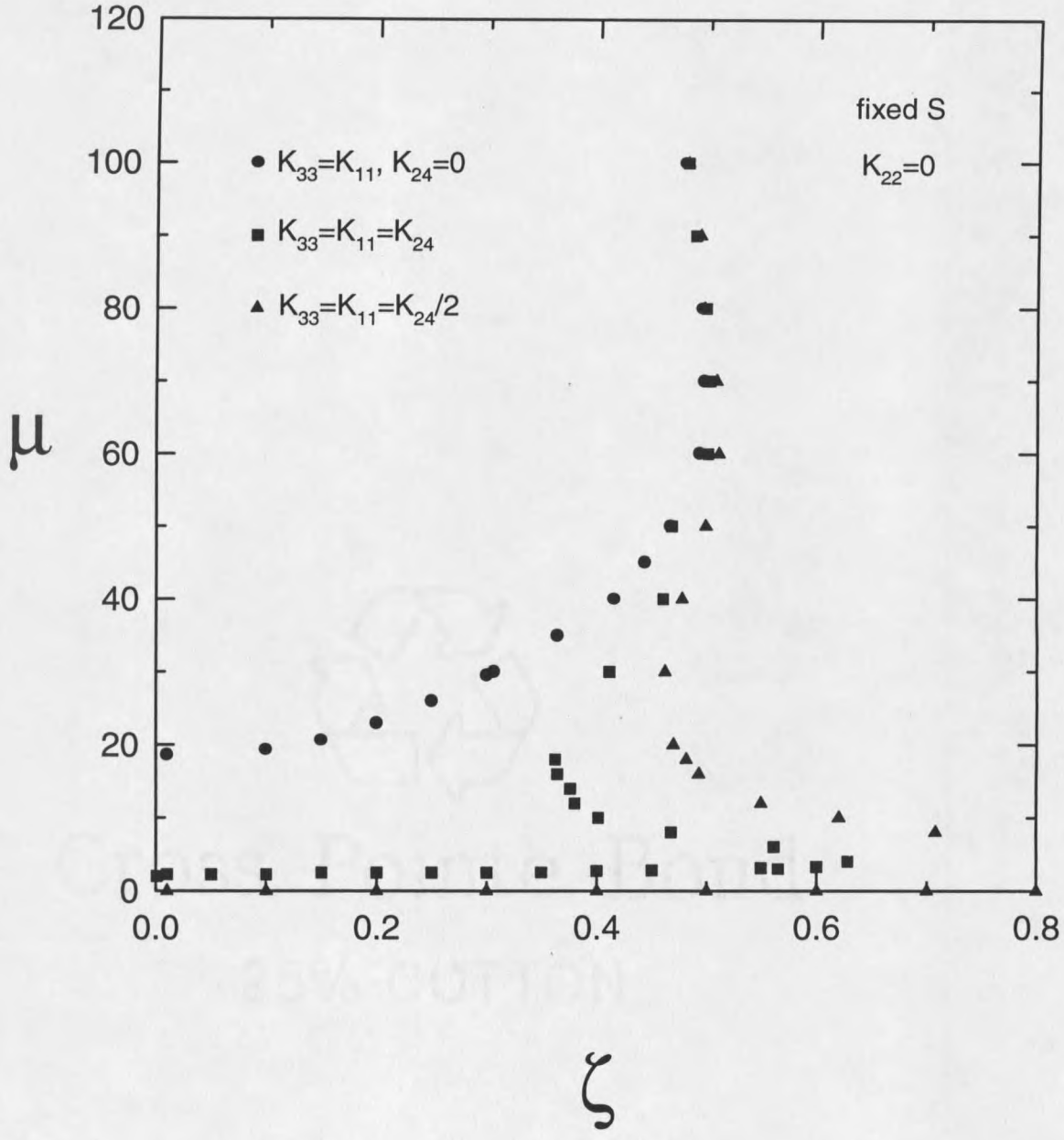

Figure 33. Phase diagrams in the assumptions of uniform order parameter and no twist, obtained by using a 20×20 mesh and conjugate gradient technique for direct minimization. The phase boundaries are obtained for $K_{11} = K_{33}$ without K_{24}, $K_{24} = K_{11} = K_{33}$, and $K_{24} / 2 = K_{11} = K_{33}$ as shown.

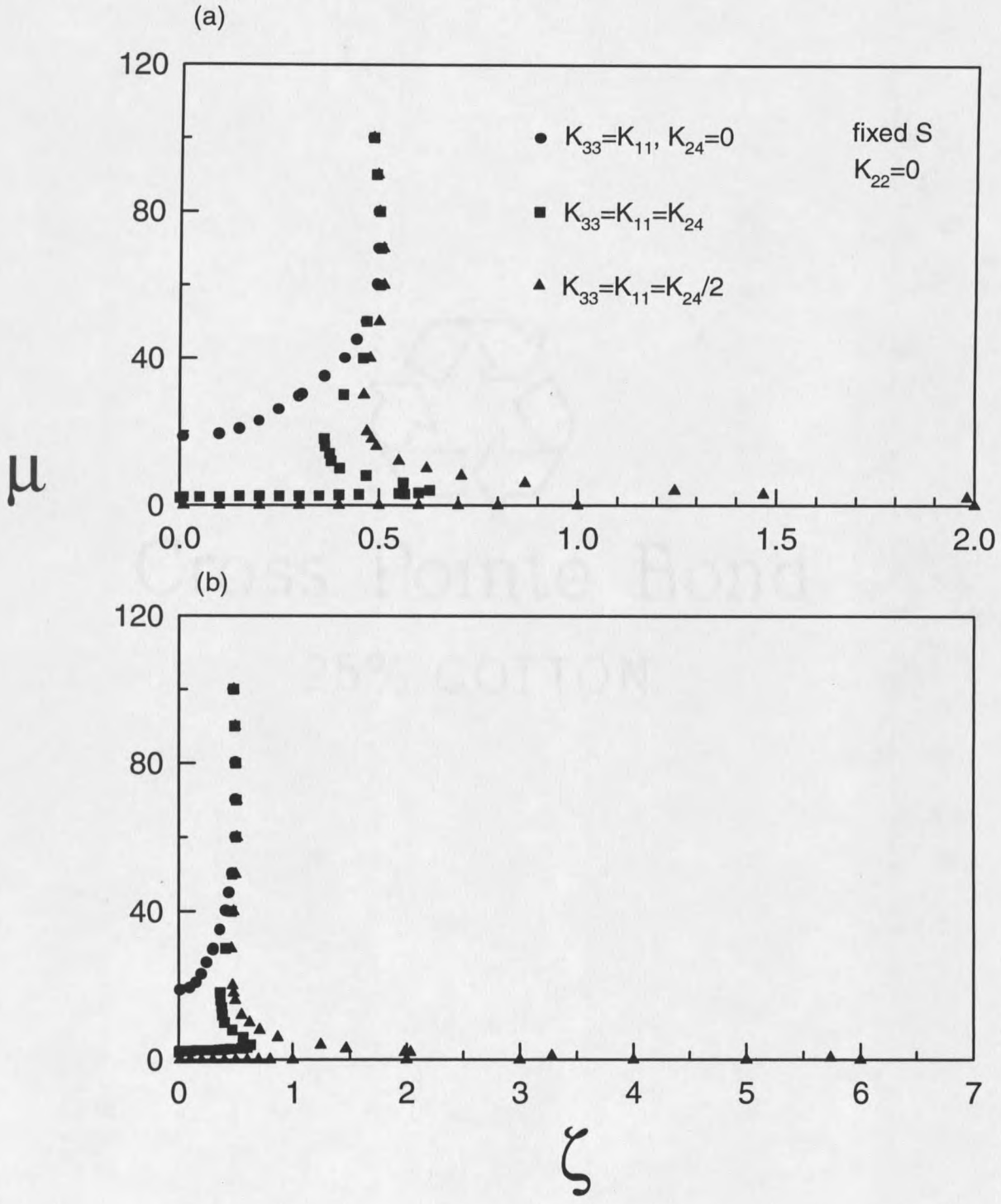

Figure 34. Phase diagrams obtained by extending the ζ's scale of the Figure 35 to (a) 2 and (b) 7.

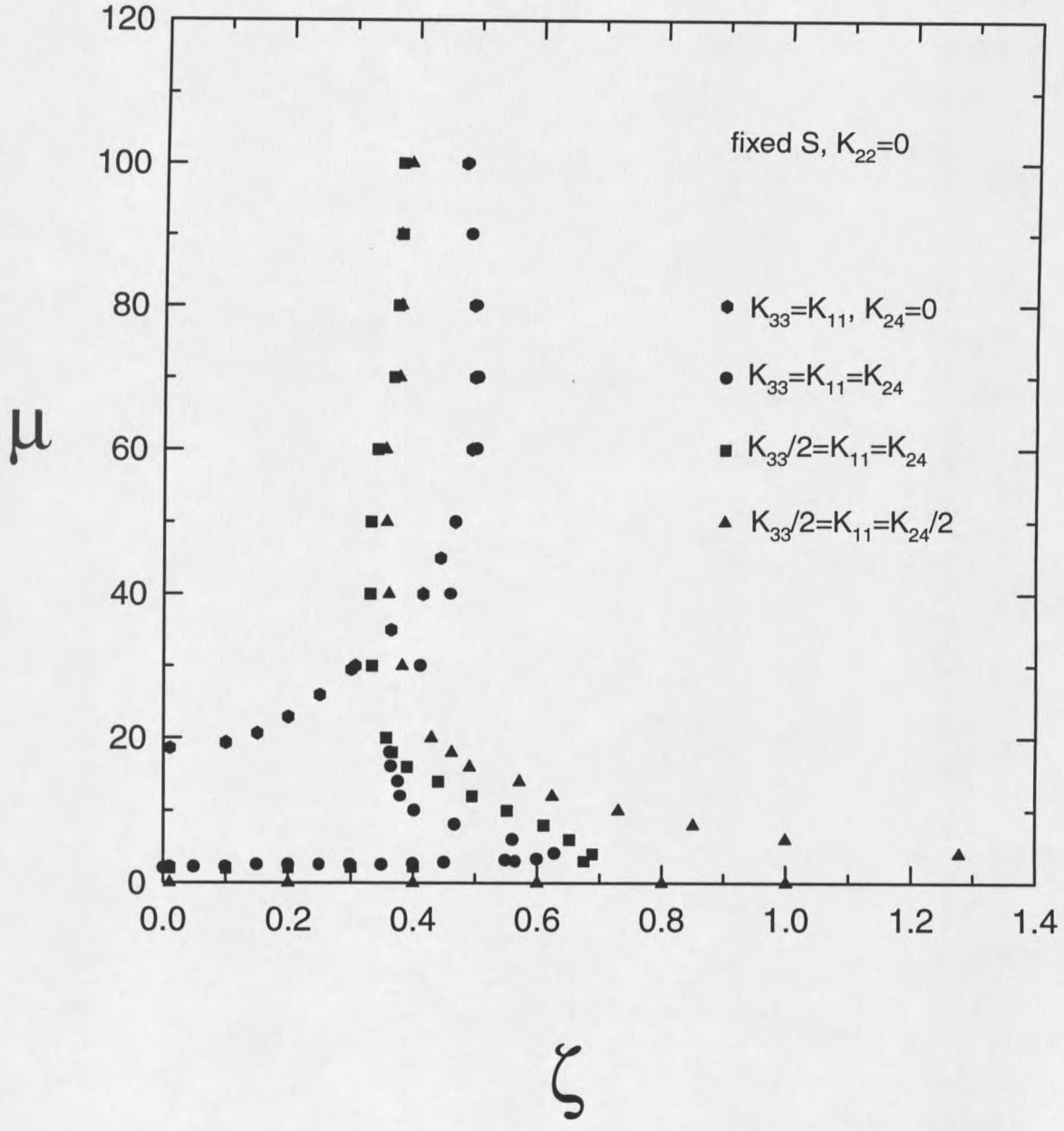

Figure 35. Phase diagrams obtained by using the same assumptions and methods as those used Figure 33. Phase boundaries for four sets of elastic constants are shown.

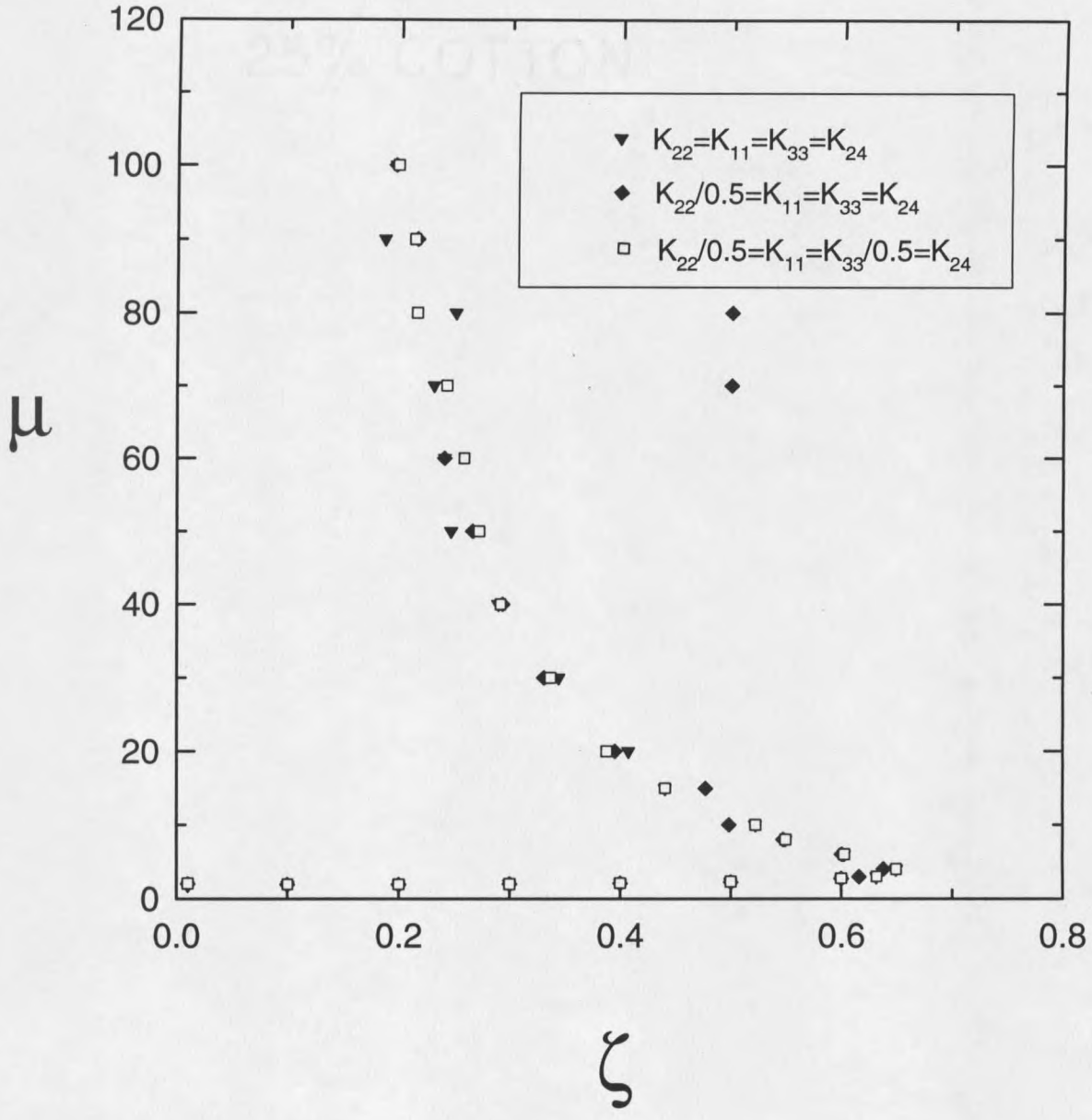

Figure 36. Phase diagrams in the uniform-order-parameter assumption for three combinations of all elastic constants (i.e. K_{11}, K_{22}, K_{33}, and K_{24}) as shown, obtained by using the conjugate gradient technique for direct minimization and a 20×20 mesh.

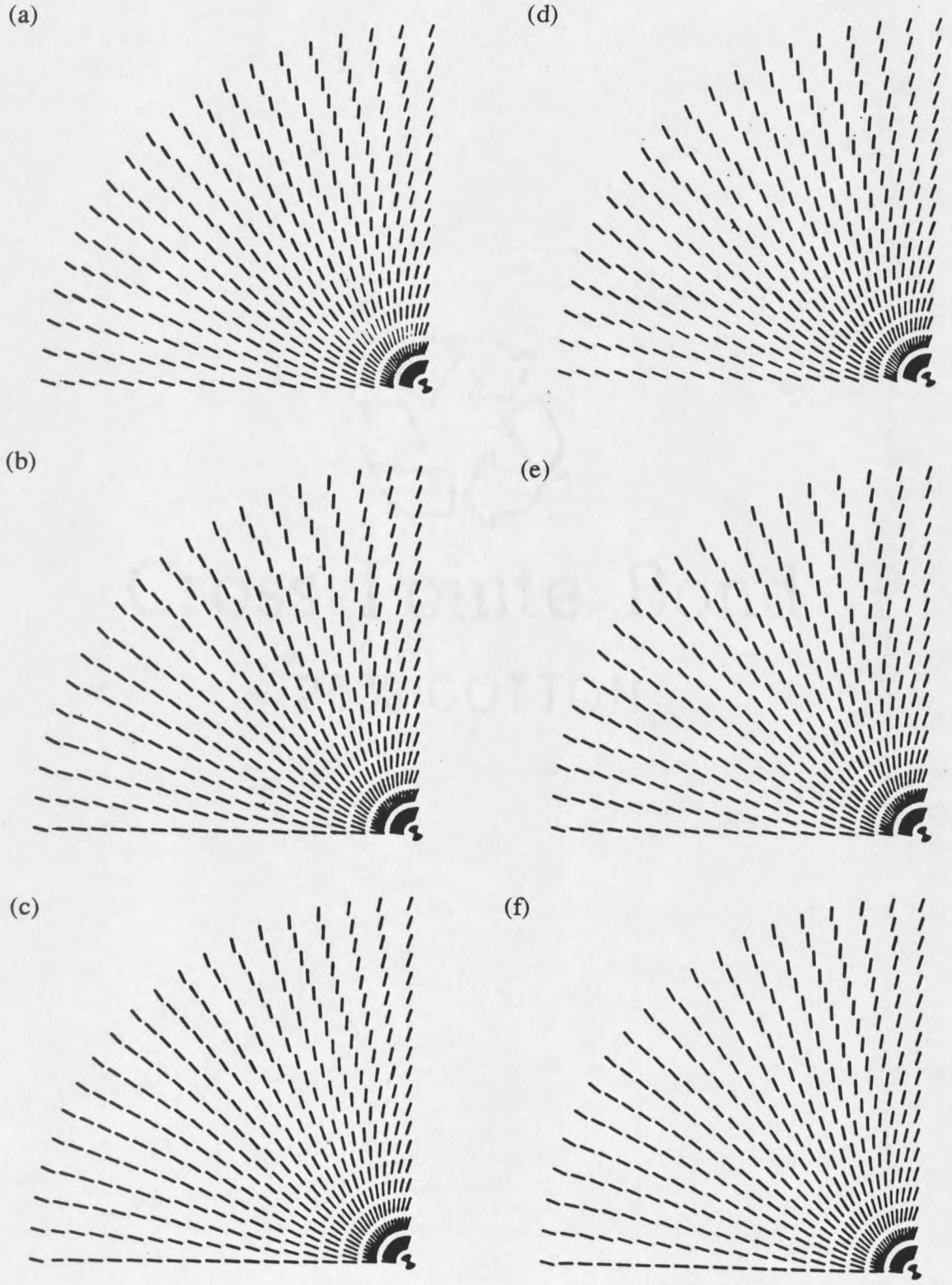

Figure 37. Twist configurations for $K_{22} / 0.5 = K_{11} = K_{33} / 0.5 = K_{24}$ in the uniform-order-parameter assumption, obtained by projecting the directors configurations on the $\theta - \varphi$, where the electric field is applied in the direction out of the paper at (a) $\mu = 60$, $\zeta = 0.1$ (b) $\mu = 60$, $\zeta = 0.2$, (c) $\mu = 60$, $\zeta = 0.3$, (d) $\mu = 100$, $\zeta = 0.1$, (e) $\mu = 100$, $\zeta = 0.2$, and (f) $\mu = 100$, $\zeta = 0.3$.

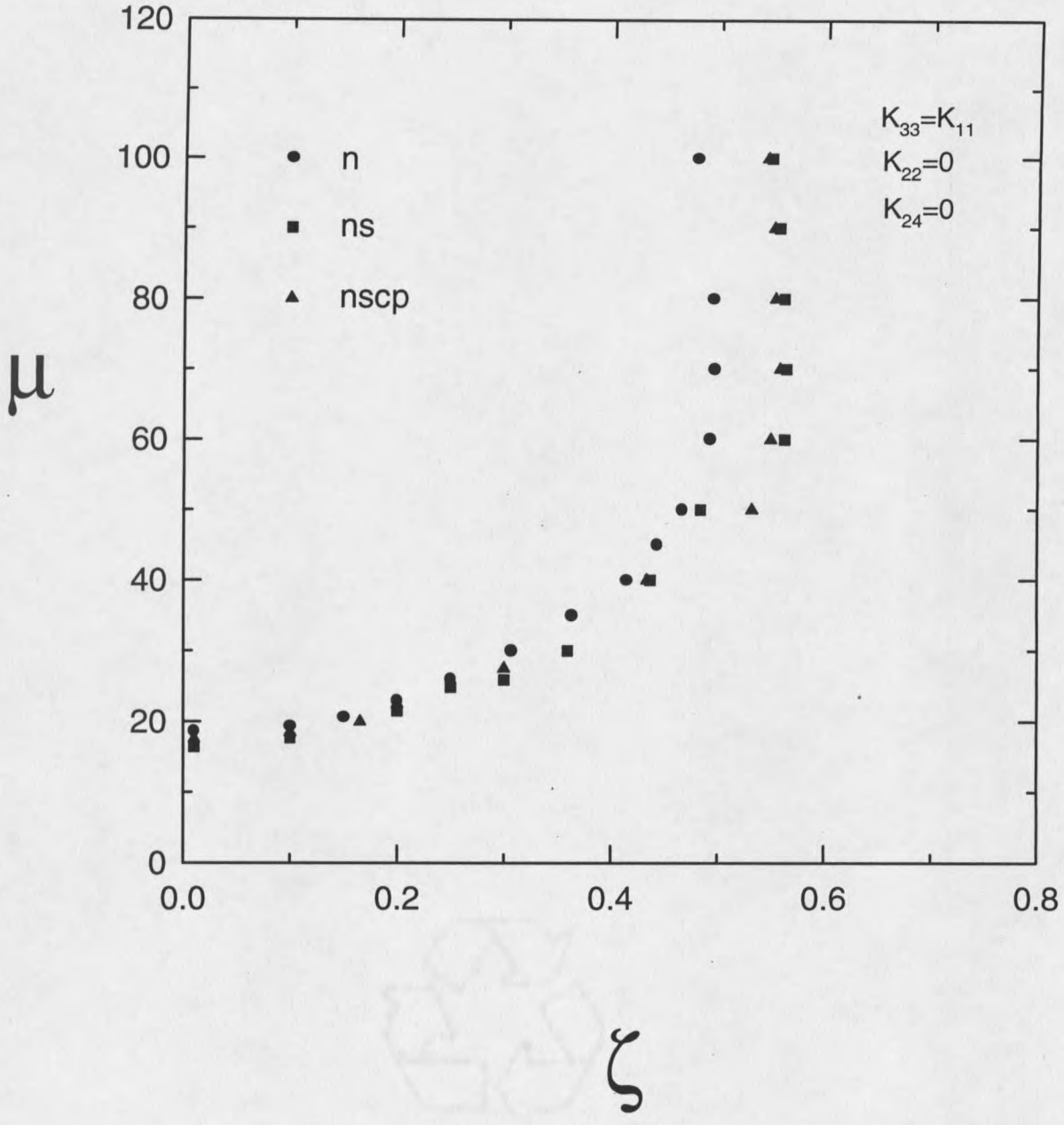

Figure 38. Phase diagrams obtained for the cases (a) with uniform order parameter, (b) with position-dependent order parameter but no coupling between director and order parameter, and (c) with position-dependent order parameter and full coupling between director and order parameter, indicated as n, ns, and nscp, respectively. The assumptions of no twist and no saddle-splay have been adopted in the numerical calculation done by using the conjugate gradient technique for direct minimization in a 20×20 mesh for $K_{11} = K_{33}$.

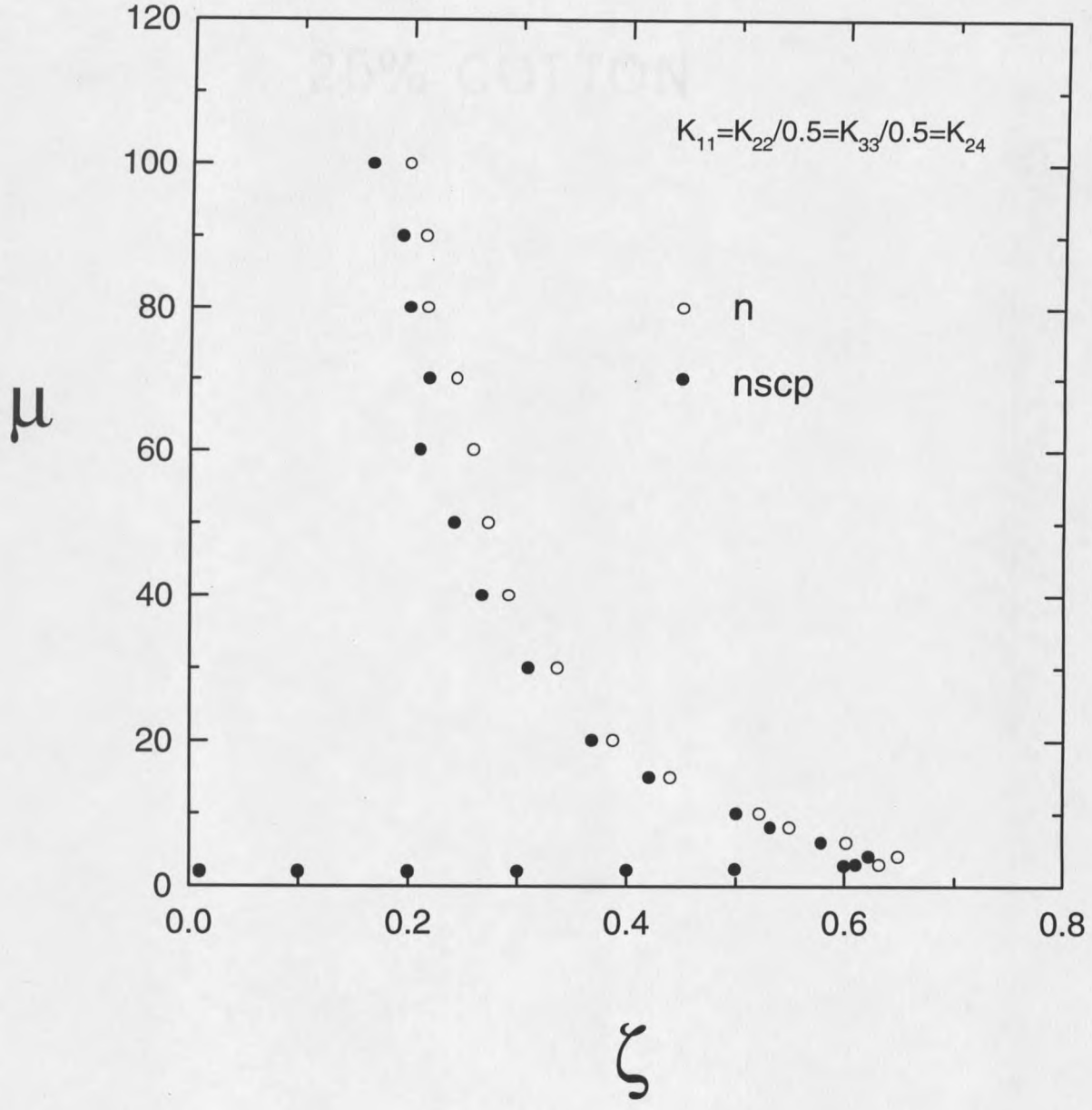

Figure 39. Comparison of phase diagrams obtained for the case with uniform order parameter to the case with full coupling between position-dependent order parameter and director. All of the elastic constants are included and $K_{22} / 0.5 = K_{11} = K_{33} / 0.5 = K_{24}$ for both phase boundaries. The boundaries do not differ much.

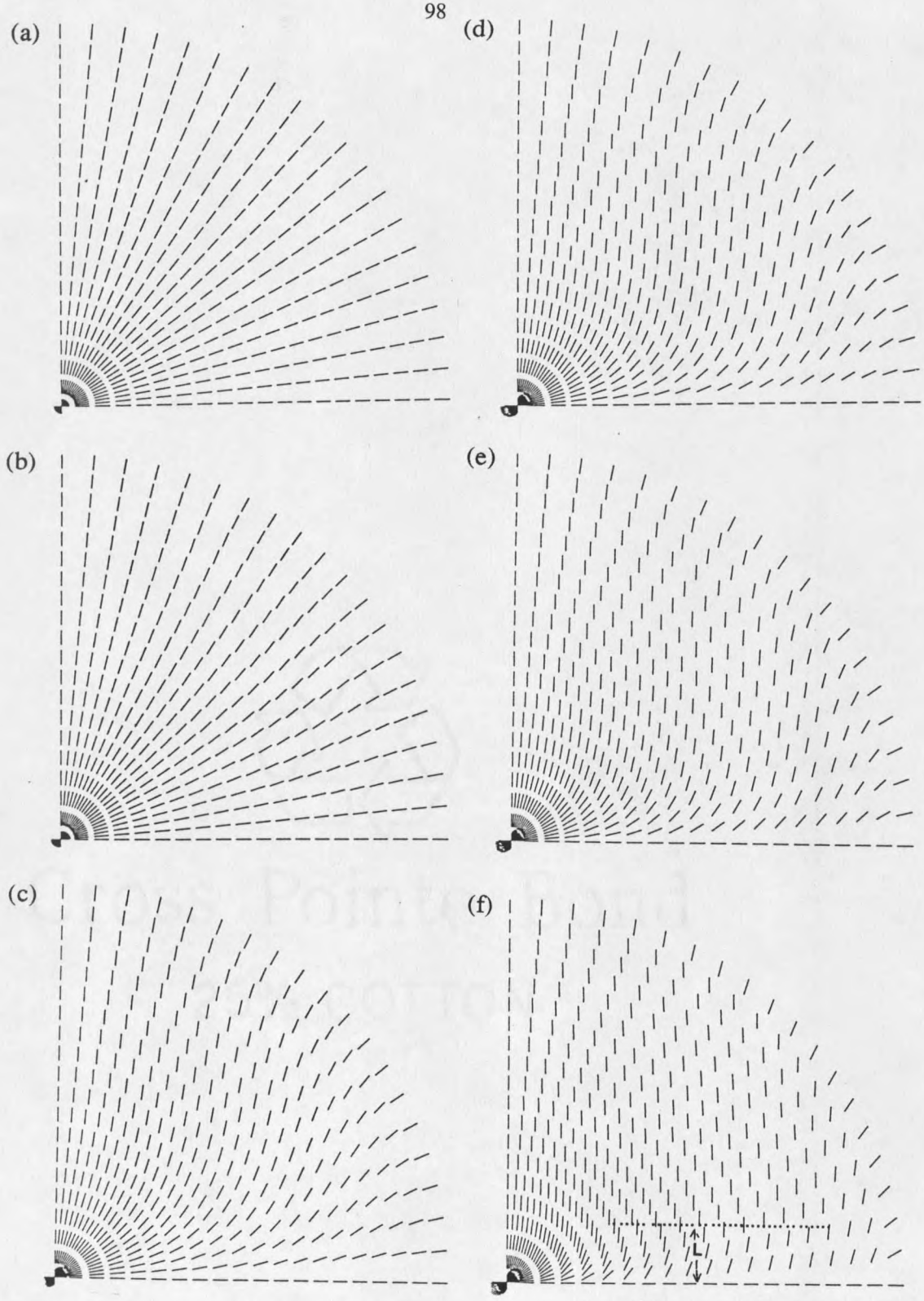

Figure 40. Director configurations obtained by using the same assumptions and methods as those used in Figure 38 (c) (i.e. nscp) at $\mu = 40$ and increasing field strength: (a) $\zeta = 0.01$, (b) $\zeta = 0.1$, (c) $\zeta = 0.2$, (d) $\zeta = 0.3$, (e) $\zeta = 0.4$, and (f) $\zeta = 0.9$. L indicates the thickness of the region where most of the directors are not parallel to the E-field direction ($\hat{z}$ -axis).

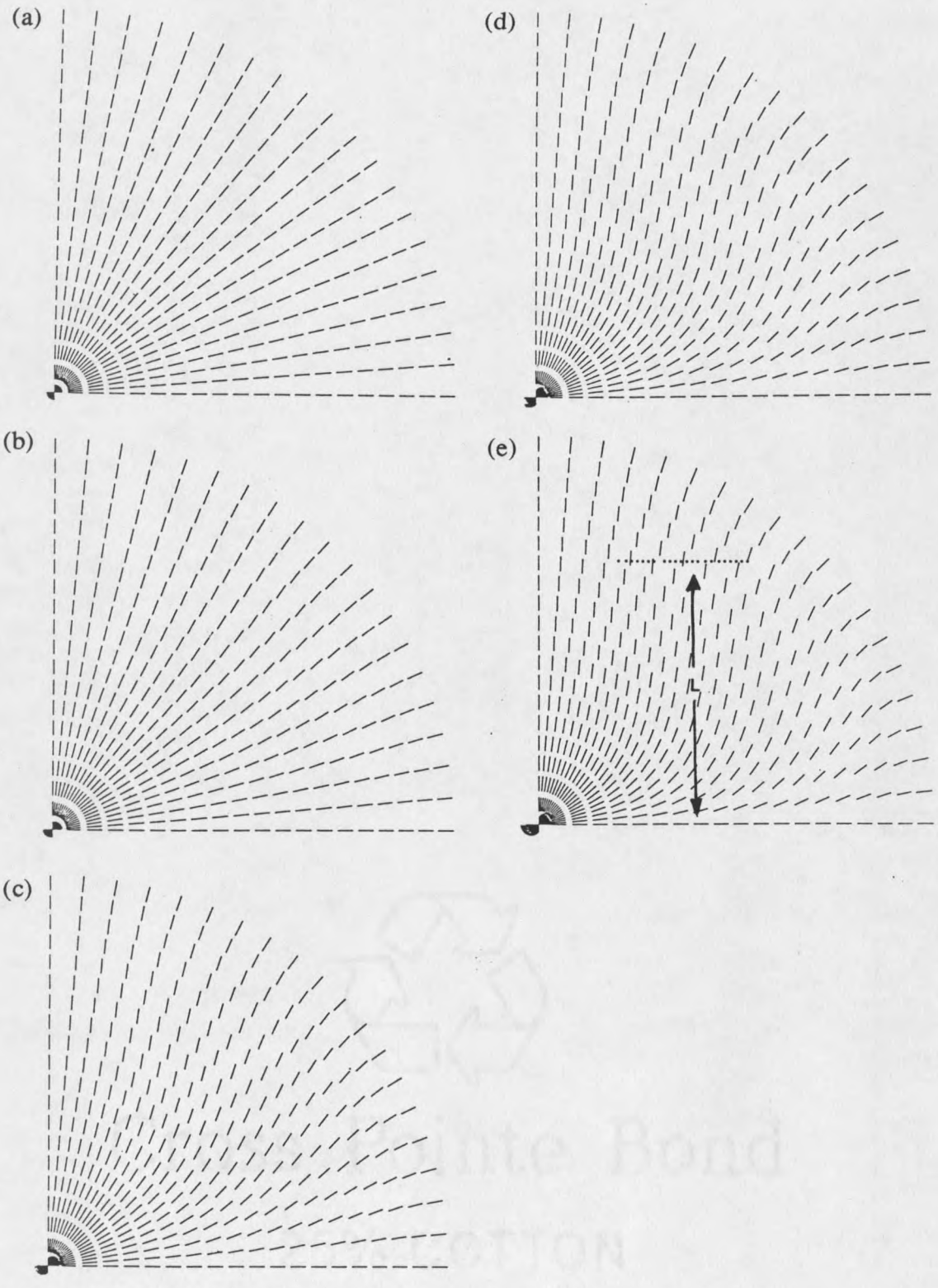

Figure 41. Director configurations obtained by using the same assumptions and methods as those used in Figure 40 at $\zeta = 0.1$ and increasing anchoring strength: (a) $\mu = 10$, (b) $\mu = 40$, (c) $\mu = 60$, (d) $\mu = 80$, and (e) $\mu = 100$. L also indicates the thickness of the region where most of the directors are not parallel to the E-field direction (z-axis).

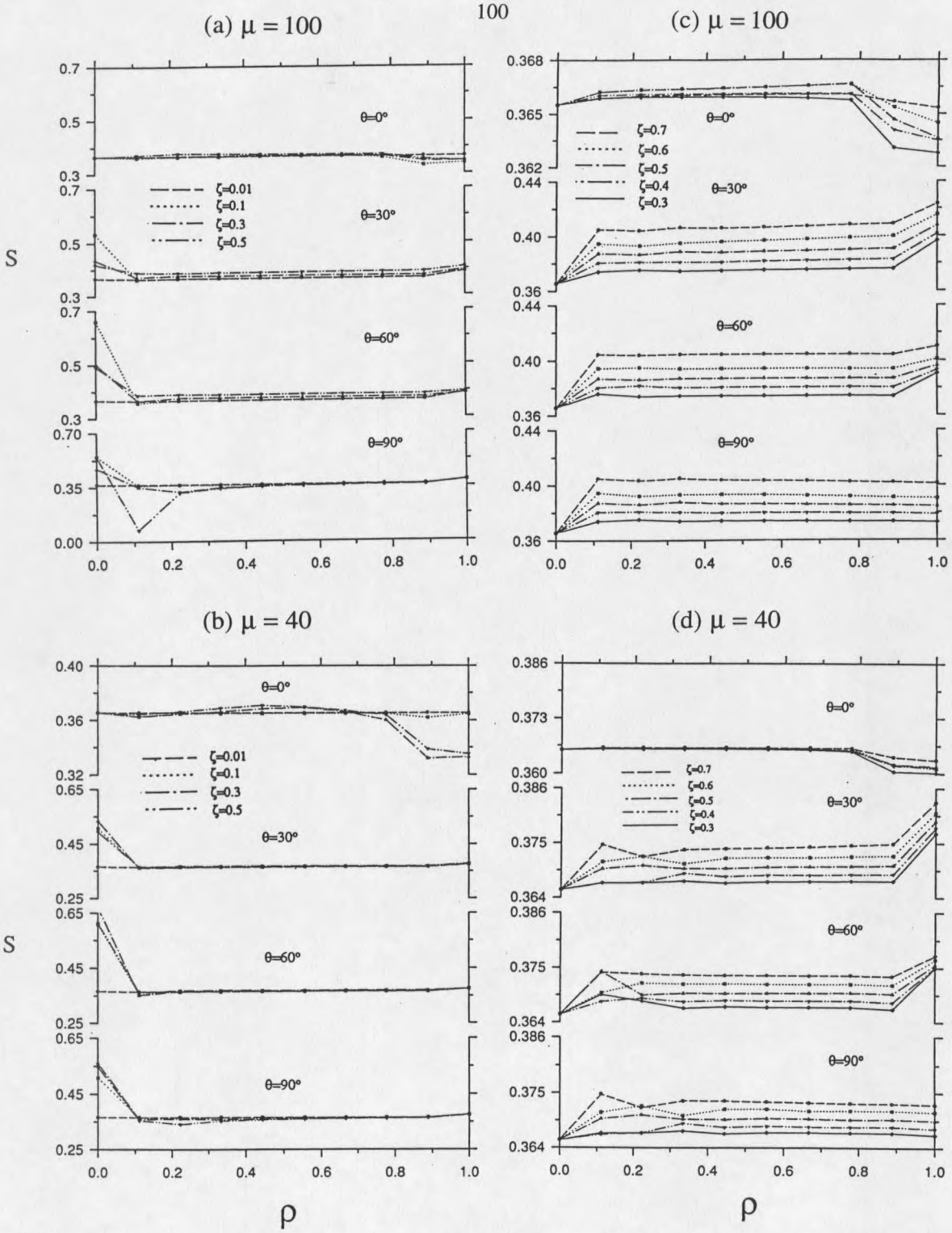

Figure 42. Position-dependent order parameter $S(\rho,\theta)$ obtained by using the same assumptions and methods as those used in Figure 38 (c) (i.e. nscp) for (a) radial phase at $\mu = 100$, (b) radial phase at $\mu = 40$, (c) axial phase at $\mu = 100$, and (d) axial phase at $\mu = 40$. Each branch in the radial phase (i.e. (a) and (b)) at a certain angle θ has four data lines obtained for $\zeta = 0.01, 0.1, 0.3, .0.5$ as shown, while $\zeta = 0.7, 0.6, 0.5, 0.4, 0.3$ in the axial phase (i.e. (c) and (d)).

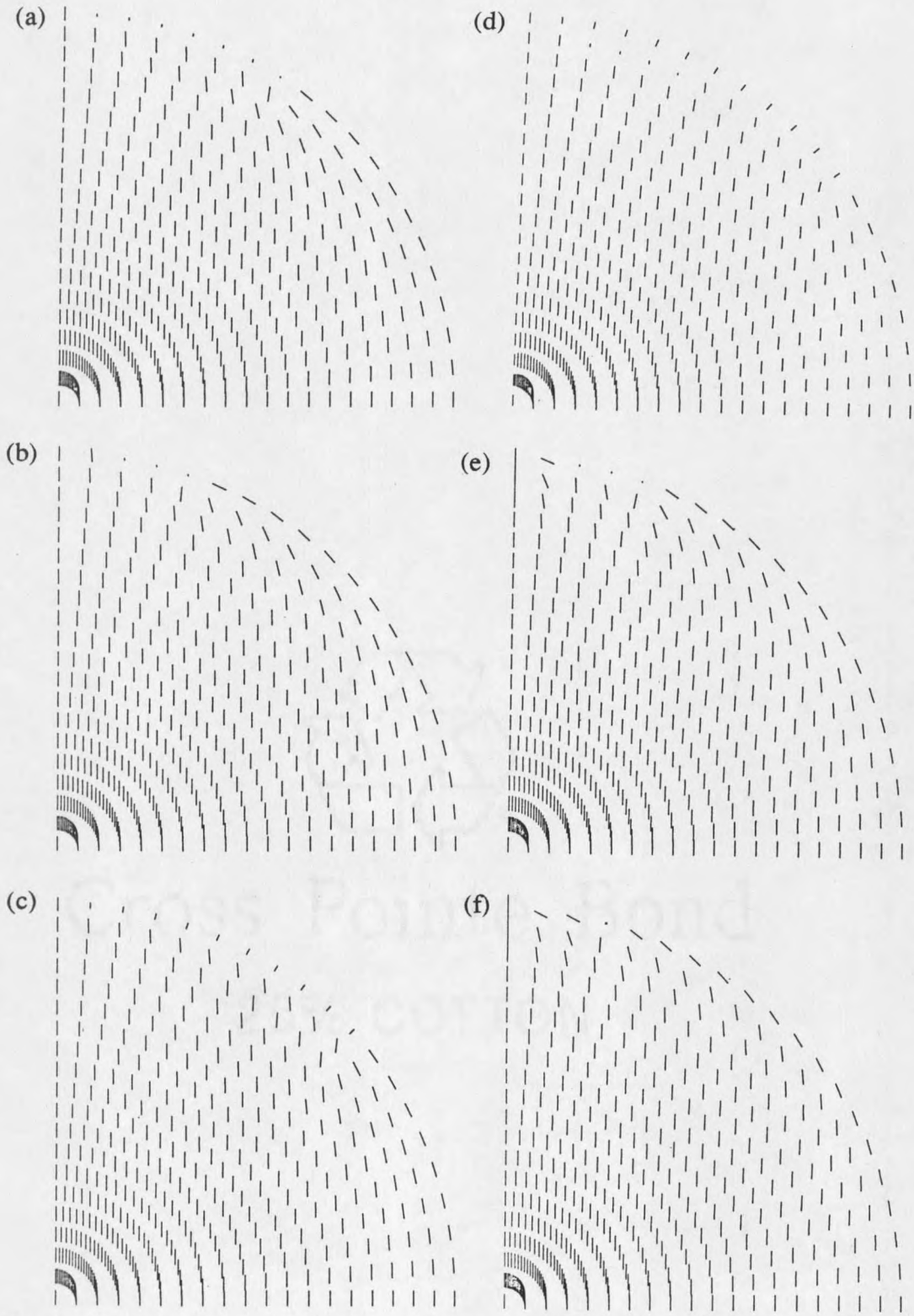

Figure 43. Director configurations of the nematic droplet with tangential anchoring, obtained for (a) $\mu = 100$, $\zeta = 0.01$, $R = 1\mu m$, $\Delta T = 1$, (b) $\mu = 60$, $\zeta = 0.01$, $R = 1\mu m$, $\Delta T = 1$, (c) $\mu = 100$, $\zeta = 0.01$, $R = 0.5\mu m$, $\Delta T = 1$, (d) $\mu = 100$, $\zeta = 0.01$, $R = 0.5\mu m$, $\Delta T = 1.5$, (e) $\mu = 60$, $\zeta = 0.1$, $R = 1\mu m$, $\Delta T = 1$, and (f) $\mu = 60$, $\zeta = 0.2$, $R = 1\mu m$, $\Delta T = 1$. The same assumptions and methods as those used in Figure 38 (c) (i.e. nscp) have been adopted. The field is applied along the $\hat{z}$ axis.

CHAPTER 5

CONCLUSIONS

Summary of Our Work

We have explored the director and order parameter configurations in spherical nematic microdroplets in an applied electric field, using for the internal field calculation a method that takes into account the effect of spatial field variations arising from the liquid crystal's anisotropic polarizability. The approach is based on the Landau-de Gennes model free energy, allowing the elastic constants to be unequal and taking into account the scalar order-parameter dependence of elastic constants up to second order, and determines the stable configurations by numerical solution of the Euler-Lagrange equations for the director with the Newton's relaxation method or by direct minimization of the total free energy with conjugate gradient or relaxation techniques

We have found that the inhomogeneity of the electric field inside the nematic droplet is significant in determining the stable configurations. For strong anchoring the influence of bend-to-splay ratio on the location of the phase boundary dominates. Our nonuniform-field approach predicts a greater range of stability for the radial phase than that predicted by the uniform-field approximation. In addition, the "reentrant" feature of the axial phase is lost when the twist deformation is not significant. The directors far from the equatorial plane reoriented along the E-field first then a domain wall near the equatorial plane appears as the $(\mu \times \zeta)$ increases. The twist elastic constant does have a

significant effect on the location of the phase boundary for strong anchoring when all elastic constants (i.e. K_{11}, K_{22}, K_{33}, and K_{24}) except the splay-bend elastic constant K_{13} are included. Particularly, the phase boundary is stable when the splay elastic constant is large compared to twist and bend elastic constants. The phase boundary looks more like that obtained in the uniform-field approximation. We predict a twist configuration when the droplet is viewed along the field. In addition, a mirror symmetry appears on the equatorial plane as the field increases. For weak anchoring the influence of the saddle-splay elastic deformation on the location of phase boundary dominates and the inclusion of the saddle-splay deformation stabilizes the radial phases even at very strong external field.

The spatial dependence of the order parameter does not affect the location of the phase boundary more than the various elastic deformations do. However, it does allow the creation of defect regions, where elastic energy is reduced by the suppression of the order parameter. Increasing external field strength would reduce the defect region. A smaller droplet radius and an increasing temperature difference $\Delta T = T - T_c^*$, where T_c^* is the temperature of supercooling limit, would increase the defect region.

Future Directions

The Splay-Bend Elastic Contribution

Unlike the splay, bend, twist, and saddle-splay elastic deformations, the splay-bend has received little experimental study and is not well understood theoretically. Particularly, the surface-like free energy of K_{24} term only contains derivatives in directions tangential to surface. But a singularity in normal derivatives at the surface would allow for an unbounded decrease (or increase depending on the sign of K_{13}) in the free energy of K_{13} term, so that the total free energy has no minimum for any nonzero K_{13}. Therefore,

we should not use direct minimization of the total free energy (Eq. (19)), which includes the K_{13} term. However, our approach, including the K_{13} term, can be carried out by solution of Euler-Lagrange equations, since it is always possible formally to derive Euler-Lagrange equations for any functional, although their solutions do not necessarily minimize the functional.

We have found that of all the terms in the Frank-Oseen free energy, the K_{13} contribution is the only one which cannot be transformed into expressions quadratic in first derivatives of the director field by using the normalization condition, but must include second derivatives. The normal mode picture proposed by Schmidt[40] does not include any K_{13} term, since that picture is explicitly constructed only from first derivatives of $\hat{n}$. Developing a theory that takes into account K_{13} term in explaining PDLC behavior will be an interesting direction of our work in the future.

Dynamic Approach

A dynamic approach to the problem is important because the dynamic behavior of the nematic liquid crystal in PDLC determines the switching time.

When we consider the dynamics of nematics, the velocity field $\bar{v}(\bar{r},t)$ should be also taken into account. Therefore the variables involved in the problem will be velocity field of the fluid $\bar{v}(\bar{r},t)$, director $\hat{n}(\bar{r},t)$, order parameter $S(\bar{r},t)$, and external electric field $E(\bar{r},t)$, all of which are time dependent. In addition, $\bar{v}$ and $\hat{n}$ are coupled vector fields since the reorientation of the director $\hat{n}$ can cause bulk fluid flow and the gradient of $\bar{v}$ produces a torque on the nematic liquid crystal.[90] An approach to this problem will require a larger and higher-speed computer system.

Testing Predictions

Some of our predictions have matched experimental results[5], as mentioned in Chapter 4. More accurate measurement[27,32,34,35] of the Oseen-Frank elastic constant ratios K_{22}/K_{11}, K_{33}/K_{11}, and K_{24}/K_{11} should be carried out to test our predictions. The phase diagrams can be determined experimentally by using a polarizing microscope to monitor the configuration transition of the nematic droplet with different radii at a "critical" strength of the external electric field.

REFERENCES CITED

1. E. Dubois-Violette and O. Parodi, J. Phys. (Paris) **30**, C4-57 (1969).
2. S. Candau, P. LeRoy, and F. Debeauvais, Mol. Crst. Liq. Cryst. **23**, 283 (1973).
3. A. Golemme, S. Zumer, D. W. Allender, and J. W. Doane, Phys. Rev. Lett. **61**, 2937 (1988).
4. J. H. Erdmann, S. Zumer, and J. W. Doane, Phys. Rev. Lett. **64**, 19 (1990).
5. V. G. Bondar, O. D. Lavrentovich, and V. M. Pergamenshchik, Sov. Phys. JETP **72**, 60 (1992).
6. S. Kralj and S. Zumer, Phys. Rev. A **45**, 2461 (1992).
7. S. Zumer and S. Kralj, Liq. Cryst. **12**, 613 (1992).
8. F. Xu, H.-S. Kitzerow, and P. P. Crooker, Phys. Rev. A **46**, 6536 (1992).
9. E. Berggren, C. Zannoni, C. Chiccoli, P. Pasini, and F. Semeria, Phys. Rev. E **49**, 614 (1994) and references therein.
10. G. E. Volovik and O. D. Lavrentovich, Sov. Phys. JETP **58**, 1159 (1983).
11. S. Zumer and J. W. Doane, Phys. Rev. A **34**, 3373 (1986).
12. O. D. Lavrentovich and E. M. Terent'ev, Sov. Phys. JETP **64**, 1237 (1986).
13. P. Drzaic, Mol. Cryst. Liq. Cryst. **154**, 289 (1988).
14. I. Vilfan, M. Vilfan, and S. Zumer, Phys. Rev. A **40**, 4724 (1989).
15. R. Ondris-Crawford, E. P. Boyko, B. G. Wagner, J. H. Erdmann, S. Zumer, and J. W. Doane, J. Appl. Phys. **69**, 1 (1991).
16. S. Kralj, S. Zumer and D. W. Allender, Phys. Rev. A **43**, 2943 (1991).
17. W. Huang and G. F. Tuthill, Phys. Rev. E **49**, 570 (1994).
18. M. J. Press and A. S. Arrott, Phys. Rev. Lett. **33**, 403 (1974).
19. M. J. Press and A. S. Arrott, J. Phys. (Paris) **36**, C1-177 (1975).
20. R. D. Williams, J. Phys. A **19**, 3211 (1986).
21. O. D. Lavrentovich and V. V. Sergan, Nuovo Cimento **12 D**, 1219 (1990).
22. P. E. Cladis and M. Kleman, J. Phys. (Paris) **33**, 591 (1972).

23. C. E. Williams, P. Pieranski and P. E. Cladis, Phys. Rev. Lett. **29**, 90 (1972).

24. R. B. Meyer, Phil. Mag. **27**, 405 (1973).

25. A. Saupe, Mol. Cryst. Liq. Cryst. **21**, 211 (1973).

26. A. Pargellis, N. Turok and B. Yurke, Phys. Rev. Lett. **67**, 1570 (1991).

27. D. W. Allender, G. P. Crawford, and J. W. Doane, Phys. Rev. Lett. **67**, 1442 (1991).

28. G. P. Crawford, M. Vilfan, J. W. Doane, and I. Vilfan, Phys. Rev. A **43**, 835 (1991).

29. I. Vilfan, M. Vilfan, and S. Zumer, Phys. Rev. A **43**, 6875 (1991).

30. G. P. Crawford, D. W. Allender, J. W. Doane, M. Vilfan, and I. Vilfan, Phys. Rev. A **44**, 2570 (1991).

31. G. P. Crawford, D. W. Allender, and J. W. Doane, Phys. Rev. A **45**, 8693 (1992).

32. G. P. Crawford, J. A. Mitcheltree, E. P. Boyko, W. Fritz, S. Zumer, and J. W. Doane, Appl. Phys. Lett **60**, 29 (1992).

33. R. Ondris-Crawford, S. Zumer, and J. W. Doane, Phys. Rev. Lett. 70, 194 (1993).

34. A. Scharkowski, G. P. Crawford, S. Zumer, and J. W. Doane, J. Appl. Phys. **73**, 7280 (1993).

35. R. D. Polak, G. P. Crawford, B. C. Kostival, J. W. Doane, and S. Zumer, Phys. Rev. E **49**, R978 (1994).

36. J. W. Doane, N. A. Vaz, B.-W. Wu, and S. Zumer, Appl. Phys. Lett. **48**, 269 (1986).

37. J. W. Doane, A. Golemme, J. L. West, J. B. Whitehead, and B.-G. Wu, Mol. Cryst. **165**, 511, (1988).

38. J. W. Doane, Mater. Res. Bull. **XVI**, 22 (1991), and references therein.

39. G. P. Crawford and J. W. Doane, Condensed Matter News **1**, 5 (1992), and references therein.

40. V. H. Schmidt, Phys. Rev. Lett. **64**, 535 (1990).

41. A. I. Derzhanski and H. P. Hinov, Phys. Lett. **56A**, 465 (1976); **62A**, 36 (1977); J. Phys. (Paris) **38**, 1013 (1977).

42. H. P. Hinov, J. Phys. (Paris) Lett. **38**, l215 (1977).

43. H. P. Hinov and A. I. Derzhanski, J. Phys. (Paris) Colloq. **40**, C3-505 (1979).

44. H. P. Hinov, Mol. Cryst. Liq. Cryst. **148**, 197 (1987); **168**, 7 (1989); **178**, 53 (1990); **191**, 389 (1990); **209**, 339 (1991).

45. C. Oldano and G. Barbero, J. Phys. (Paris) Lett. **46**, l451 (1985); Phys. Lett. **110A**, 213 (1985).

46. G. Barbero and C. Oldano, Nuovo Cimento **D 6**, 479 (1985).

47. A. Strigazzi, Mol. Cryst. Liq. Cryst. **152**, 435 (1987).

48. G. Barbero, N. V. Madhusudana ,and C. Oldano, J. Phys. (Paris) **50**, 2263 (1989).

49. G. Barbero and A. Strigazzi, Mol. Cryst. Liq. Cryst. **5**, 693 (1989).

50. G. Barbero and C. Oldano, Mol. Crsyt. Liq. Cryst. **168**, 1 (1989); **170**, 99 (1989).

51. N. V. Madhusudana and R. Pratibha, Mol. Cryst. Liq. Cryst. **179**, 207 (1990).

52. G. Barbero and C. Oldano, Mol. Crsyt. Liq. Cryst. **168**, 1 (1989); **170**, 99 (1989); **195**, 199 (1991).

53. G. Barbero, A. Sparavigan, and A. Strigazzi, Nuovo Cimento **D 12**, 1259 (1990).

54. A. Sparavigan, L. Komitov and A. Strigazzi, Phys.Scr. **43**, 210 (1991).

55. G. Barbero and Yu. A. Kosevich, Phys. Lett. **A 170**, 41 (1992).

56. G. Barbero and G. Durand, Phy. Rev. E **48**, 1942 (1993).

57. V. M. Pergamenshchik, Phys. Rev. E **47**, 1881 (1993).

58. V. M. Pergamenshchik, Phys. Rev. E **48**, 1252 (1993).

59. V. M. Pergamenshchik, P. I. C. Teixeira, and T. J. Sluckin, Phy. Rev. E **48**, 1265 (1993).

60. P. G. de Gennes, Mol. Cryst. Liq. Cryst. **12**, 193 (1971).

61. F. Gramsbergen, L. Longa, and W. H. de Jeu, Phys. Rep. **135**, 195 (1986).

62. G. Vertogen and W. H. de Jeu, *Thermotropic Liquid Crystals, Fundamentals* (Spring-Verlag,, New York, 1988), Sec. 5.2.

63. G. Vertogen and W. H. de Jeu, *Thermotropic Liquid Crystals, Fundamentals* (Spring-Verlag,, New York, 1988), Sec. 5.3.

64. C. W. Oseen, Trans. Faraday Soc. **29**, 883 (1933).

65. H. Zocher, Trans. Faraday Soc. **29**, 945 (1933).

66. F. C. Frank, Disc. Faraday Soc. **25**, 19 (1958).

67. Vertogen and W. H. de Jeu, *Thermotropic Liquid Crystals, Fundamentals* (Spring-Verlag,, New York, 1988), Sec. 6.4.

68. W. H. de Jeu, Mol. Cryst. Liq. Cryst. **63**, 83 (1981).

69. W. H. de Jeu and W. A. P. Claassen, J. Chem. Phys. **67**, 3705 (1977).

70. F. Leenhouts and A. J. Dekker, J. Chem. Phys. **74**, 1956 (1981).

71. J. Nehring and A. Saupe, J. Chem. Phys. **54**, 337 (1971).

72. J. Nehring and A. Saupe, J. Chem. Phys. **56**, 5527 (1972).

73. J. Nehring and A. Saupe, J. Chem. Phys. **75**, 5118 (1981).

74. G. Vertogen and W. H. de Jeu, *Thermotropic Liquid Crystals, Fundamentals* (Spring-Verlag, New York, 1988), Secs. 12.1~12.3.

75. E. B. Priestley, P. J. Wojtowitz, and P. Sheng, *Introduction to Liquid Crystals* (Plenum, New York, 1975), Ch. 10.

76. P. G. de Gennes, *The Physics of Liquid Crystals* (Clarendon press, Oxford, 1974), Sec. 3.2.2.

77. E. B. Priestley, P. J. Wojtowitz, and P. Sheng, *Introduction to Liquid Crystals* (Plenum, New York, 1975), Sec. 3.2.

78. J. Mathews and R. L. Walker, *Mathematical Methods of Physics* (Addison-Wesley, New York, 1970), Sec. 7.1.

79. A. Rapini and M. Papoular, J. Phys. (Paris) Colloq. **30**, C4-54 (1969).

80. P. Sheng, Phys. Rev. Lett. **37**, 1059 (1976).

81. P. Sheng, Phys. Rev. A. **26**, 1610 (1982).

82. G. Barbero and G. Durand, J. Physique **47**, 2129 (1986).

83. G. Barbero, E. Miraldi, and A. Stepanescu, J. Appl. Phys. **68**, 2063 (1990).

84. G. P. Crawford, R. Stannarius, and J. W. Doane, Phys. Rev. A **44**, 2558 (1991).

85. G. J. Borse, *FORTRAN 77 and Numerical Methods for Engineers* (PWS-Kent, Boston, 1991).

86. S. L. Alder & T. Piran, Rev. Mod. Phys. **56**, 1 (1984).

87. W. H. Press, B. P. Flannery, S. A. Teukolsky, and W. T. Vetterling, *Numerical Recipes (FORTRAN Version)* (Cambridge University Press, Cambridge, 1989), Ch. 10.

88. W. F. Ames, *Numerical Methods for Partial Differential Equations* (Academic, New York, 1977).

89. Private communications with Prof. George F. Tuthill.

90. P. G. Gennes, *The Physics of Liquid Crystals* (Clarendon press, Oxford, 1974), Chapter 5.

APPENDIX

APPENDIX

COMPUTER CODES IN FORTRAN LANGUAGE

```
c CGNSCPMU20.FOR - Program to determine axial/radial phase boundary by comparing
c free energies, and successive bracketing in fieldfactor at
c constant mu, with inhomogeneous field.
c Conjugate gradient method is used to find equilibrium director configuration
c Order parameter field is permitted to vary spatially
c Including all the elastic deformations except mixed splay-bend, that is,
c K11(splay), K22(twist), K33(bend), and K24(saddle-splay).
      implicit real*8(a-h,o-z)
      real*8 mulist(9),cross(9)
      common/dropletparms/R,h11,h22,h33,h24,af,bf,cf,df,de,ep,w0,seq,ef
      common/simulparms/ngrid,npts,mm,nanneal,xlim,klim,dr,dth,pi,ipar,
     1ct(20),st(20)
      data mulist/100.d0,90.d0,80.d0,70.d0,60.d0,50.d0,40.d0,30.d0,
     1 20.d0/

c Droplet parameters
      R    = 1.d-4
      h11  = 5.d-7
      af   = 1.3d6
      bf   = 1.836d7
      cf   = 4.05d7
      df   = 6.d-7
      de   = 13.8d0
      ep   = 5.2d0
      seq  = bf*(1.d0+dsqrt(1.d0 - 4.d0*af*cf/bf**2))/(2.d0*cf)
      de   = de/seq
      h11  = h11/seq**2
      h22  = 0.5d0*h11
      h33  = 0.5d0*h11
      h24  = h11
      ef   = (2.d0/9.d0)*(h11+h33)

c Simulation parameters
      ngrid   = 20
      npts    = 1200
      mm      = 10001
      nanneal = 1
      xlim    = 5.d-4
      bdryun  = 2.d-3
      ftol    = 3.d-6
      klim    = 10000
      pi      = dacos(-1.d0)
      dth     = pi/(2.d0*(ngrid-1))
      dr      = R/(ngrid-1)

c Initialize the arrays of sine and cotangent
      do 24 j=1,ngrid
        th=dth*(j-1)
        st(j)=dsin(th)
        ct(j) = 0.d0
        if (j.gt.1) ct(j) = dcos(th)/st(j)
   24 continue

c Start the calculation of the boundary by picking successive
c values of the fieldfactor
      do 100 jmu = 1,9
        cross(jmu) = 0.d0
        down = 0.d0
        up = 1.d0
        write(6,*)up,down
        ipar=1
        call energy(mulist(jmu)*seq,up,fax,ftol)
        write(6,*)ipar,fax
        ipar=0
        call energy(mulist(jmu)*seq,up,frad,ftol)
        write(6,*)ipar,frad
```

```
          if (frad.lt.fax) goto 100

     10   trial = (up+down)/2.d0
          write(6,*)up,down,trial
          ipar=1
          call energy(mulist(jmu)*seq,trial,fax,ftol)
          ipar=0
          call energy(mulist(jmu)*seq,trial,frad,ftol)

          if (frad.gt.fax) then
            up = trial
          else
            down = trial
          endif

          if ((up-down).gt.bdryun) then
             goto 10
          else
             cross(jmu) = (up+down)/2.d0
          endif

    100 continue
        open(unit=10,file='nscpmu20.dat',status='new')
        do 200 jmu=1,9
          write(10,210)ngrid,cross(jmu),mulist(jmu)
    200 continue
        write(10,*)'R=',r,'xlim=',xlim,'bdryun.=',bdryun
        write(10,*)'ftol=',ftol,'nanneal=',nanneal
    210 format(2x,i4,2(4x,e14.6))
        close(unit=10)

        stop
        end
c ***************************************************************************
        subroutine energy(zmu,zfld,fax,ftol)
        implicit real*8 (a-h,o-z)
        common/dropletparms/R,h11,h22,h33,h24,af,bf,cf,df,de,ep,w0,seq,ef
        common/simulparms/ngrid,npts,mm,nanneal,xlim,klim,dr,dth,pi,ipar,
       1ct(20),st(20)
        common/field/fmag(20,20),fdir(20,20)
        dimension a(20,20),b(20,20),s(20,20),
       1achk(20,20),bchk(20,20),schk(20,20),
       1amom(4)

        fieldfactor = zfld
        xmu = zmu
        w0fin = xmu*h11/R
        dmu = xmu/nanneal
        dw0 = w0fin/nanneal

c Initialize a(i,j) to be pure axial or pure radial before relaxation,
c b(i,j) to be a small, and s to be equilibrium value everywhere
        do 10 i=1,ngrid
          do 20 j=1,ngrid
            a(i,j)=ipar*dth*(j-1)
            b(i,j) = 0.01d0
            s(i,j) = seq
c            if (i.eq.1) s(i,j) = ipar*seq
            achk(i,j) = a(i,j)
            schk(i,j) = s(i,j)
     20   continue
     10   continue

c Find the equilibrium electric field *and* director configurations.
c Anneal the anchoring parameter to the desired value.
c The maximum number of steps in the iterative process is MM.
```

```
      do 50 k=1,mm
        w0 = min(k*dw0,w0fin)
        ymu = min(k*dmu,xmu)
        b1 = fieldfactor*ymu*(ep+de*seq+2.d0)*((4.d0*pi)**0.5d0)
     1       /(R*dsqrt(de*seq/h11)*2.0d0)

c First find the E-field from the director configuration at the surface.
c The quantities p and pp are, resp., the radial and tangential
c (theta) components of the electric field, at the site (i,j)
      call surface(a,b,s,amom,ep,de,r,b1)
      do 51 i=2,ngrid
        do 53 j=1,ngrid
          x=dcos((j-1)*dth)
          call psum(p,pp,dr,i,x,amom)
          fmag(i,j) = dsqrt(p**2+pp**2)
          fdir(i,j) = - datan(pp/p)
   53   continue
   51 continue

c Next find the equilibrium configuration for the director, fixing the
c electric field configuration:
      call frpmn(a,b,s,ftol,iter,fax)

c Compare the new director configuration with the old; if the maximum
c change is less than xlim, stop the process, but if not then continue.
      xmxa = 0.d0
      xmxb = 0.d0
      xmxs = 0.d0
      do 60 i=1,ngrid
        do 70 j=1,ngrid
          xchka = dabs(a(i,j)-achk(i,j))
          xchkb = dabs(b(i,j)-bchk(i,j))
          xchks = dabs(s(i,j)-schk(i,j))
          if (xmxa.lt.xchka) xmxa = xchka
          if (xmxb.lt.xchkb) xmxb = xchkb
          if (xmxs.lt.xchks) xmxs = xchks
          achk(i,j) = a(i,j)
          bchk(i,j) = b(i,j)
          schk(i,j) = s(i,j)
   70   continue
   60 continue
c      write(*,*)k,ipar,xmxa,xmxb,xmxs
      if ((xmxa.lt.xlim).and.(xmxb.lt.xlim).and.(xmxs.lt.xlim).and.
     1(k.ge.(nanneal)))
     1    goto 100
      if (k.ge.klim) go to 100

   50 continue
  100 continue
      return
      end

c *********************************************************************
      subroutine total(x,ftotal)
c This subroutine calculates the total free energy for
c the particular director configuration a(i,j) and field
c configuration fmag(i,j),fdir(i,j)
      implicit real*8(a-h,o-z)
      common/dropletparms/R,h11,h22,h33,h24,af,bf,cf,df,de,ep,w0,seq,ef
      common/simulparms/ngrid,npts,mm,nanneal,xlim,klim,dr,dth,pi,ipar,
     1ct(20),st(20)
      common/field/fmag(20,20),fdir(20,20)
      dimension a(20,20),b(20,20),s(20,20),dadt(20,20),dbdt(20,20),
     1dsdt(20,20),dadr(20,20),dbdr(20,20),dsdr(20,20),x(1200)

c Restore the arrays a(i,j), b(i,j), and s(i,j) from x(k)
```

```
      do 5 i=1,ngrid
        do 4 j=1,ngrid
          a(i,j) = x((i-1)*ngrid+j          )
          b(i,j) = x((i-1)*ngrid+j+ngrid**2)
          s(i,j) = x((i-1)*ngrid+j+2*ngrid**2)
    4   continue
    5 continue

c Calculate theta and r derivatives of A
      do 7 i = 1,ngrid
        do 6 j = 1,ngrid
          if (i.eq.1) then
            dadr(i,j) = (a(2,j)-a(1,j))/dr
            dbdr(i,j) = (b(2,j)-b(1,j))/dr
            dsdr(i,j) = (s(2,j)-s(1,j))/dr
          else if (i.eq.ngrid) then
            dadr(i,j) = (a(ngrid,j)-a(ngrid-1,j))/dr
            dbdr(i,j) = (b(ngrid,j)-b(ngrid-1,j))/dr
            dsdr(i,j) = (s(ngrid,j)-s(ngrid-1,j))/dr
          else
            dadr(i,j) = (a(i+1,j)-a(i-1,j))/(2.d0*dr)
            dbdr(i,j) = (b(i+1,j)-b(i-1,j))/(2.d0*dr)
            dsdr(i,j) = (s(i+1,j)-s(i-1,j))/(2.d0*dr)
          endif

          if (j.eq.1) then
            dadt(i,j) = (a(i,2)-a(i,1))/dth
            dbdt(i,j) = (b(i,2)-b(i,1))/dth
            dsdt(i,j) = 0.d0
c           dsdt(i,j) = (s(i,2)-s(i,1))/dth
          else if (j.eq.ngrid) then
            dadt(i,j) = (a(i,ngrid)-a(i,ngrid-1))/dth
c            if (ipar.eq.0) then
c               dbdt(i,j) = 0.0d0
c            else
               dbdt(i,j) = (b(i,j)-b(i,j-1))/dth
c            endif
            dsdt(i,j) = 0.d0
c           dsdt(i,j) = (s(i,ngrid)-s(i,ngrid-1))/dth
          else
            dadt(i,j) = (a(i,j+1)-a(i,j-1))/(2.d0*dth)
            dbdt(i,j) = (b(i,j+1)-b(i,j-1))/(2.d0*dth)
            dsdt(i,j) = (s(i,j+1)-s(i,j-1))/(2.d0*dth)
          endif
    6   continue
    7 continue

c Sum the volume contributions to the free energy
      fvol  = 0.d0
      fsurf = 0.d0
      volfactor = 4.d0*pi*dth*dr
      surfactor = 2.d0*pi*dth
      do 10 i=2,ngrid
        ro=(i-1)*dr
        do 20 j=2,ngrid
          cell = 1.d0
          if (i.eq.ngrid) cell = cell*0.5d0
          if (j.eq.ngrid) cell = cell*0.5d0
          volfact = cell*volfactor*st(j)*ro**2

c Bulk order parameter contribution
          fbulk = s(i,j)**2*af/2.d0 - s(i,j)**3*bf/3.d0
     1     + s(i,j)**4*cf/4.d0 + 0.75d0*df*(dsdr(i,j)**2
     2     + dsdt(i,j)**2/ro**2)

c Elastic contribution
```

```
            ca1 = dcos(a(i,j))
            sa1 = dsin(a(i,j))
            sa2 = dsin(2.d0*a(i,j))
            cb1 = dcos(b(i,j))
            sb1 = dsin(b(i,j))
            sb2 = dsin(2.d0*b(i,j))
            cf1 = dcos(fdir(i,j))
            sf1 = dsin(fdir(i,j))

            splay = (   2.d0*ca1
     x                - ct(j)*cb1*sa1
     x                - dadr(i,j)*ro*sa1
     x                - dadt(i,j)*cb1*ca1
     x                + dbdt(i,j)*sb1*sa1
     x               )/ro
            twist = (  ct(j)*sa2*sb1/2.d0
     x                + dadt(i,j)*sb1
     x                + dbdr(i,j)*ro*sa1**2
     x                + dbdt(i,j)*sa2*cb1/2.d0
     x                )/ro
            bndr = (    sa1**2
     x                + dadr(i,j)*ro*sa2/2.d0
     x                - dadt(i,j)*sa1**2*cb1
     x                )/ro
            bndt = (    sa2*cb1/2.d0
     x                + ct(j)*sa1**2*sb1**2
     x                + dadr(i,j)*ro*ca1**2*cb1
     x                - dadt(i,j)*sa2*cb1**2/2.d0
     x                - dbdr(i,j)*ro*sa2*sb1/2.d0
     x                + dbdt(i,j)*sa1**2*sb2/2.d0
     x                )/ro
            bndp = (    ct(j)*sa1**2*sb2/2.d0
     x                - sa2*sb1/2.d0
     x                - dadr(i,j)*ro*ca1**2*sb1
     x                + dadt(i,j)*sa2*sb2/4.d0
     x                - dbdr(i,j)*ro*sa2*cb1/2.d0
     x                + dbdt(i,j)*sa1**2*cb1**2
     x                )/ro
            nscp1= ca1*dsdr(i,j)-sa1*cb1*dsdt(i,j)/ro
            nscp2= bndr*dsdr(i,j)+bndt*dsdt(i,j)/ro
            felast = 0.5d0*s(i,j)**2*(h11*splay**2 + h22*twist**2
     x             + h33*(bndr**2+ bndt**2+bndp**2))
            fcoupl =(3.d0/4.d0)*ef*(0.5d0*nscp1**2
     x              +2.d0*s(i,j)*splay*nscp1
     x              +s(i,j)*nscp2)

c Electric contribution
            felect = - fmag(i,j)**2*(ep + de*s(i,j)*
     x                (ca1*cf1+sa1*sf1*cb1)**2)/(8.d0*pi)

c Total volume contribution
            fvol = fvol + volfact*(fbulk+felast+fcoupl+felect)
   20     continue
   10   continue

c Surface contribution
        do 30 j=2,ngrid
          cell = 1.d0
          if (j.eq.ngrid) cell = 0.5d0
          surfact = cell*surfactor*st(j)*R**2

          ca1 = dcos(a(ngrid,j))
          sa2 = dsin(2.d0*a(ngrid,j))
          cb1 = dcos(b(ngrid,j))
          sb1 = dsin(b(ngrid,j))
```

```
         sdlsplyr = (   2.d0*ca1**2
     x                - .5d0*ct(j)*sa2*cb1
     x                - dadt(ngrid,j)*cb1
     x                + .5d0*dbdt(ngrid,j)*sa2*sb1
     x                )/R

         f24 = h24*sdlsplyr
         fsurf = fsurf - surfact*s(ngrid,j)*
     x          (w0*dcos(a(ngrid,j))**2+f24*s(ngrid,j))
   30 continue

c Total Free energy:
      ftotal = fvol + fsurf
      return
      end
c *********************************************************************
      subroutine dfunc(x,xi)
c Subroutine dfunc calculates the array dtot(i,j) that contains the
c derivatives of the free energy w/ respect to the node variables a(i,j).
c Dtot(i,j) is undefined for i=1 and for j=1 or ngrid (that is,
c a(i,j) is fixed at these locations).  It also calculates the elements
c of the unit vector xi, which points in the direction of maximum
c increase of the free energy (i.e., the direction of the gradient)
      implicit real*8(a-h,o-z)
      common/dropletparms/R,h11,h22,h33,h24,af,bf,cf,df,de,ep,w0,seq,ef
      common/simulparms/ngrid,npts,mm,nanneal,xlim,klim,dr,dth,pi,ipar,
     1 ct(20),st(20)
      common/field/fmag(20,20),fdir(20,20)
      dimension a(20,20),b(20,20),s(20,20)
     1,dtota(20,20),dtotb(20,20),dtots(20,20)
     1,dadt(20,20),dadr(20,20),dbdt(20,20),dbdr(20,20)
     1,dsdt(20,20),dsdr(20,20),xi(1200),x(1200)


c Zero the array of partial derivatives; restore A, B, and S arrays from X
      do 2 j = 1,ngrid
        do 1 i = 1,ngrid
          dtota(i,j) = 0.d0
          dtotb(i,j) = 0.d0
          dtots(i,j) = 0.d0
          a(i,j) = x((i-1)*ngrid+j          )
          b(i,j) = x((i-1)*ngrid+j+ngrid**2)
          s(i,j) = x((i-1)*ngrid+j+2*ngrid**2)
    1   continue
    2 continue

c Calculate theta and r derivatives of A, B, and S
      do 7 i = 1,ngrid
        do 6 j = 1,ngrid
          if (i.eq.1) then
            dadr(i,j) = (a(2,j)-a(1,j))/dr
            dbdr(i,j) = (b(2,j)-b(1,j))/dr
            dsdr(i,j) = (s(2,j)-s(1,j))/dr
          else if (i.eq.ngrid) then
            dadr(i,j) = (a(ngrid,j)-a(ngrid-1,j))/dr
            dbdr(i,j) = (b(ngrid,j)-b(ngrid-1,j))/dr
            dsdr(i,j) = (s(ngrid,j)-s(ngrid-1,j))/dr
          else
            dadr(i,j) = (a(i+1,j)-a(i-1,j))/(2.d0*dr)
            dbdr(i,j) = (b(i+1,j)-b(i-1,j))/(2.d0*dr)
            dsdr(i,j) = (s(i+1,j)-s(i-1,j))/(2.d0*dr)
          endif

          if (j.eq.1) then
            dadt(i,j) = (a(i,2)-a(i,1))/dth
```

```
            dbdt(i,j) = (b(i,2)-b(i,1))/dth
            dsdt(i,j) = 0.d0
c           dsdt(i,j) = (s(i,2)-s(i,1))/dth
          else if (j.eq.ngrid) then
            dadt(i,j) = (a(i,ngrid)-a(i,ngrid-1))/dth
c            if (ipar.eq.0) then
c               dbdt(i,j) = 0.0d0
c            else
              dbdt(i,j) = (b(i,j)-b(i,j-1))/dth
c            endif
            dsdt(i,j) = 0.d0
c           dsdt(i,j) = (s(i,ngrid)-s(i,ngrid-1))/dth
          else
            dadt(i,j) = (a(i,j+1)-a(i,j-1))/(2.d0*dth)
            dbdt(i,j) = (b(i,j+1)-b(i,j-1))/(2.d0*dth)
            dsdt(i,j) = (s(i,j+1)-s(i,j-1))/(2.d0*dth)
          endif
    6   continue
    7 continue

c Calculate derivatives of total free energy with respect to
c variable A, B, and S at each node (i.e., the components of the generalized
c gradient).  Omit terms at i=0 and at j=0 (the volume factor will be
c zero in each of these cases)

      volfactor = 4.d0*pi*dth*dr
      surfactor = 2.d0*pi*dth

      do 200 i=2,ngrid
        ro = (i-1)*dr
        do 195 j=2,ngrid
          cell = 1.d0
          if (i.eq.ngrid) cell = cell*0.5d0
          if (j.eq.ngrid) cell = cell*0.5d0
          volfact = cell*volfactor*st(j)*ro**2
          surfact = 2.d0*cell*surfactor*st(j)*R**2

c Bulk order parameter contribution
          dsb =  af*s(i,j) - bf*s(i,j)**2 + cf*s(i,j)**3
          dsbr = 1.5d0*df*dsdr(i,j)/(2.d0*dr)
          dsbt = 1.5d0*df*dsdt(i,j)/(2.d0*dth*ro**2)

c Elastic contribution
          ca1 = dcos(a(i,j))
          sa1 = dsin(a(i,j))
          sa2 = dsin(2.d0*a(i,j))
          ca2 = dsin(2.d0*a(i,j))

          cb1 = dcos(b(i,j))
          sb1 = dsin(b(i,j))
          cb2 = dcos(2.d0*b(i,j))
          sb2 = dsin(2.d0*b(i,j))

          cf1 = dcos(fdir(i,j))
          sf1 = dsin(fdir(i,j))

          splay = (   2.d0*ca1
     x              - ct(j)*cb1*sa1
     x              - dadr(i,j)*ro*sa1
     x              - dadt(i,j)*cb1*ca1
     x              + dbdt(i,j)*sb1*sa1
     x             )/ro
          twist = (  ct(j)*sa2*sb1/2.d0
     x             + dadt(i,j)*sb1
     x             + dbdr(i,j)*ro*sa1**2
     x             + dbdt(i,j)*sa2*cb1/2.d0
```

```
     x             )/ro
           bndr = (   sa1**2
     x              + dadr(i,j)*ro*sa2/2.d0
     x              - dadt(i,j)*sa1**2*cb1
     x            )/ro
           bndt = (   sa2*cb1/2.d0
     x             + ct(j)*sa1**2*sb1**2
     x             + dadr(i,j)*ro*ca1**2*cb1
     x             - dadt(i,j)*sa2*cb1**2/2.d0
     x             - dbdr(i,j)*ro*sa2*sb1/2.d0
     x             + dbdt(i,j)*sa1**2*sb2/2.d0
     x            )/ro
           bndp = (   ct(j)*sa1**2*sb2/2.d0
     x             - sa2*sb1/2.d0
     x             - dadr(i,j)*ro*ca1**2*sb1
     x             + dadt(i,j)*sa2*sb2/4.d0
     x             - dbdr(i,j)*ro*sa2*cb1/2.d0
     x             + dbdt(i,j)*sa1**2*cb1**2
     x             )/ro

           dasplay =( - 2.d0*sa1
     x                - ct(j)*cb1*ca1
     x                - dadr(i,j)*ro*ca1
     x                + dadt(i,j)*cb1*sa1
     x                + dbdt(i,j)*sb1*ca1
     x               )/ro
           dasplayr = - sa1/(2.d0*dr)
           dasplayt = - ca1*cb1/(2.d0*dth*ro)

           dbsplay  = ( ct(j)*sa1*sb1
     x                + dadt(i,j)*ca1*sb1
     x                + dbdt(i,j)*sa1*cb1
     x               )/ro
           dbsplayr =   0.d0
           dbsplayt =   sa1*sb1/(2.d0*dth*ro)

           datwist = (  ct(j)*ca2*sb1
     x                + dbdr(i,j)*ro*sa2
     x                + dbdt(i,j)*ca2*cb1
     x               )/ro
          datwistr = 0.d0
          datwistt = sb1/(2.d0*dth*ro)
          dbtwist = (  ct(j)*sa2*cb1/2.d0
     x                + dadt(i,j)*cb1
     x                - dbdt(i,j)*sa2*sb1/2.d0
     x               )/ro
          dbtwistr = sa1**2/(2.d0*dr)
          dbtwistt = sa2*cb1/(4.d0*dth*ro)

          dabndr  = (sa2
     x               + dadr(i,j)*ro*ca2
     x               - dadt(i,j)*sa2*cb1
     x             )/ro
          dabndrr =    sa2/(4.d0*dr)
          dabndrt = - sa1**2*cb1/(2.d0*dth*ro)
          dbbndr  =   dadt(i,j)*sa1**2*sb1/ro
          dbbndrr =   0.d0
          dbbndrt =   0.d0

          dabndt = ( ca2*cb1
     x              + ct(j)*sa2*sb1**2
     x              - dadr(i,j)*ro*sa2*cb1
     x              - dadt(i,j)*ca2*cb1**2
     x              - dbdr(i,j)*ro*ca2*sb1
     x              + dbdt(i,j)*sa2*sb2/2.d0
     x             )/ro
```

```
      dabndtr =  ca1**2*cb1/(2.d0*dr)
      dabndtt = -sa2*cb1**2/(4.d0*dth*ro)
      dbbndt =(- sa2*sb1/2.d0
     x          + ct(j)*sa1**2*sb2
     x          - dadr(i,j)*ro*ca1**2*sb1
     x          + dadt(i,j)*sa2*sb2/2.d0
     x          - dbdr(i,j)*ro*sa2*cb1/2.d0
     x          + dbdt(i,j)*sa1**2*cb2
     x         )/ro
      dbbndtr = -sa2*sb1/(4.d0*dr)
      dbbndtt = -sa1**2*sb2/(4.d0*dth*ro)

      dabndp = ( ct(j)*sa2*sb2/2.d0
     x          - ca2*sb1
     x          + dadr(i,j)*ro*sa2*sb1
     x          + dadt(i,j)*ca2*sb2/2.d0
     x          - dbdr(i,j)*ro*ca2*cb1
     x          + dbdt(i,j)*sa2*cb1**2
     x         )/ro
      dabndpr = - ca1**2*sb1/(2.d0*dr)
      dabndpt =   sa2*sb2/(8.d0*dth*ro)
      dbbndp = (  ct(j)*sa1**2*cb2
     x          - sa2*cb1/2.d0
     x          - dadr(i,j)*ro*ca1**2*cb1
     x          + dadt(i,j)*sa2*cb2/2.d0
     x          + dbdr(i,j)*ro*sa2*sb1/2.d0
     x          - dbdt(i,j)*sa1**2*sb2
     x         )/ro
      dbbndpr = - sa2*cb1/(4.d0*dr)
      dbbndpt =   sa1**2*cb1**2/(2.d0*dth*ro)

      nscp1= ca1*dsdr(i,j)-sa1*cb1*dsdt(i,j)/ro
      danscp1= -(sa1*dsdr(i,j)+ca1*sb1*dsdt(i,j)/ro)
      dbnscp1= sa1*sb1*dsdt(i,j)/ro
      dsnscp1r= ca1/(2.d0*dr)
      dsnscp1t= -sa1*cb1/(2.d0*dth*ro)

      nscp2= bndr*dsdr(i,j)+bndt*dsdt(i,j)/ro
      danscp2= dabndr*dsdr(i,j)+dabndt*dsdt(i,j)/ro
      dbnscp2= dbbndr*dsdr(i,j)+dbbndt*dsdt(i,j)/ro
      danscp2r=dabndrr*dsdr(i,j)+dabndtr*dsdt(i,j)/ro
      dapscp2t=dabndrt*dsdr(i,j)+dabndtt*dsdt(i,j)/ro
      dbnscp2r=dbbndrr*dsdr(i,j)+dbbndtr*dsdt(i,j)/ro
      dbnscp2t=dbbndrt*dsdr(i,j)+dbbndtt*dsdt(i,j)/ro
      dsnscp2r= bndr/(2.d0*dr)
      dsnscp2t= bndt/(2.d0*dth*ro)

      daelast = s(i,j)**2*(h11*splay*dasplay +  h22*twist*datwist +
     x            h33*(bndr*dabndr +  bndt*dabndt +  bndp*dabndp))
      daelastr = s(i,j)**2*(h11*splay*dasplayr + h22*twist*datwistr +
     x            h33*(bndr*dabndrr + bndt*dabndtr + bndp*dabndpr))
      daelastt = s(i,j)**2*(h11*splay*dasplayt + h22*twist*datwistt +
     x            h33*(bndr*dabndrt + bndt*dabndtt + bndp*dabndpt))
      dbelast  = s(i,j)**2*(h11*splay*dbsplay + h22*twist*dbtwist +
     x            h33*(bndr*dbbndr +  bndt*dbbndt +  bndp*dbbndp))
      dbelastr = s(i,j)**2*(h11*splay*dbsplayr + h22*twist*dbtwistr +
     x            h33*(bndr*dbbndrr + bndt*dbbndtr + bndp*dbbndpr))
      dbelastt = s(i,j)**2*(h11*splay*dbsplayt + h22*twist*dbtwistt +
     x            h33*(bndr*dbbndrt + bndt*dbbndtt + bndp*dbbndpt))
      dselast = s(i,j)*(h11*splay**2 + h22*twist**2
     x          + h33*(bndr**2+ bndt**2+bndp**2))
c     fcoupl = (3.d0/4.d0)*ef*(0.5d0*nscp1**2
c               +2.d0*s(i,j)*splay*nscp1
c               +s(i,j)*nscp2)
      dacoupl = (3.d0/4.d0)*ef*(nscp1*danscp1
     x            + 2.d0*s(i,j)*(dasplay*nscp1+ splay*danscp1)
```

```
     x              + s(i,j)*danscp2)
          dbcoupl = (3.d0/4.d0)*ef*(nscp1*dbnscp1
     x              + 2.d0*s(i,j)*(dbsplay*nscp1+ splay*dbnscp1)
     x              + s(i,j)*dbnscp2)
          dacouplr = (3.d0/4.d0)*ef*(2.d0*s(i,j)*dasplayr*nscp1
     x               + s(i,j)*danscp2r)
          dbcouplr = (3.d0/4.d0)*ef*(2.d0*s(i,j)*dbsplayr*nscp1
     x               + s(i,j)*dbnscp2r)
          dacouplt = (3.d0/4.d0)*ef*(2.d0*s(i,j)*dasplayt*nscp1
     x               + s(i,j)*danscp2t)
          dbcouplt = (3.d0/4.d0)*ef*(2.d0*s(i,j)*dbsplayt*nscp1
     x               + s(i,j)*dbnscp2t)
          dscouplr = (3.d0/4.d0)*ef*(dsnscp1r*nscp1
     x               + 2.d0*s(i,j)*(dssplayr*nscp1+splay*dsnscp1r)
     x               + s(i,j)*dsnscp2r)
          dscouplt = (3.d0/4.d0)*ef*(dsnscp1t*nscp1
     x               + 2.d0*s(i,j)*(dssplayt*nscp1+splay*dsnscp1t)
     x               + s(i,j)*dsnscp2t)

c Electric contribution
c         felect = - fmag(i,j)**2*(ep + de*s(i,j)*
c     x             (ca1*cf1+sa1*sf1*cb1)**2)/(8.d0*pi)
          dselect = - fmag(i,j)**2*de*(ca1*cf1+sa1*sf1*cb1)**2
     x              /(8.d0*pi)
          daelect = - fmag(i,j)**2*de*s(i,j)
     x              *2.d0*(-sa1*cf1+ca1*sf1*cb1)*
     x              (ca1*cf1+sa1*sf1*cb1)/(8.d0*pi)
          dbelect = + fmag(i,j)**2*de*s(i,j)*sa1*sf1*sb1*2.d0*
     x              (ca1*cf1+sa1*sf1*cb1)/(8.d0*pi)

c Surface contribution
          if (i.eq.ngrid) then
          sdlsplyr = ( 2.d0*ca1**2
     x               - .5d0*ct(j)*sa2*cb1
     x               - dadt(ngrid,j)*cb1
     x               + .5d0*dbdt(ngrid,j)*sa2*sb1
     x               )/R
          dasdlsplyr = ( - 2.d0*sa2
     x                 + ct(j)*ca2*cb1
     x                 + dbdt(ngrid,j)*ca2*sb1
     x                 )/R
          dasdlsplyrr = 0.d0
          dasdlsplyrt = - cb1/(2.d0*dth*R)
          dbsdlsplyr  = ( .5d0*ct(j)*sa2*sb1
     x                  + dadt(ngrid,j)*sb1
     x                  + .5d0*dbdt(ngrid,j)*sa2*cb1
     x                  )/R
          dbsdlsplyrr = 0.d0
          dbsdlsplyrt = sa2*sb1/(4.d0*dth*R)

          dasurf  = s(ngrid,j)*(- h24*s(ngrid,j)*dasdlsplyr
     x                + w0*dsin(2.d0*a(ngrid,j)))
          dasurfr = - h24*dasdlsplyrr*s(ngrid,j)**2
          dasurft = - h24*dasdlsplyrt*s(ngrid,j)**2
          dbsurf  = - h24*dbsdlsplyr*s(ngrid,j)**2
          dbsurfr = - h24*dbsdlsplyrr*s(ngrid,j)**2
          dbsurft = - h24*dbsdlsplyrt*s(ngrid,j)**2
          dssurf  = - (h24*s(ngrid,j)*sdlsply+
     x                 w0*dcos(a(ngrid,j))**2)
        endif

c Sum contributions to a derivatives
          da = volfact*(daelast+daelect+dacoupl) + surfact*dasurf
          dar = volfact*(daelastr+dacouplr) + surfact*dasurfr
          dat = volfact*(daelastt+dacouplt) + surfact*dasurft
          dtota(i,j) = dtota(i,j) + da
```

```
            if (i.lt.ngrid) then
               dtota(i+1,j) = dtota(i+1,j) + dar
               dtota(i-1,j) = dtota(i-1,j) - dar
            else
               dtota(i  ,j) = dtota(i  ,j) + 2.d0*dar
               dtota(i-1,j) = dtota(i-1,j) - 2.d0*dar
            endif
            if (j.lt.ngrid) then
               dtota(i,j+1) = dtota(i,j+1) + dat
               dtota(i,j-1) = dtota(i,j-1) - dat
            else
               dtota(i,j  ) = dtota(i,j  ) + 2.d0*dat
               dtota(i,j-1) = dtota(i,j-1) - 2.d0*dat
            endif

c Sum contributions to b derivatives
            db  = volfact*(dbelast + dbelect) + surfact*dbsurf
            dbr = volfact*dbelastr + surfact*dbsurfr
            dbt = volfact*dbelastt + surfact*dbsurft
            dtotb(i,j) = dtotb(i,j) + db
            if (i.ne.ngrid) then
              dtotb(i+1,j) = dtotb(i+1,j) + dbr
              dtotb(i-1,j) = dtotb(i-1,j) - dbr
            else
              dtotb(i  ,j) = dtotb(i  ,j) + 2.d0*dbr
              dtotb(i-1,j) = dtotb(i-1,j) - 2.d0*dbr
            endif
            if (j.ne.ngrid) then
              dtotb(i,j+1) = dtotb(i,j+1) + dbt
              dtotb(i,j-1) = dtotb(i,j-1) - dbt
            else
              dtotb(i,j  ) = dtotb(i,j  ) + 2.d0*dbt
              dtotb(i,j-1) = dtotb(i,j-1) - 2.d0*dbt
            endif

c Sum contributions to s derivatives
            ds = volfact*(dsb + dselast + dscoupl + dselect)
     x           + surfact*dssurf
            dsr = volfact*(dsbr + dscouplr)
            dst = volfact*(dsbt + dscouplt)
            dtots(i,j) = dtots(i,j) + ds
            if (i.ne.ngrid) then
              dtots(i+1,j) = dtots(i+1,j) + dsr
              dtots(i-1,j) = dtots(i-1,j) - dsr
            else
              dtots(i  ,j) = dtots(i  ,j) + 2.d0*dsr
              dtots(i-1,j) = dtots(i-1,j) - 2.d0*dsr
            endif
            if (j.ne.ngrid) then
              dtots(i,j+1) = dtots(i,j+1) + dst
              dtots(i,j-1) = dtots(i,j-1) - dst
            else
              dtots(i,j  ) = dtots(i,j  ) + 2.d0*dst
              dtots(i,j-1) = dtots(i,j-1) - 2.d0*dst
            endif

  195   continue
  200 continue

c Ensure A remains at zero on the axis, and is either zero or pi/2
c on the equator, by zeroing the derivative.
      do 210 i=1,ngrid
        dtota(i,1)     = 0.d0
        dtota(i,ngrid) = 0.d0
        dtota(1,i)     = 0.d0
  210 continue
```

```
c Store elements of gradient in array XI
      do 220 i=1,ngrid
        do 215 j=1,ngrid
          xi((i-1)*ngrid+j          ) = dtota(i,j)
          xi((i-1)*ngrid+j+ngrid**2) = dtotb(i,j)
          xi((i-1)*ngrid+j+2*ngrid**2) = dtots(i,j)
  215   continue
  220 continue

      return
      end

c *********************************************************************
      subroutine frpmn(a,b,s,ftol,iter,fret)
c (Numerical Recipes, p 305)
c Polak-Ribiere variant of conjugate gradient minimization
c Given a starting point P(a,b,s) that is a vector of length
c npts(=ngrid x ngrid), Polak-Ribiere minimization is performed
c on a function TOTAL, using its gradient as calculated by
c a routine DFUNC.  The convergence tolerance on the function value
c is input as FTOL.  Returned quantities are
c P(a,b,s)(the location of minimum),ITER(the no. of iterations that were
c performed), and FRET(the minimum value of the function).
c The routine LINMIN is called to perform line minimization.
      implicit real*8(a-h,o-z)
      common/dropletparms/R,h11,h22,h33,h24,af,bf,cf,df,de,ep,w0,seq,ef
      common/simulparms/ngrid,npts,mm,nanneal,xlim,klim,dr,dth,pi,ipar,
     1ct(20),st(20)
      common/field/fmag(20,20),fdir(20,20)
      parameter (itmax = 200, eps = 1.d-10)
      dimension a(20,20),b(20,20),s(20,20)
     1,p(1200),g(1200),h(1200),xi(1200)

c Calculate the elements of vector p from the array a(i,j), b(i,j), and s(i,j)
      do 5 i=1,ngrid
        do 4 j=1,ngrid
          p((i-1)*ngrid+j          )   = a(i,j)
          p((i-1)*ngrid+j+ngrid**2)   = b(i,j)
          p((i-1)*ngrid+j+2*ngrid**2) = s(i,j)
    4   continue
    5 continue

      call total(p,fp)
      call dfunc(p,xi)

      do 11 j=1,npts
        g(j) = -xi(j)
        h(j) = g(j)
        xi(j) = h(j)
   11 continue

      do 14 its=1,itmax
        iter=its
        call linmin(p,xi,fret)
        if (2.d0*dabs(fret-fp).le.ftol*(dabs(fret)+dabs(fp)+eps))goto 17
        call total(p,fp)
        call dfunc(p,xi)
        gg=0.d0
        dgg=0.d0
        do 12 j=1,npts
          gg = gg + g(j)**2
          dgg = dgg + (xi(j)+g(j))*xi(j)
   12   continue
        if (gg.eq.0.d0) return
        gam = dgg/gg
```

```
        do 13 j=1,npts
          g(j) = -xi(j)
          h(j) = g(j) + gam*h(j)
          xi(j) = h(j)
   13   continue
   14 continue
      pause 'fpr maximum iterations exceeded'

   17 continue
c Calculate the elements of the array a(i,j) from the vector p
      do 20 i=1,ngrid
        do 19 j=1,ngrid
          a(i,j) = p((i-1)*ngrid+j)
          b(i,j) = p((i-1)*ngrid+j+ngrid**2)
          s(i,j) = p((i-1)*ngrid+j+2*ngrid**2)
   19   continue
   20 continue

      return
      end
c *********************************************************************
      subroutine linmin(p,xi,fret)
c (Numerical Recipes, p 300)
c Given an npts(=ngrid x ngrid) dimensional point P and
c npts(=ngrid x ngrid) dimensional XI, moves and resets P to
c where the function TOTAL(P) takes on a minimum along
c the direction XI from P, and replace XI by the actual
c vector displacement that P was moved.  Also returns as
c FRET the value of TOTAL at the returned location P.
c This is actually all accomplished by calling the
c routines mnbrak and dbrent.
      implicit real*8(a-h,o-z)
      parameter (tol=1.d-7)
      common/dropletparms/R,h11,h22,h33,h24,af,bf,cf,df,de,ep,w0,seq,ef
      common/simulparms/ngrid,npts,mm,nanneal,xlim,klim,dr,dth,pi,ipar,
     1ct(20),st(20)
      common/field/fmag(20,20),fdir(20,20)
      common/f1com/ncom,pcom(1200),xicom(1200)
      dimension xi(1200),p(1200)
      ncom = npts

c Establish magnitude of gradient; if less than 1.d-18, quit
      xnorm = 0.d0
      do 3 j=1,npts
        xnorm = xnorm + xi(j)**2
    3 continue
      xnorm = dsqrt(xnorm)
      if (xnorm.lt.1.d-18) return

c Establish maximum step size so no angles are greater than pi/2
c or less than -pi/2, and order parameter is always between 0 and 1
      pi1 =   pi/2.d0 + 1.d-4
      xmax = 1.d18
      np = npts/3
      do 8 i = 1,np
      if (dabs(xi(i)).gt.1.d-18) then
        if (xi(i).gt.0) then
           xxm = ( pi1-p(i))/xi(i)
        else
           xxm = (-pi1-p(i))/xi(i)
        endif
        xmax = min(xxm,xmax)
      endif
      pcom(i) = p(i)
      xicom(i) = xi(i)
    8 continue
```

```
        do 9 i = np+1, npts
        if (dabs(xi(i)).gt.1.d-18) then
          if (xi(i).gt.0) then
             xxm = ( 1.d0-p(i))/xi(i)
          else
             xxm = -p(i)/xi(i)
          endif
          xmax = min(xxm,xmax)
        endif
        pcom(i) = p(i)
        xicom(i) = xi(i)
      9 continue

        xx = min(xmax/5.d0,1.0d0/xnorm)
        ax = 0.d0
        call mnbrak(ax,xx,bx,fa,fx,fb)
        fret = dbrent(ax,xx,bx,tol,xmin)

        do 13 j=1,npts
          p(j) = p(j) + xmin*xi(j)
     13 continue

        return
        end
c ***********************************************************************
        subroutine mnbrak(ax,bx,cx,fa,fb,fc)
c (Numerical Recipes, p 281)
c Given distinct initial points AX and BX, this routine searches
c in the downhill direction (defined by the function as evaluated
c at the initial points) and returns new points AX, BX, CX which
c bracket a minimum of the function. Also returned are the function
c values at the three points, FA, FB, FC.
        implicit real*8(a-h,o-z)
        common/f1com/ncom,pcom(1200),xicom(1200)
        parameter (gold = 1.618034d0, glimit = 100.d0, tiny = 1.d-20)
        call f1dim(ax,fa)
        call f1dim(bx,fb)
c Switch a and b so that we can go downhill in the direction
c from a to b:
        if (fb.gt.fa) then
          dum = ax
          ax = bx
          bx = dum
          dum = fa
          fa = fb
          fb = dum
        endif
c First guess for c:
        cx = bx+gold*(bx-ax)
        call f1dim(cx,fc)
c Keep returning here until we bracket.
      1 if (fb.ge.fc) then
          r = (bx-ax)*(fb-fc)
          q = (bx-cx)*(fb-fa)
c Compute U by parabolic extrapolation from a,b,c and tiny is used to
c prevent any possible division by zero:
          u = bx - ((bx-cx)*q - (bx-ax)*r)/
     x                 (2.d0*sign(max(dabs(q-r),tiny),(q-r)))
c We won't go farther than this:
          ulim = bx + glimit*(cx-bx)
c U is between b and c:
          if ((bx-u)*(u-cx).gt.0.d0) then
            call f1dim(u,fu)
c Got a minimum between b and c:
            if (fu.lt.fc) then
              ax = bx
```

```
              fa = fb
              bx = u
              fb = fu
              return
cGot a minimum between a and u:
            else if (fu.gt.fb) then
              cx = u
              fc = fu
              return
            endif
c Extend u beyond cx
            u = cx + gold*(cx-bx)
            call f1dim(u,fu)
          else if ((cx-u)*(u-ulim).gt.0.d0) then
c  u lies between cx and ulim
            call f1dim(u,fu)
            if (fu.lt.fc) then
c  Minimum is bracketed
              bx = cx
              cx = u
              u = cx + gold*(cx-bx)
              fb = fc
              fc = fu
              call f1dim(u,fu)
            endif
          else if ((u-ulim)*(ulim-cx).ge.0.d0) then
            u = ulim
            call f1dim(u,fu)
          else
            u = cx + gold*(cx-bx)
            call f1dim(u,fu)
          endif
c Replace ax by bx, bx by cx, cx by u and go back to 1
          ax = bx
          bx = cx
          cx = u
          fa = fb
          fb = fc
          fc = fu
          goto 1
        endif

        return
        end
c ***********************************************************************
        function dbrent(ax,bx,cx,tol,xmin)
        implicit real*8(a-h,o-z)
        common/f1com/ncom,pcom(1200),xicom(1200)
        parameter(itmax=100,zeps=1.d-10)
        logical ok1,ok2
        a = min(ax,cx)
        b = max(ax,cx)
        v = bx
        w = v
        x = v
        e = 0.d0
        call f1dim(x,fx)
        fv = fx
        fw = fx
        call df1dim(x,dx)
        dv = dx
        dw = dx
        do 11 iter = 1,itmax
          xm = 0.5d0*(a+b)
          tol1 = tol*dabs(x) + zeps
          tol2 = 2.d0*tol1
```

```
      if (dabs(x-xm).le.(tol2-0.5d0*(b-a))) goto 3
      if (dabs(e).gt.tol1) then
        d1 = 2.d0*(b-a)
        d2 = d1
        if (dw.ne.dx) d1 = (w-x)*dx/(dx-dw)
        if (dv.ne.dx) d2 = (v-x)*dx/(dx-dv)
        u1 = x + d1
        u2 = x + d2
        ok1 = ((a-u1)*(u1-b).gt.0.d0).and.(dx*d1.le.0.d0)
        ok2 = ((a-u2)*(u2-b).gt.0.d0).and.(dx*d2.le.0.d0)
        olde = e
        e = d
        if (.not.(ok1.or.ok2)) then
          goto 1
        else if (ok1.and.ok2) then
          if (dabs(d1).lt.dabs(d2)) then
            d = d1
          else
            d = d2
          endif
        else if (ok1) then
          d = d1
        else
          d = d2
        endif
        if (dabs(d).gt.dabs(0.5d0*olde)) goto 1
        u = x + d
        if (u-a.lt.tol2 .or. b-u.lt.tol2) d = sign(tol1,xm-x)
             goto 2
      endif
1     if (dx.ge.0.d0) then
        e = a - x
      else
        e = b - x
      endif
      d = 0.5d0*e
2     if (dabs(d).ge.tol1) then
        u = x + d
        call f1dim(u,fu)
      else
        u = x + sign(tol1,d)
        call f1dim(u,fu)
        if (fu.gt.fx) goto 3
      endif
      call df1dim(u,du)
      if (fu.le.fx) then
        if (u.ge.x) then
          a = x
        else
          b = x
        endif
        v = w
        fv = fw
        dv = dw
        w = x
        fw = fx
        dw = dx
        x = u
        fx = fu
        dx = du
      else
        if (u.lt.x) then
          a = u
        else
          b = u
        endif
```

```
          if (fu.le.fw .or. w.eq.x) then
            v = w
            fv = fw
            dv = dw
            w = u
            fw = fu
            dw = du
          else if (fu.le.fv .or. v.eq.x .or. v.eq.w) then
            v = u
            fv = fu
            dv = du
          endif
        endif
   11 continue
      pause 'dbrent exceeded maximum iterations'
    3 xmin = x
      dbrent = fx
      return
      end
c *********************************************************************
      subroutine f1dim(x,f1)
      implicit real*8(a-h,o-z)
      common/f1com/ncom,pcom(1200),xicom(1200)
      dimension xt(1200)
      do 11 j=1,ncom
        xt(j) = pcom(j) + x*xicom(j)
   11 continue
      call total(xt,f1)
      return
      end
c *********************************************************************
      subroutine df1dim(x,df1)
      implicit real*8(a-h,o-z)
      common/f1com/ncom,pcom(1200),xicom(1200)
      dimension xt(1200),df(1200)
      do 11 j = 1,ncom
        xt(j) = pcom(j) + x*xicom(j)
   11 continue
      call dfunc(xt,df)
      df1 = 0.d0
      do 12 j=1,ncom
        df1=df1 + df(j)*xicom(j)
   12 continue
      return
      end
c *********************************************************************
c  The quantities p and pp are, resp., the radial and tangential (theta)
c components of the electric field, times r, at the site (i,j)
      subroutine psum(p,pp,dr,i,x,amom)
      implicit real*8(a-h,o-z)
      dimension amom(4)
      nn=4
      p=0.d0
      pp=0.d0
      ro = dr*(i-1)
      do 10 l=1,nn
        p  = p-l*amom(l)*(ro**(l-1))*pleg(l,x)
        pp = pp+amom(l)*(ro**(l-1))*ppleg(l,x)*dsqrt(1.d0-x**2)
   10 continue
      return
      end
c *********************************************************************
      subroutine surface(a,b,s,amom,ep,de,r,b1)
      implicit real*8(a-h,o-z)
      common/simulparms/ngrid,npts,mm,nanneal,xlim,klim,dr,dth,pi,ipar,
     1ct(20),st(20)
```

```
      dimension a(20,20),b(20,20),s(20,20),
     1fcof(0:5),bcof(0:5),scof(0:5),
     1amom(4),xj(4,4),xjinv(4,4)

      call fita(a,fcof)
      call fitb(b,bcof)
      call fits(s,scof)
      call match(ipar,ep,de,fcof,bcof,scof,xj,r)
c Invert matrix
      call matinv(xj,xjinv,4,4)
c Calculate multipole moment coefficients
      do 10 j=1,4
        amom(j) = xjinv(j,1)*(-4.d0*b1/3.d0)
   10 continue
      return
      end
c ***********************************************************************
      subroutine fita(a,fcof)
      implicit real*8(a-h,o-z)
      common/simulparms/ngrid,npts,mm,nanneal,xlim,klim,dr,dth,pi,ipar,
     1ct(20),st(20)
      dimension a(20,20),fcof(0:5),pmat(5,5),pinv(5,5),q(5),x(20)
c Initialize arrays, including the cosine(theta) array, here called x(i)
      do 20 j=1,5
        q(j) = 0.0d0
        do 18 k=1,5
          pmat(j,k) = 0.d0
   18   continue
   20 continue
      do 24 i=1,ngrid
        x(i)=dcos((i-1)*dth)
  24  continue

c Compute the elements of the data vector q and the fitting matrix pmat
c ipar = 0 if f is even, 1 if f is odd
      do 40 i=1,ngrid
        dat = dcos(a(ngrid,i))
        y = x(i)
        fact = pleg(ipar,y)
        do 38 j=1,5
          q(j) = q(j) + (dat-fact)*(pleg(2*j+ipar,y)-fact)
          do 36 k=1,5
            pmat(j,k) = pmat(j,k) + (pleg(2*j+ipar,y)-fact)*
     1                  (pleg(2*k+ipar,y)-fact)
   36     continue
   38   continue
   40 continue

c Invert the fitting matrix pmat
      call matinv(pmat,pinv,5,5)

c Calculate the coefficients fcof, including the zeroth
      fcof(0) = 1.d0
      do 50 j=1,5
        fcof(j) = 0.d0
        do 48 k=1,5
          fcof(j) = fcof(j) + pinv(j,k)*q(k)
   48   continue
        fcof(0) = fcof(0) - fcof(j)
   50 continue

      return
      end

c ***********************************************************************
      subroutine fitb(b,bcof)
```

```
      implicit real*8(a-h,o-z)
      common/simulparms/ngrid,npts,mm,nanneal,xlim,klim,dr,dth,pi,ipar,
     1ct(20),st(20)
      dimension b(20,20),bcof(0:5),pmat(5,5),pinv(5,5),q(5),x(20)
c Initialize arrays, including the cosine(theta) array, here called x(i)
      do 20 j=1,5
        q(j) = 0.0d0
        do 18 k=1,5
          pmat(j,k) = 0.d0
   18   continue
   20 continue
      do 24 i=1,ngrid
        x(i)=dcos((i-1)*dth)
  24  continue

c Compute the elements of the data vector q and the fitting matrix pmat
c ipar = 0 if f is even, 1 if f is odd

      do 40 i=1,ngrid
        dat = dcos(b(ngrid,i))
        y = x(i)
        fact = pleg(0,y)
        do 38 j=1,5
          q(j) = q(j) + (dat-fact)*(pleg(2*j,y)-fact)
          do 36 k=1,5
            pmat(j,k) = pmat(j,k) + (pleg(2*j,y)-fact)*
     1                  (pleg(2*k,y)-fact)
   36     continue
   38   continue
   40 continue

c Invert the fitting matrix pmat
      call matinv(pmat,pinv,5,5)

c Calculate the coefficients bcof, including the zeroth
      bcof(0) = 1.d0
      do 50 j=1,5
        bcof(j) = 0.d0
        do 48 k=1,5
          bcof(j) = bcof(j) + pinv(j,k)*q(k)
   48   continue
        bcof(0) = bcof(0) - bcof(j)
   50 continue

      return
      end
c**********************************************************************
      subroutine fits(s,scof)
      implicit real*8(a-h,o-z)
      common/simulparms/ngrid,npts,mm,nanneal,xlim,klim,dr,dth,pi,ipar,
     1ct(20),st(20)
      dimension s(20,20),scof(0:5),pmat(5,5),pinv(5,5),q(5),x(20)
c Initialize arrays, including the cosine(theta) array, here called x(i)
      do 20 j=1,5
        q(j) = 0.0d0
        do 18 k=1,5
          pmat(j,k) = 0.d0
   18   continue
   20 continue

      do 24 i=1,ngrid
        x(i)=dcos((i-1)*dth)
  24  continue

c Compute the elements of the data vector q and the fitting matrix pmat
c Note that s is even in x.
```

```
      do 40 i=1,ngrid
        dat = s(ngrid,i)
        y = x(i)
        fact = pleg(0,y)
        do 38 j=1,5
          q(j) = q(j) + (dat-fact)*(pleg(2*j,y)-fact)
          do 36 k=1,5
            pmat(j,k) = pmat(j,k) + (pleg(2*j,y)-fact)*
     1                  (pleg(2*k,y)-fact)
   36     continue
   38   continue
   40 continue

c Invert the fitting matrix pmat
      call matinv(pmat,pinv,5,5)

c Calculate the coefficients scof, including the zeroth
      scof(0) = 1.d0
      do 50 j=1,5
        scof(j) = 0.d0
        do 48 k=1,5
          scof(j) = scof(j) + pinv(j,k)*q(k)
   48   continue
        scof(0) = scof(0) - scof(j)
   50 continue

      return
      end

c ***********************************************
      real*8 function pleg(n,y)
      real*8 y
      integer n
      pleg = 1.d0
      if (n.lt.1.or.n.gt.11) return
      goto (1,2,3,4,5,6,7,8,9,10,11) n

    1   pleg = y
        goto 20

    2   pleg = (3.d0*y**2-1.d0)/2.d0
        goto 20

    3   pleg = (5.d0*y**3-3.d0*y)/2.d0
        goto 20

    4   pleg = (35.d0*y**4-30.d0*y**2+3.d0)/8.d0
        goto 20

    5   pleg = (63.d0*y**5-70.d0*y**3+15.d0*y)/8.d0
        goto 20

    6   pleg = (231.d0*y**6-315.d0*y**4+105.d0*y**2-5.d0)/16.d0
        goto 20

    7   pleg = (429.d0*y**7-693.d0*y**5+315.d0*y**3-35.d0*y)/16.d0
        goto 20

    8   pleg = (6435.d0*y**8-12012.d0*y**6+6930*y**4-1260.d0*y**2
     1           +35.d0)/128.d0
        goto 20

    9   pleg = (12155.d0*y**9-25740.d0*y**7+18018.d0*y**5-4620.d0*y**3
     1           +315.d0*y)/128.d0
        goto 20
```

```
   10   pleg = (46189.d0*y**10-109395.d0*y**8+90090.d0*y**6
     1          -30030.d0*y**4+3465.d0*y**2-63.d0)/256.d0
        goto 20

   11   pleg = (88179.d0*y**11-230945.d0*y**9+218790.d0*y**7
     1         -90090.d0*y**5+15015.d0*y**3-693.d0*y)/256.d0

   20   return
        end
c ***********************************************************************
      real*8 function ppleg(n,y)
      real*8 y
      integer n
      ppleg = 0.d0
      if (n.lt.1.or.n.gt.4) return
      goto (1,2,3,4) n

    1   ppleg = 1.d0
              goto 20

    2   ppleg = 3.d0*y
        goto 20

    3   ppleg = (15.d0*y**2-3.d0)/2.d0
        goto 20

    4   ppleg = (35.d0*y**3-15.d0*y)/2.d0

   20   return
        end
c ***********************************************************************
c subroutine match calculates the elements of the matrix xj by numerical
c integration
      subroutine match(ipar,ep,de,fcof,bcof,scof,xj,r)
      implicit real*8(a-h,o-z)
      parameter(eps=1.d-5,jmax=20,jmaxp=21,kk=5,kkm=4)
      dimension s(jmaxp),xh(jmaxp)
      dimension fcof(0:5),bcof(0:5),scof(0:5),xj(4,4)

      do 20 j=1,4
        do 18 k=1,4
c Calculate the (j,k)th element of the matrix xj, using Romberg
c integration (p 114 in "Numerical Recipes").  Only needs to be
c done if j,k both even or both odd, and integration can be
c carried out over the half-interval (0 to 1)

          if (mod(j,2).ne.mod(k,2)) then
            xj(j,k) = 0.d0
            goto 18
          endif
          xh(1)=1.d0
          do 10 jj=1,jmax
            call trapzd(j,k,s(jj),jj,it,fcof,bcof,scof,ipar,de,ep)
            if (jj.ge.kk) then
              call polint(xh(jj-kkm),s(jj-kkm),kk,0.d0,ss,dss)
              if (dabs(dss).lt.(eps*dabs(ss))) goto 11
              if (dabs(dss).lt.(1.d-12).and.
     1            dabs(ss).lt.(1.d-12)) goto 11
            endif
            s(jj+1) = s(jj)
            xh(jj+1) = 0.25d0*xh(jj)
   10     continue
   11     continue
          xj(j,k) = -2.d0*ss*(r**(k-1))
          if (j.eq.k) then
            xj(j,k) = xj(j,k) - (r**(k-1))*2*(k+1)/(2*k+1)
```

```
          else if (dabs(xj(j,k)).lt.1.d-10) then
            xj(j,k) = 0.d0
          endif
   18   continue
   20 continue

      return
      end
c ***********************************************************************
c subroutine trapzd uses extended trapezoidal rule to evaluate integral
c using integrand at n evenly-spaced points.
      subroutine trapzd(j,k,s,n,it,fcof,bcof,scof,ipar,de,ep)
      implicit real*8(a-h,o-z)
      dimension fcof(0:5),bcof(0:5),scof(0:5)

      if (n.eq.1) then
        call eval(0.d0,s1,j,k,fcof,bcof,scof,ipar,de,ep)
        call eval(1.d0,s2,j,k,fcof,bcof,scof,ipar,de,ep)
        s = 0.5d0*(s1+s2)
        it = 1
      else
        tmn = dfloat(it)
        del = 1.d0/tmn
        x = 0.5d0*del
        sum = 0.d0
        do 91 jj = 1,it
          call eval(x,y,j,k,fcof,bcof,scof,ipar,de,ep)
          sum = sum+ y
          x = x + del
   91   continue
        s = 0.5d0*(s+sum/tmn)
        it = 2*it
      endif
      return
      end

c ***********************************************************************
c subroutine polint performs a polynomial interpolation on the
c results of successive trapezoidal-rule calculations of the
c integral, to find the limiting (zero-step-size) result.
      subroutine polint(xa,ya,n,x,y,dy)
      implicit real*8(a-h,o-z)
      parameter (nmax=10)
      dimension xa(n),ya(n),c(nmax),d(nmax)

      ns = 1
      dif = dabs(x-xa(1))
      do 11 i=1,n
        dift = dabs(x-xa(i))
        if (dift.lt.dif) then
          ns = i
          dif = dift
        endif
        c(i) = ya(i)
        d(i) = ya(i)
   11 continue

      y = ya(ns)
      ns = ns - 1
      do 13 m=1,n-1
        do 12 i=1,n-m
          xho = xa(i) - x
          xhp = xa(i+m) - x
          w = c(i+1) - d(i)
          den = xho - xhp
          if (den.eq.0.d0) pause'den=0 in polint'
```

```
          den = w/den
          d(i) = xhp*den
          c(i) = xho*den
   12   continue
        if (2*ns.lt.n-m) then
          dy = c(ns+1)
        else
          dy = d(ns)
          ns = ns - 1
        endif
        y = y + dy
   13 continue

      return
      end
c ***********************************************************************
c Subroutine eval evaluates the integrand at point x
      subroutine eval(x,y,j,k,fcof,bcof,scof,ipar,de,ep)
      implicit real*8(a-h,o-z)
      dimension fcof(0:5),bcof(0:5),scof(0:5)

      f = 0.d0
      fb = 0.d0
      s = 0.d0
      do 10 i=0,5
        f = f + fcof(i)*pleg(2*i+ipar,x)
        fb= fb + bcof(i)*pleg(2*i,x)
        s = s + scof(i)*pleg(2*i,x)
   10 continue
      y = ( (ep + de*s*f**2)*k*pleg(k,x) +
     1 de*s*f*fb*dsqrt((dabs(1.d0-f**2))*(1.d0-x**2))
     1 *ppleg(k,x))*pleg(j,x)

       return
       end

c ***********************************************************************
c Subroutine matinv performs matrix inversion by lower/upper
c decomposition and back substitution
      subroutine matinv(a,y,n,np)
      implicit real*8(a-h,o-z)
      dimension a(np,np),y(np,np),indx(5)

      do 2 i=1,n
        do 1 j=1,n
          y(i,j) = 0.d0
    1   continue
        y(i,i) = 1.d0
    2 continue

      call ludcmp(a,n,np,indx,d)
      do 3 j=1,n
        call lubksb(a,n,np,indx,y(1,j))
    3 continue

            return
            end

c ***********************************************************************
      subroutine ludcmp(a,n,np,indx,d)
      implicit real*8(a-h,o-z)
      parameter (nmax=100, tiny=1.0d-20)
      dimension a(np,np),indx(n),vv(nmax)

      d=1.d0
      do 12 i=1,n
```

```
      aamax=0.d0
      do 11 j=1,n
        if (dabs(a(i,j)).gt.aamax) aamax=dabs(a(i,j))
11    continue
      if (aamax .eq. 0.d0) then
        pause 'singular matrix'
      endif
      vv(i)=1.d0/aamax
12  continue

    do 19 j=1,n
      do 14 i=1,j-1
        sum=a(i,j)
        do 13 k=1,i-1
          sum=sum-a(i,k)*a(k,j)
13      continue
        a(i,j)=sum
14    continue
      aamax=0.d0
      do 16 i=j,n
        sum=a(i,j)
        do 15 k=1,j-1
          sum=sum-a(i,k)*a(k,j)
15      continue
        a(i,j)=sum
        dum=vv(i)*dabs(sum)
        if (dum .ge. aamax) then
          imax=i
          aamax=dum
        endif
16    continue
      if (j .ne. imax) then
        do 17 k=1,n
          dum=a(imax,k)
          a(imax,k)=a(j,k)
          a(j,k)=dum
17      continue
        d=-d
        vv(imax)=vv(j)
      endif
      indx(j)=imax
      if (a(j,j) .eq. 0.d0) a(j,j) = tiny
      if (j .ne. n) then
        dum=1.d0/a(j,j)
        do 18 i=j+1,n
          a(i,j)=a(i,j)*dum
18      continue
      endif
19  continue

    return
    end
c *******************************************************************
    subroutine lubksb(a,n,np,indx,b)
    implicit real*8(a-h,o-z)
    dimension a(np,np),indx(n),b(n)

    ii=0
    do 50 i=1,n
      ll=indx(i)
      sum=b(ll)
      b(ll)=b(i)
      if (ii .ne. 0) then
        do 60 j=ii,i-1
          sum=sum-a(i,j)*b(j)
60      continue
```

```
      else if (sum .ne. 0.d0)  then
        ii=i
      endif
      b(i)=sum
50  continue
    do 70 i=n,1,-1
      sum=b(i)
      do 80 j=i+1,n
        sum=sum-a(i,j)*b(j)
80    continue
      b(i)=sum/a(i,i)
70  continue
    return
    end
```